The Pennsylvania State University

The Graduate School

Department of Physics

PROGRESS TOWARDS AN ELECTRON ELECTRIC DIPOLE MOMENT MEASUREMENT WITH LASER-COOLED ATOMS

A Dissertation in

Physics

by

Neal Solmeyer

Submitted in Partial Fulfillment
of the Requirements
for the Degree of

Doctor of Philosophy

May 2013

The dissertation of Neal Solmeyer was reviewed and approved* by the following:

David S. Weiss
Professor of Physics
Dissertation Advisor
Chair of Committee

Kenneth M. O'Hara
Associate Professor of Physics

Murat Gunaydin
Professor of Physics

Sergei Tabachnikov
Professor of Mathematics

Nitin Samarath
Professor of Physics
Head of the Department of Physics

*Signatures are on file in the Graduate School

ABSTRACT

This dissertation recounts the progress made towards a measurement of the electron electric dipole moment. The existence of a permanent electric dipole moment of any fundamental particle would imply that both time reversal and parity invariance are violated. If an electric dipole moment were measured within current experimental limits it would be the first direct evidence for physics beyond the standard model. For our measurement we use laser-cooled alkali atoms trapped in a pair of 1D optical lattices. The lattices run through three electric field plates so that the two groups of atoms see opposing electric fields. The measurement chamber is surrounded by a four layer mu-metal magnetic shield. Under electric field quantization, the atoms are prepared in a superposition of magnetic sublevels that is sensitive to the electron electric dipole moment in Ramsey-like spectroscopy. The experiment requires very large electric fields and very small magnetic fields. Engineering a system compatible with both of these goals simultaneously is not trivial. Searches for electric dipole moments using neutral atoms in optical lattices have much longer possible interaction times and potentially give more precise information about the inherent symmetry breaking than other methods. This comes at the cost of a higher sensitivity to magnetic fields and possible sources of error associated with the trapping light. If noise and systematic errors can be controlled to our design specifications our experiment will significantly improve the current experimental limit of the electron electric dipole moment.

TABLE OF CONTENTS

LIST OF FIGURES

LIST OF TABLES

ACKNOWLEDGEMENTS

I would like to thank Professor David S. Weiss for his guidance throughout my graduate career. His unflinching adherence to the highest level of scientific rigor is truly an inspiration. I would also like to thank my 'partner in crime' Kunyan Zhu with whom I've worked side by side for the last six years. Without his ability to break down complex problems and attack them, the experiment would not be where it is today.

I would like to thank those I have worked directly with on our eEDM experiment: Fang Fang, who passed the torch of the experiment to me; Cheng Tang, to whom I am now passing the torch; and Matthew Ebert, who, as an undergraduate, helped us complete several projects during his brief time in lab. The physics department machinists Barry Dutrow, Tim Bowmaster, Tim Treaster, and Ryan Jacbo have done great work for us over the years. This work is supported by the NSF grant PHY-0969303.

I would also like to acknowledge the many colleagues who have assisted me in lab, lent me equipment, and given me numerous good conversations: Laura Adams, Ted Corcovilos, Karl Nelson, Xiao Li, Aaron Reinhard, Jean-Felix Riou, and Yang Wang. I am grateful and honored to be a part of the strong AMO community at Penn State consisting of the groups of Professor Kurt Gibble, Professor Nate Gemelke, and Professor Ken O'Hara. I would also like to thank my committee members; Professors Ken O'Hara, Murat Gunaydin, Sergei Tabachnikov, and of course David S. Weiss, for their generous contributions.

I thank Gary and Sandra Meyer for being good parents. Finally, I thank my wife, Anna Solmeyer for her help editing this dissertation and her support in all things non-physics.

Chapter 1. Introduction

Atomic systems have been a fruitful tool for probing numerous areas of physics. With the development of laser cooling and trapping, experimentalists have nearly complete control over all degrees of freedom of the atom (Chu, 1998). Laser-cooled atoms can be used in precision measurements (see Section 1.2), many-body physics (Bloch, Dalibard, and Zwerger, 2008), and quantum computers (Nielsen and Chuang, 2000) among other things. If high energy physics has uncovered a zoo of fundamental particles, then atomic physics offers nothing short of a jungle of possibilities.

Our measurement of an electron electric dipole moment (eEDM) requires precise application of techniques that have been developed in atomic physics over the last several decades as well as state of the art engineering. Searches for eEDMs are tests of the fundamental symmetries of nature. Understanding fundamental symmetries has been crucial to the development of modern physics. With our measurement we hope to aid in that development.

1.1. Symmetry

Symmetry has proven to be a powerful principle in physics. Through Noether's theorem, (Noether, 1918) symmetry under translation in space, rotation, and translation in time give rise to the conservation laws of momentum, angular momentum, and energy, respectively. Gauge symmetries lead to the conservations of charge, lepton number, quark color, etc. that form the basis of the standard model. Even many proposed extensions to the standard model often rely on the application of deeper

symmetries, such as supersymmetry (SUSY) which is based on a symmetry between bosons and fermions. Symmetry is critical to our current understanding of the physical laws.

Unlike continuous symmetries, discrete symmetries involve a reflection or interchange. In quantum mechanics, the study of three discreet symmetries in particular has proven to be elucidating; charge conjugation (*C*), parity (*P*) , and time reversal (*T*). *C* is the exchange of all particles with their anti-particles, or equivalently, switching the sign of all particles (i.e., *C* (H(*q*)) → H(-*q*)). *P* is the inversion of all spatial coordinates (i.e., P(H(*r*)) → H(-*r*)). *T* reverses the direction of time (i.e.,*T*(H(*t*)) → H(-*t*)). Most processes seem to be invariant under *C* and *P* symmetry, meaning that they look the same as their anti-particle counterpart and their spatial inversion. *T* reversal symmetry may not appear to hold on the macroscopic level of complex objects because a video of a glass falling off a table and shattering is rather bizarre if played backwards in time. However, this is due to the tendency of complex systems to increase their entropy and does not prove that *T* reversal symmetry is broken for fundamental processes. If the velocities of every single particle could be perfectly reversed, the broken glass would reconstitute itself and jump back onto the table. This would, of course, be practically impossible to arrange, but it would not violate the laws of physics. In their microscopic descriptions, most known fundamental processes are invariant under *T* reversal.

The *CPT* theorem shows that the simultaneous application of these three discrete symmetries is exact in any Lorentz-invariant quantum field theory that has a Hermitian Hamiltonian (Lee, Oehme, and Yang, 1957). Most quantum field theories preserve these properties and hence *CPT* symmetry is usually considered to be exact. The *CPT* theorem is also intimately connected to the spin-statistics theorem (see for example Guido and Longo, 1995). The question of *CPT* symmetry can of course be

asked experimentally, and such tests of *CPT* and Lorentz violation are ongoing (Brown *et al.*, 2010) but violations have not been observed. If *CPT* symmetry is exact, *T* violation is equivalent to *CP* violation.

1.1.1. Broken Symmetry

Until the mid-20th century, it was believed that *C*, *P*, and *T* were all individually good symmetries. In the mid 1950s Lee and Yang (1956) suggested that this may not be true and subsequent experiments proved them correct. *P* violation was first observed in beta decay of cobolt-60 (Wu *et al.*, 1957). Shortly after that, both *P* and *C* were found to be violated in the decay of pions (Garwin, Lederman, and Weinrich, 1957). To see why this is so, in the process of pion decay into a muon and a neutrino, $\pi^- \rightarrow \mu^- + \bar{\upsilon}^0$, the muon always has negative helicity. *P* reversal is broken because the *P* reversed process, i.e., with the positive muon helicity, does not occur. In the charge conjugated version of the decay above, $\pi^+ \rightarrow \mu^+ + \upsilon^0$, the helicity of the muon is not affected by the charge conjugation. So if *C* symmetry were to hold, we would expect the muon to still have negative helicity. But when this process is observed, the helicity of the muon is positive, and therefore *C* is also broken (Lederman and Hill, 2004).

Interestingly, the weak force violates *P* and *C* symmetry maximally by acting only on left-handed particles, or right-handed anti-particles (Feynman and Gell-Mann, 1958; Sudarshan and Marshak, 1958). To this day, *C* and *P* violation continue to be fruitful areas of research, (e.g., Abelev *et al.*, 2010). After the first violations of *P* and *C* were seen, it was proposed that the combined *CP* symmetry may be the true symmetry of nature (Landau, 1957). This is not the case.

1.1.2. *CP* violation

In 1965, Cronin and Fitch observed *CP* violation in the decay of neutral kaons (Fitch *et al.*, 1965). They won the Nobel Prize for this work in 1980. *CP* violation is described within the standard model by the Cabibbo-Kobayashi-Maskawa (CKM) matrix (Kobayashi and Maskawa, 1973), for which the Nobel prize was awarded in 2008. *CP* violation has also been seen more recently in *B*-meson decay (Abe *et al.*, 2001; Aubert *et al.*, 2002). The LHCb collaboration recently found evidence for *CP* violation in *D*-meson decay that differs from the standard model prediction by 3.5 sigma (Aaij *et al.*, 2012), though more data and more theoretical understanding is required to establish whether this is inconsistent with the standard model.

There are unresolved theoretical issues associated with *CP* violation. First is the so-called “strong *CP* problem”. All observed *CP* violation happens in the weak sector. There is a possible *CP* violation in quantum chromodynamics (QCD), known as θ_{QCD}, that would give rise to effects like a neutron EDM. However, when it has been experimentally measured, θ_{QCD} is unnaturally small, i.e., less than 10^{-10} (Pospelovitz and Ritz, 2005). With no a-priori reason to expect this angle to be this small, this leaves open the possibility that something is missing from the description of *CP* violation within QCD.

A second theoretical problem relates to an issue in cosmology. The abundance of matter over anti-matter in the observable universe has long puzzled cosmologists (Ellis, 2003). Sakharov (1966) proposed that this asymmetry can arise due to *CP* violation. However, the observed *CP* violation described by CKM theory is not large enough to explain the observed matter anti-matter asymmetry of the universe. There is therefore some reason to believe that additional sources of *CP* violation might exist.

1.1.3. Electric dipole moments

The existence of a permanent EDM of any fundamental particle violates *T* symmetry. This is so because a permanent EDM would necessarily be either aligned or anti-aligned with the angular momentum (***J***) or equivalently the magnetic moment of a fundamental particle. This is a consequence of the Wigner-Ekhart theorem (see for example Budker, Kimball and DeMille, 2004). Intuitively, if the EDM did *not* align with ***J***, then a new quantum number would be needed to describe the projection of the EDM axis along ***J***. This additional degree of freedom would be statistically observable in counting the energy levels in an atom. Because it is not observed, we conclude that if the electron has an EDM, its axis must coincide with that of ***J***.

The Hamiltonian for a particle with an EDM (*d*) placed in an electric field (***E***) is:

$$H = -\boldsymbol{d} \cdot \boldsymbol{E} = -d\frac{\boldsymbol{J}}{J} \cdot \boldsymbol{E} \qquad (1.1)$$

The electric field vector, ***E*****,** is a displacement vector and is therefore even under *T* reversal and odd under *P* reversal. ***J*** on the other hand is an axial vector and is odd under *T* and even under *P*. Performing either a *T* or *P* transformation will result in the Hamiltonian:

$$T(H) = P(H) = -H \qquad (1.2)$$

Thus, an EDM breaks both *T* and *P* symmetry.

As discussed above, if the *CPT* theorem holds, *T* violation implies *CP* violation. The CKM theory does predict a value for the electron EDM, but the effect only enters at the third loop level of QED and is very small (Bernreuther and Suzuki, 1991). The standard model's prediction for the eEDM is more than 10^{10} times smaller than the current experimental sensitivity (Hoogeveen, 1990) and is for all practical purposes unobservable.

Despite many attempts, as of November 2012 no experiment has ever observed a value for a permanent EDM of a fundamental particle. Only upper limits have been set. The goal of current experimental programs is to make these measurements more accurate, pushing the upper limits of the value of an EDM smaller and smaller.

1.1.4. Beyond the standard model

The standard model is the currently accepted physical description of the electroweak and strong forces, i.e., all fundamental processes not including gravity. It was finalized and realized its modern form in the 1960s and 1970s. For their work in formulating the standard model, Sheldon Glashow, Abdus Salam, and Steven Weinberg shared the Nobel prize in 1979. Though there are reasons to believe that the standard model is not complete, there has never been a direct observation that violates its predictions.

Many models of physics beyond the standard model, notably SUSY, generically predict much larger values for the eEDM. They tend to do this because they have additional particles that can add *T*-violating terms which contribute to the EDM at the one or two loop level (Bernreuther and Suzuki, 1991). Minimal SUSY models predict eEDMs within range of the current experimental limits. The next two orders of magnitude of precision contain the predictions of several other SUSY variants. As a result, minimal SUSY theorists are challenged to explain why an EDM has not yet been measured. If the experimental upper bound is improved and no EDM is observed, additional constraints will be placed on these theories. Alternatively, if a non-zero EDM is measured, it would be the first direct evidence of a violation of the standard model. As long as an EDM measurement helps to push the upper limit further down, there is

theoretical knowledge to be gained regardless of whether the result of the measurement is positive or null. This and the technical challenges associated with pushing experimental limits are what make EDM searches such an exciting prospect for many experimentalists.

1.2. EDM searches

Experimentalists began looking for eEDMs and EDMS of other fundamental particles as early as 1950 (Purcell and Ramsey, 1950). For relatively recent overviews see Fortson, Sandars, and Barr (2003) and Commins (2007). The sensitivity of eEDM measurements improved rapidly during the first few decades of searches. An exponential fit to the 5 experimental lower limits since 1984 shows an improvement of an order of magnitude every 21 years (see Figure 1-1). A variety of systems have been used; neutral atoms, molecules, molecular ions, and solid state systems. We will briefly describe these for comparison in the last half of this chapter. For the reasons described in the next section as well as other reasons, eEDM measurements are rarely done on bare electrons.

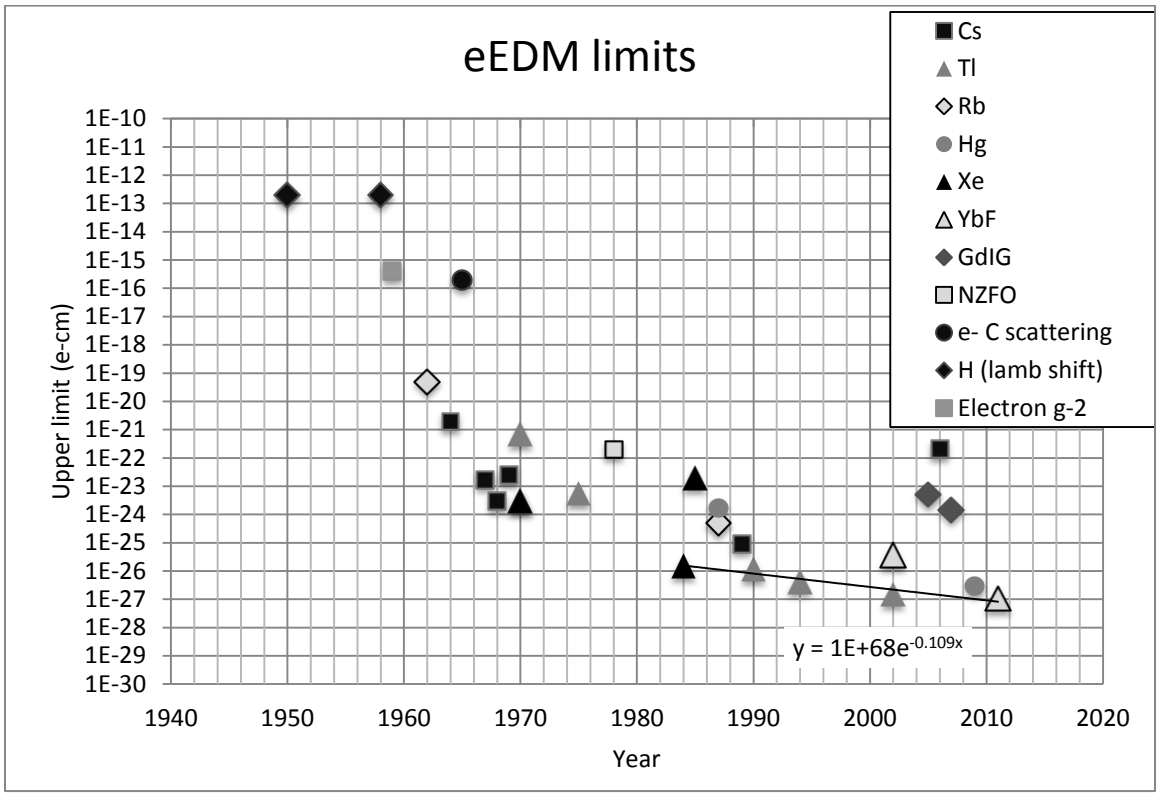

Figure 1-1. *Historical eEDM limits*

After initial rapid progress, the lower limit of the eEDM has been improving by an order of magnitude every 21 year since 1984.

1.2.1. Enhancement factors

It is worth noting that most of the things we think of as electric dipole moments are not permanent in the strictest sense of the term. The dipole moment of a water molecule, for instance, is induced by an externally applied electric field. In a truly zero electric field, the two opposite polarities of a water molecule are degenerate and the lowest energy state is an equal superposition of them. As the electric field strength grows, the degeneracy is lifted and the energy separation of the two states diverges. Many molecules will become completely polarized even for relatively small electric fields,

and for larger electric fields the induced dipole moment will appear to be permanent as it approaches the familiar energy relationship:

$$E = \boldsymbol{d} \cdot \boldsymbol{E} \tag{1.3}$$

But a true permanent EDM of a fundamental particle is one that remains even when the applied electric field is zero.

There are several ways a neutral atom can have a permanent EDM. If the electron has an EDM, a neutral atom will have one in much the same way that a neutral atom has a spin from the internal spin of the electron. The ratio of the atomic EDM, d_a, to the electron EDM, d_e, is the enhancement factor R. It is also possible for the atom to have an EDM induced by other T-violating effects. The possibilities are permanent nucleon (proton or neutron) EDMs, electron-nucleon interactions, or nucleon-nucleon interactions (Pospelov and Ritz, 2005). In general, each of these contributes to the EDM of the atom. However, in heavy paramagnetic atoms with one valence electron, such as Cs, Rb, and thallium (Tl), the electron EDM is generally expected to be the leading term, although P and T violating electron-nucleon interactions could possibly explain a paramagnetic atom EDM. Complementary EDM measurements on systems such as neutrons, mercury, radium, or xenon, are sensitive to other T-violating effects.

In classical mechanics, Schiff's theorem implies that the enhancement factor for any neutral atom would be exactly zero because all charges would rearrange to cancel out any external field (Schiff, 1963). However, it has long been known that when the atom is treated relativistically, Schiff's theorem can be violated and can lead to an enhancement of the electron EDM (Sandars, 1965). The enhancement factor can be estimated as $\sim 10\alpha^2 Z^3$ where α is the fine structure constant and Z is the atomic number. An intuitive explanation for the evasion of Schiff's theorem relies on the fact that the electron moves relativistically in the atom. The length contraction of the electron leads to

the difference of the EDM in the electron's frame of reference compared to that of the atom i.e., the lab (Commins, *et al.*, 2007).

For the heavy paramagnetic atoms, the enhancement factor can be calculated readily using atomic wavefunctions. The *T*-violating term from the eEDM is considered as a perturbation on the overall Hamiltonian of the atom. This term tends to mix states with opposite parity, allowing an EDM to exist. The expectation value of the dipole moment of the atom can be extracted from the perturbed wave functions. The enhancement factors for Cs and Rb were recently calculated to be 120.5 and 25.7, respectively, with less than 1% uncertainty (Nataraj *et al.*, 2008).

One way to boost a potential signal size in an EDM measurement is to choose a system with the largest enhancement factor. This has been one of the driving forces behind molecular searches. Molecules can become completely polarized in modest electric fields, and there is no further gain from increasing the electric field. The enhancement factor of a molecule is often interpreted as an effective electric field at the electron which comes from the altered charge distribution of the polarized molecule.

Table 1-1 summarizes the enhancement factors, *R*, and effective electric fields, E_{eff}, for several of the ongoing eEDM experiments for typical applied electric fields, E_{app}, during the experiment. For comparison purposes E_{eff} for neutral atoms is reported as the enhancement factor multiplied by the applied electric field even though the physical interpretation of the enhancement factor of neutral atoms is not an effective electric field and we also report the enhancement factor of molecules as E_{eff}/E_{app} even though the molecules saturate so that increasing E_{app} may not increase the E_{eff}. The references for these numbers are given in the text about each experiment in the following subsections. Furthermore, as a figure of merit, E_{eff} multiplied by a typical measurement time, τ, is reported which, as will be seen later, is directly proportional to the signal size. Though it

misses some important factors, such as the number of particles measured, Table 1-1 shows that the current experiments can have quite competitive ultimate sensitivities even though many of their parameters are dramatically different. The overall sensitivity of our experiment is discussed more in Section 8.2.

System	Cs	Rb	Tl	YbF	ThO	HfF+
E_{app} (V/m)	$1.5*10^{7}$	$1.5*10^{7}$	$1.23*10^{7}$	$1*10^{6}$	$1*10^{4}$	$\sim 1*10^{2}$
R	120.5	25.7	-585	$-1.45*10^{6}$	$1*10^{9}$	$1*10^{10}$
E_{eff} (V/m)	$1.8*10^{9}$	$3.8*10^{8}$	$7.2*10^{9}$	$-1.45*10^{12}$	$1*10^{13}$	$1*10^{12}$
τ (s)	3	3	$3*10^{-3}$	$6.4*10^{-4}$	$1.5*10^{-3}$	0.1
$E_{eff}*\tau$	$5.4*10^{9}$	$1.1*10^{9}$	$2.2*10^{7}$	$-9.3*10^{8}$	$1.5*10^{10}$	$1*10^{11}$

Table 1-1. *Enhancement factors and effective electric fields of some eEDM experiments*

1.2.2. Molecules

The current experimental limit on the eEDM is $1.05*10^{-27}$ e-cm and it is provided by the molecular eEDM experiment of Ed Hind's group at the Imperial College London (Hudson *et al.*, 2011). This experiment utilizes the ytterbium fluoride (YbF) molecule. Molecular experiments typically prepare the molecules in super-positions of m_F levels and look for relative shifts of those levels in an electric field similar to the way our measurement works, as described in Section 2.2. This measurement is limited by statistics. The largest systematic error comes from an uncertainty in the shape of the electric field which affects the radio frequency transfers during the measurement.

The large enhancement factors of molecular systems are very promising for future eEDM experiments (Meyer and Bohn, 2009). A collaboration, called ACME (Atomic Cold Molecule Experiment) between David DeMille (Yale), Gerry Gabrielse (Harvard), and John Doyle (Harvard) and uses thorium monoxide (ThO) molecules, is a promising example (Vutha *et al.,* 2007, 2011). It hopes to improve the experimental limit

by utilizing internal states of the molecule which have opposite sign E_{eff} in a clever measurement scheme and by starting with a cold buffer gas cooled beam of molecules.

In addition, there are several other molecular searches going on such as the lead fluoride (PbF) experiment at the University of Oklahoma under Neil Shafer-Ray, the tungsten carbide (WC) experiment at the University of Michigan under Aaron Leanhardt, the lead oxide (PbO) experiment at Yale under David DeMille, and the incipient PbO experiment at the University of Massachusetts under David Kawall.

1.2.3. Molecular ion

The hafnium fluoride molecular ion (HfF+) has also been identified as a promising candidate for an eEDM measurement (Petrov, Mosyagin, and Titov, 2009). Eric Cornell's experiment at JILA takes place in an ion trap using a rotating electric field as the measurement field (Leanhardt, 2011). The HfF+ molecular ion polarizes at a low applied electric field which simplifies many experimental details. It is notable that the science signal from this measurement comes from a single molecular ion and they expect to have coherence times in the trap as long as 0.5 seconds.

1.2.4. Solid state

There are several attempts to measure the eEDM within a solid state system. These measurements attempt to take advantage of the large signal size coming from a macroscopic sample of atoms. The goal is look for an electric field induced magnetization (Lamoreaux, 2002). There is an ongoing experiment at the Indiana University under Chen-Yu Liu using the paramagnetic insulator gadolinium gallium

garnet (GGG; Kim *et al.*, 2011). Another interesting proposal by Steve Lamoreaux's group at Yale is to use a ferro-electric material that can sustain a sizable E_{eff} even when the externally applied field is brought to zero (Rushchanskii *et al.,* 2010). Solid state eEDM measurements have tremendous statistical sensitivity, but have historically been plagued by the uncontrolled systematic effects associated with a solid state system.

1.2.5. Neutron and nuclear EDMs

There are many ongoing experiments to measure other permanent EDMs. These include neutron EDM experiments (Baker *et al.*, 2006) and atomic EDM experiments such as Griffiths *et al.,* (2009). Even though Griffiths *et al.,* (2009) is pretty sensitive to the eEDM, it is more sensitive to the non-EDM *T* violating effects described above. There are also several groups attempting to measure the EDMs of radium, xenon, and francium. There are ongoing experiments and proposals to measure the EDMs of the muon, proton, and deuteron in storage rings. These experiments have many of the same concerns as searches for eEDMs, but they probe different fundamental physics.

1.2.6. Neutral atoms

Before the YbF results in 2011, the previous limit on the eEDM was held for several years by Eugene Commins's group at Berkeley (Regan *et al.*, 2002). Their experiment used a Tl fountain. Beams of Tl were launched up between three electric field plates. This experiment is similar to ours except that it is done with a beam of atoms, titanium electric field plates, and a magnetic field quantization axis. The limitation of this measurement was the uncertainty in the motional magnetic field from the $\boldsymbol{v}\times\boldsymbol{E}$

effect, as well as the Berry's phase from the motion of the atoms. Neutral atoms have the disadvantage of being more sensitive to magnetic fields than molecules.

In addition there is another group pursuing eEDM measurements with Cs: Dan Heinzen's group at the Univerisity of Texas.

1.2.7. Motivation for our measurement

Our measurement design relies on the maturity of techniques used to manipulate neutral atoms. Previous neutral atom measurements and molecular searches have been beam experiments, in which the measurement occurs while the atoms or molecules traverse a region with an electric field. In our experiment, the well-understood laser trapping and cooling techniques for Cs and Rb atoms allow them to be trapped between electric field plates. This allows for measurement times of a few seconds, while beam experiments are often limited to interaction times on the scale of milliseconds. Having the atoms motionless also reduces the $\boldsymbol{v}\times\boldsymbol{E}$ and geometric phase effects to negligibly small levels. This comes at the cost of systematic effects that are associated with the trapping laser light (Chin *et al.* 2001). Further, the enhancement factor does not saturate in atoms, while a molecule can become completely polarized, leading to competitive final sensitivities.

In addition, the precision of the calculation of the enhancement factor for alkali atoms, like Cs and Rb, gives a more accurate measurement of the EDM value of the electron and so can ultimately give a more accurate determination of the eEDM. Performing the measurement on both Cs and Rb will allow us to compare the expected size of the eEDM signal for the two species serving as a final test against systematic errors.

Our project has produced one Ph.D. dissertation already (Fang, 2007). Details from that work are referenced in the text. In addition, much of the work presented here was done in collaboration with a fellow student, Kunyan Zhu. His future dissertation will also be cited in the text as Zhu (*forthcoming*) when appropriate.

Chapter 2. Measurement Procedure

2.1. Overview of the dissertation and experiment

In very broad terms, our eEDM measurement requires precise spectroscopy of Cs atoms in a large electric field with minimal magnetic fields. There are many challenges associated with being able to accomplish these goals simultaneously on one apparatus. The remainder of this dissertation will describe how our experiment meets those challenges.

In the second half of Chapter 2 I give an overview of the measurement procedure. The eEDM measurement will look for a linear shift in energy between the m_F and $-m_F$ magnetic sublevels of Cs in an electric field. The atoms will be transferred from the($F = 0$, $m_F = 0$) state to a superposition of (3,3) and (3,-3) that is directly sensitive to the eEDM. This superposition will evolve during the free measurement time such that the number of atoms that are transferred back to the (0,0) state will depend on the eEDM and the measurement time. This provides a context for the rest of the dissertation which describes how we hope to obtain such a measurement.

The atoms must be prepared in a region that is suitable for the measurement. The atom preparation is described in Chapter 3. First, Cs atoms are heated in an oven to 420 °K. They are slowed in a 1 m Zeeman slower and are collected in a magneto-optical trap (MOT). The relatively large magnetic fields needed for the MOT would interfere with the low magnetic fields needed to suppress systematic errors, so we must transfer the atoms to a measurement chamber. The MOT magnetic fields are adjusted so that the atom cloud can be alternately overlapped with the light from two parallel build-up cavities separated by 1 cm which pass vertically through the vacuum chamber. The dipole force

from the light in the cavity creates a 1-dimensional optical lattice which guides the atoms transversely during the launch. We launch the atoms 84 cm vertically using the technique of moving molasses as described in Section 3.1. Details of the build-up cavities are described in Section 3.3.

When the atoms reach the top of their trajectory, a set of cooling beams is pulsed on so that the atoms are stopped, re-cooled, and trapped in the lattices. The atoms have a ~6.25 second vacuum limited lifetime in the trap. Using multiple loadings and launches over ~1 second we can load a few cm vertical spread of atoms into the lattices in the measurement chamber.

The measurement chamber consists of a 1 m long glass cell situated above the MOT chamber. Immediately around the glass cell, a plastic platform holds all of the optics necessary for cooling and imaging. The mounts for these optics must be completely non-magnetic and made out of predominantly non-conducting material. This platform is encased in a four-layer mu-metal magnetic shield. Chapter 4 describes the design, construction, and installation of the magnetic shield. It provides shielding factors of at least > $5*10^4$ transversely and ~$1.3*10^4$ axially (the shields have not been measured after improvements to the mounting design). A set of three magnetic field coils, with diameters ~ 3 m, are installed around the optics table in order to cancel the earth's magnetic field so that the magnetic shields do not saturate.

Directly inside the inner-most magnetic shield layer there is a 24" long and 16" diameter plexiglass cylinder, on which a set of eight magnetic field coils are built. The magnetic field coils provide the three bias fields and five independent first order derivative fields. These magnetic fields are used for several purposes. They provide the quantization axis for optical pumping and microwave transitions, they are used to zero magnetic fields and field gradients during the measurement procedure, and they provide

magnetic fields for state selective measurements. The design and construction of the magnetic coils are described in Chapter 5. The plexiglass cylinder also holds a platform for the measurement chamber optics.

Inside the measurement chamber, the two parallel optical lattices thread three glass electric field plates which are described in Chapter 6. The center plate is held at the high voltage while the outer plates are grounded. The plates are made of glass because glass is non-magnetic, minimizes Johnson noise, and allows optical access. They are specially coated with high reflective (HR) and anti-reflective (AR) surfaces. The plates also have an outer coating of the transparent conductor indium tin oxide (ITO). The electric field plates are designed to sustain up to 60 kV and are separated by 4mm. They are mounted with titanium, which is nonmagnetic, good for vacuum, and has relatively low conductivity to minimize Johnson noise. Fused silica spacers hold the plates at 4 mm separation, and do not sustain significant leakage currents that might lead to false EDM signals.

The arrangement of two parallel lattices between three electric field plates is essential in that it allows a simultaneous measurement of atoms with opposite electric fields (see Section 8.1). This improves the measurement noise by making it insensitive to uniform B field fluctuations. In addition, between shots, the polarity of the central electrode can be reversed. This makes the measurement insensitive to static B field gradients. The lattices are linearly polarized in the direction parallel to the electric field in order to minimize systematic effects associated with the trapping light.

With the atoms prepared in the measurement chamber, the state preparation for the eEDM measurement can be developed. First the atoms are optically pumped into the stretched state. A series of microwave pulses bring the atoms to the $m_F = 0$ state to

initiate the measurement procedure. The microwave state preparation is described in Chapter 7.

For the measurement to be successful it must meet stringent requirements on statistical noise and systematic error. In Chapter 8 we discuss how our experiment meets these requirements. The three most important systematic effects are; leakage currents across the plates, which create magnetic fields that change sign with the electric field; an interaction between a magnetic field gradient, electric field gradient, and imperfect electric field reversal; and a third order effect associated with the residual circular polarization of the trapping light.

In all, the lasers and optics used in the experiment fill up two connected 5' x 8' optical tables. The vacuum chamber has four ion pumps, and two titanium sublimation pumps (TSPs). EDM measurements are table top experiments that probe some of the same physics as large collider experiments. But they are big tables.

2.2. Ramsey-like fringe

Our measurement procedure can be thought of as a generalization of a Ramsey fringe (Ramsey, 1950). I will first briefly describe the Ramsey fringe and then will describe our measurement. In a traditional Ramsey fringe an atomic sample is subject to two π/2 pulses separated by a free evolution time, *T*. The first π/2 pulse creates a superposition between the ground and excited state:

$$|g\rangle \xrightarrow{\frac{\pi}{2}\,pulse} |g\rangle + e^{-i\varphi}|e\rangle \qquad (2.1)$$

When left to evolve freely in an electric field, the phase difference between the two components of the superposition, φ, will be given by $\varphi = T/\tau$, where *T* is the free

evolution time and τ is the precession time of the atom in the field. If φ is 0, or an integer multiple of 2π, then the second π/2 pulse, when combined with the first, will act as a π pulse and all of the atoms will be transferred to the excited state. If φ is an odd integer multiple of π, then all the atoms will return to the ground state. In general the number of atoms that return to the initial state will depend on the free evolution time and the precession time.

For our measurement, the excited state is a superposition of two degenerate energy levels. The details of the state preparation will be described in more detail in Chapter 7, but for now assume that we start with atoms in the (F = 0, m_F = 0) sub-state of the hyperfine ground state of a Cs atom in a large applied electric field. The degeneracy of the | m_F | levels is lifted by the tensor DC-stark shift. The tensor stark shift is very small so a large electric field is required. At 125 kV/cm the energy shift is 45 m_F^2 Hz (Carrico *et al.*, 1968; Simon, Laurent, and Clairon, 1997). From there we transfer the atoms to the superposition of (3, 3) + (3,-3). The transfer to this superposition will be done with a sequence of low frequency B-fields, which contain several frequency components on the order of 20 to a few hundred Hz, depending on the electric field used (Zhu, *forthcoming*).

In the absence of any magnetic field, and for the moment neglecting the EDM, the tensor shifted m_F = ±3 would be perfectly degenerate. If the atom has an EDM, the energy levels will be shifted by:

$$\mathcal{E}_{edm} = \boldsymbol{d}_a \cdot \boldsymbol{E} = m_F \, R_{Cs} \;\; d_e \, E \qquad (2.2)$$

Where the atomic EDM, d_a, is given by the dipole moment of the electron multiplied by the enhancement factor R_{Cs}. The quantum number, m_F, accounts for the orientation of the EDM with respect to the electric field. In other words, for a positive electric field, the m_F = +3 states will shift up and the m_F = -3 states will shift down.

Though, because we do not know the sign of d_a,the shifts could be in the opposite directions. See Figure 2-1 for the energy levels of Cs in a large applied DC electric field. This slight energy splitting means that during the free evolution time the two components of the superposition will accrue a relative phase difference that is proportional to the EDM and is given by it is given by $\varphi = Td_aE/h$, where h is Planck's constant. In analogy to the Ramsey sequence, a second pulse identical to the first returns atoms to the m_F = 0 state in a proportion that depends on φ. The final signal for the eEDM is the population of atoms returning to (3,0).

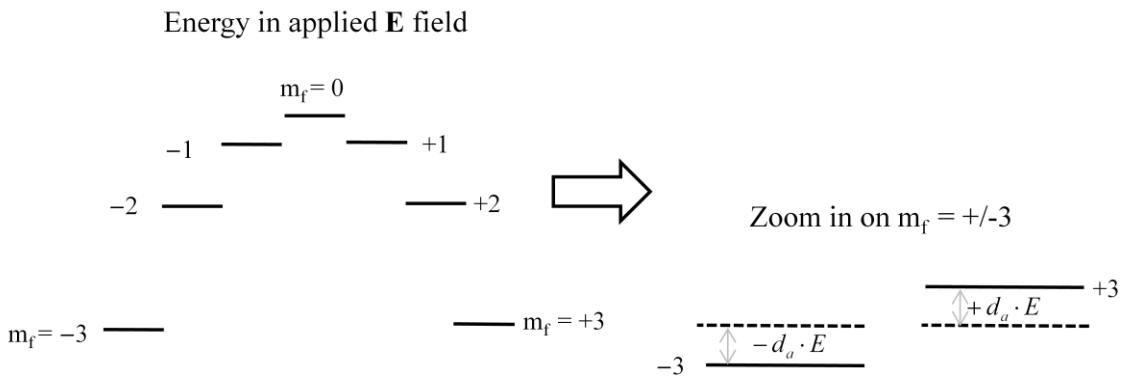

Figure 2-1. *Energy levels of Cs F=3 in a large E field*

2.2.1. Small magnetic bias field

The practicalities of performing the measurement in a real environment suggest that rather than using the exact sequence described above, it should rather be done in a small controllable magnetic bias field. This magnetic field provides an additional linear shift to the two components of the superposition state. We keep the free evolution time fixed and scan the small bias magnetic field to map out an entire fringe. An EDM signal would appear as an overall shift of the Ramsey fringe with its electric field parallel to the

applied magnetic field with respect to the Ramsey fringe with its electric field anti-parallel to the applied magnetic field. See Figure 2-2 for a depiction of such a sequence.

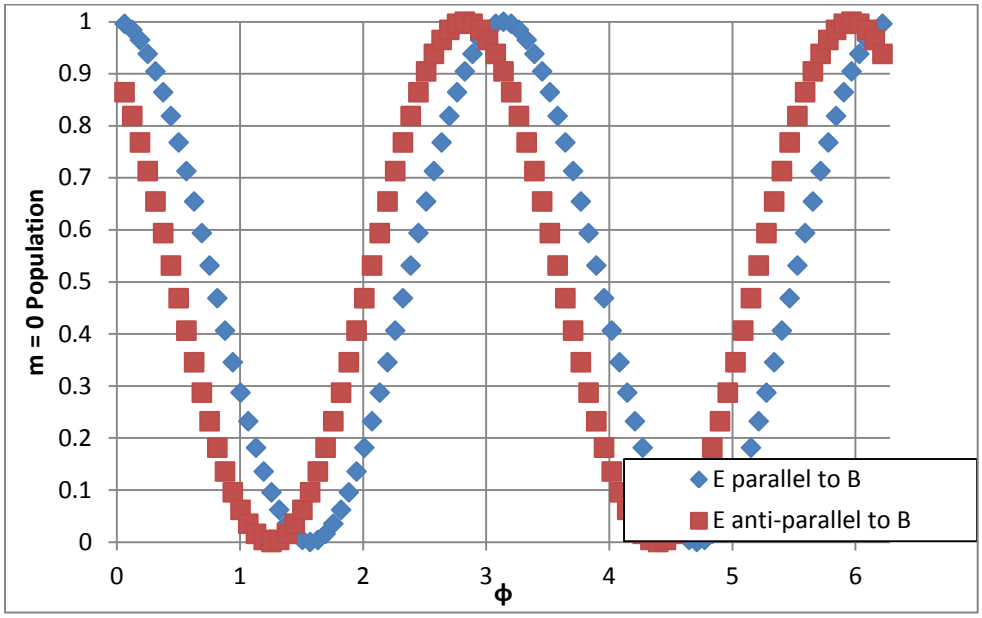

Figure 2-2. *Shifted Ramsey-like fringe*

Since the magnetic field will dominate the contribution to the phase, a fringe size can be calculated by setting the phase difference accumulation of the magnetic field over the measurement time to 2π:

$$\varphi = 2\pi = 2\,\boldsymbol{\mu}\cdot\boldsymbol{B} = g\,m_F\mu_B B\frac{T}{\hbar} \qquad (2.3)$$

Where T is the measurement time (~3 seconds), and μ_B is the Bohr magneton. This corresponds to a magnetic field of 160 nG. The bias field will be scanned through values on this order of magnitude.

In reality, the data analysis will be more complicated than this, and it will be partially described in Chapter 8. The purpose of this simplified illustration of the measurement procedure is to provide a basic understanding to motivate the design features of the experiment.

2.2.2. Sensitivity to magnetic fields

It is clear from this measurement procedure why our experiment is so sensitive to magnetic fields. Due to the Wigner-Ekhart theorem, the EDM is necessarily aligned with the magnetic moment. Whatever the enhancement factor, the magnetic moment of an electron is much larger than the EDM. For example, using cgs units, in which the electric and magnetic fields have the same units, the magnetic dipole moment is 16 orders of magnitude larger than the current experimental eEDM limit. In the worst case, if a small magnetic field changes sign when the sign of the electric field changes, it will exactly mimic the effect of the eEDM we are trying to measure. If a small magnetic field fluctuates randomly, it may wash out our ability to measure the small shifts from the eEDM. Minimizing and controlling possible sources of error from magnetic field noise are the most technically challenging aspects of our EDM search.

Chapter 3. Atom Preparation

3.1. MOT loading and launch

3.1.1. Vacuum system

Figure 3-1 shows a simplified version of our vacuum system and gives the lab coordinate system. The Cs and Rb reservoirs are connected to the oven vacuum chamber by all metal valves. See (Figure 3-1 (a)). The oven chamber (b) has a gate valve that separates it from the Zeeman slower and the main vacuum chamber. We cannot use magnetic sealing gate valves due to our sensitivity to the magnetic field, so we use gate valves that rely on a Viton sealing ring, which are subject to periodic failures. The gate valves allows the Cs or Rb to be replaced without breaking vacuum on the entire vacuum system.

A 1m tube (c) which connects the oven chamber to the main chamber (d) forms the Zeeman slower. A second gate valve separates the main chamber from the bottom 6-way cross (e). This gate valve allows us to work on the top portions of the system without breaking vacuum in the bottom.

Above the bottom 6-way cross is the 1-m long glass cell (f). The cell forms the measurement chamber. The central part of the cell is made of optical quality glass that allows beams to access the atoms. Above the glass cell is the top 6-way cross (g). Both the top and bottom 6-way crosses provide ports for electric feedthroughs which are described more thoroughly in Section 6.4.

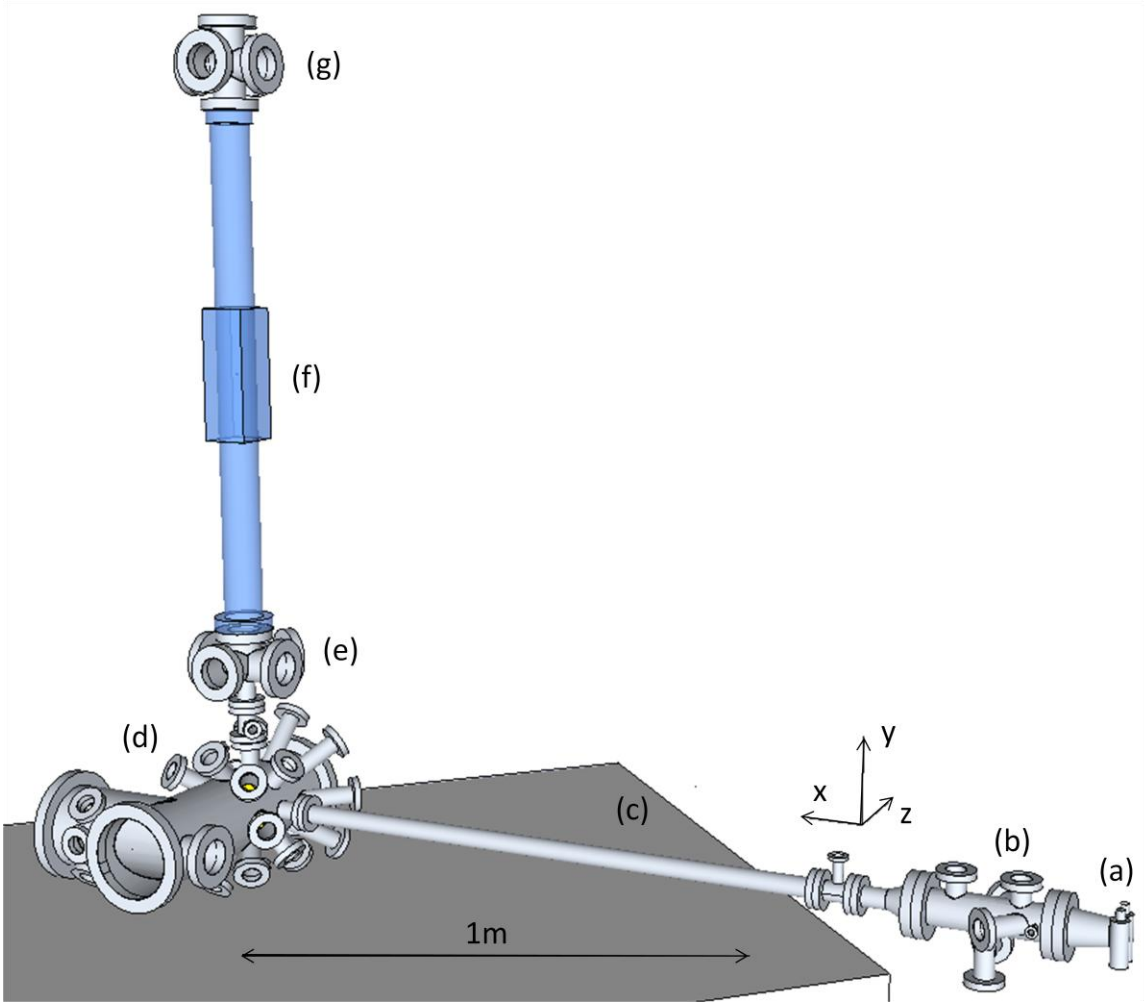

Figure 3-1. *Simplified picture of vacuum system*

a) atomic reservoirs, b) oven chamber, c) Zeeman slower, d) main chamber, e) bottom 6-way cross, f) glass cell measurement chamber, g) top 6-way cross.

The vacuum pumps are not shown on the diagram, but include ion pumps off of the oven chamber, main chamber, top 6-way cross, and bottom 6-way cross; and TSPs off of the top and bottom 6-way crosses. The main chamber, top 6-way cross, and oven chamber all have ion gauges for monitoring the vacuum pressure.

Whenever the vacuum chamber is opened for more than a few hours, we must bake the system in order to achieve a suitably low vacuum pressure. Baking primarily

gets rid of water vapor left in the system. In order to bake, we wrap the system with ~15 heat tapes powered with variable AC power supplies. Roughly 30 thermo-couples are used to monitor the pressure. The system is wrapped in aluminum foil and is slowly and evenly brought up to ~120 °C. The temperature is held constant for several days while the chamber is pumped out with two turbo-pumps. Right after a bake we can typically achieve vacuum pressures as low as ~3-5*10^{-11} Torr in the main chamber as measured with an ion gauge.

3.1.2. Laser system

The laser beams needed in order to slow, trap, and cool the atoms, as well as to perform the measurement procedure, are all tuned near the 852 nm $6^2P_{3/2}$ to $6^2S_{1/2}$ (D_2) lines of Cs. The relevant transitions and laser frequencies are shown in Figure 3-2. For the Cs system, these beams are provided by two diode lasers that are injection locked by a master laser at 852.3 nm. The master laser is PID locked to the $F = 4$ to $F' = 4$ and $F' = 5$ crossover line in saturation absorption spectroscopy. It has a line-width of 72 kHz. Each 'slave' diode laser provides ~200 mW of laser light.

Several acousto-optic modulators (AOMs) control the frequency and amplitudes of the beams. These two lasers provide all of the MOT beams, the cooling beams for the measurement chamber, as well as the optical pumping and state detection beams.

A separate diode laser is locked to the $F = 3$ to $F' = 4$ line to provide repumping for the slowing and cooling stages. The lasers and optics for the optical cavities are covered in Section 3.3.

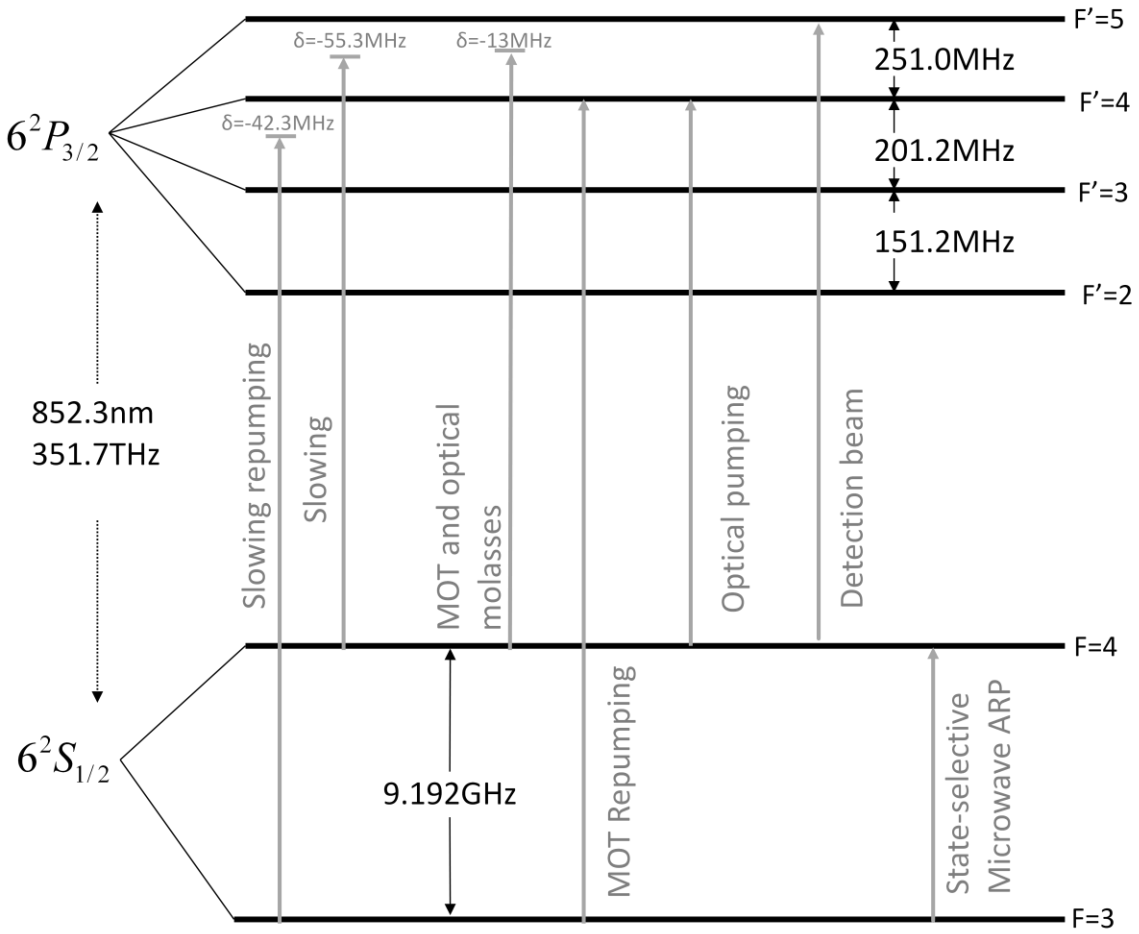

Figure 3-2. *Cs D_2 line and laser frequencies*

3.1.3. Atom collection

During operation, the atom reservoir is heated to 420 °K and the Cs atoms are boiled out of the reservoir through a nozzle. The nozzle is a glass capillary array with 10 μm diameter 1 mm long holes which partially collimate the atomic beam.

The details of the Zeeman slower (c in Figure 3-1) are covered in detail in Fang (2007, pp. 104-109). In short, the Zeeman slower consists of a circularly polarized laser

beam which is aligned counter-propagating to the atomic beam coming from the oven (Phillips and Metcalf, 1982). The beam is red-detuned so that it is close to resonance with the Zeeman and Doppler shifted $F = 4$ to $F' = 5$ transition of the moving atoms. As the atoms absorb the light, they lose forward momentum. A magnetic field changes magnitude along the length of the 1 m tube, keeping the atoms in resonance with the light as they slow down. At the end of the Zeeman slower, their velocity is low enough that they can be captured in a MOT. A repumping beam is also needed to retrieve the atoms which have fallen to the dark $F = 3$ state.

In the future, it could be possible to increase the number of atoms slowed from the Zeeman slower by adding transverse cooling beams near the oven. The optical viewports for such beams exist on the vacuum chamber and the beams could be obtained readily from our existing lasers.

In the main chamber, three counter-propagating laser beam pairs and a pair of anti-Helmholtz coils form the MOT. The anti-Helmholtz coils provide a magnetic field gradient of 7 G/cm. The geometry of the MOT beams in relation to the Zeeman slower and the atomic beam is shown in Figure 3-3. These beams also provide 3-dimensional optical molasses for the atoms. We load the MOT using a detuning of -13 MHz and 250 $\mu W/cm^2$. The MOT beams have a waist radius of 10 mm and the atomic cloud has a radius of 0.35 mm. The MOT beams are relatively large because we need to shift the MOT between two locations separated by 1cm, as will be described in the next section. The MOT can load $2*10^8$ atoms/s. In practice the loading times are a few hundred ms.

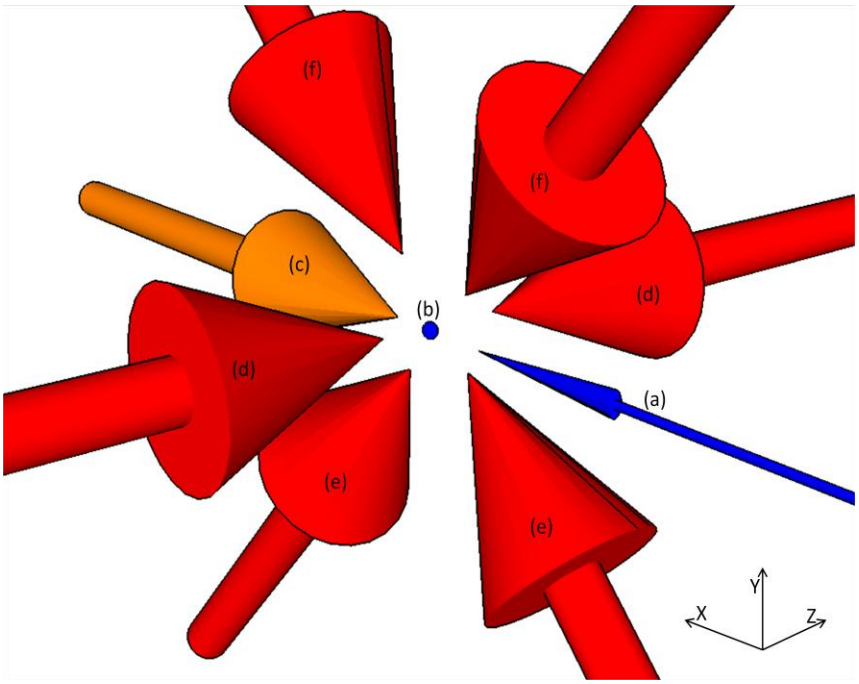

Figure 3-3. *MOT chamber beam geometry*

a) atomic beam from oven, b) MOT, c) Zeeman slowing laser beam, d) Horizontal MOT beams, e) 'down' MOT beams, f) 'up' MOT beams.

3.1.4. Optical lattices

We will discuss the generation of the optical lattices in Section 3.3, but for now let us review the atomic physics which lead to an atom trap. For now, take it as a given that the lattices are a pair of standing wave beams with a waist radius of $\omega_0 = 580$ μm and per beam power of 100 W with a wavelength of 1064 nm. They are lattices because they actually form a stack of pancake shaped traps separated by 532 nm.

The 1064 nm light is far detuned from the D_1 (894 nm) and the D_2 (852 nm) lines of Cs and thus does not significantly scatter. The optical dipole force on an atom from a red-detuned beam of light creates a conservative trap that attracts the atoms to the high intensity regions.

The peak intensity of the light can be found from the circulating power with the following equation:

$$I_0 = 4\left(\frac{2P}{\pi\omega^2}\right) \tag{3.1}$$

Where P is the power, and ω is the beam waist. The 4 comes from the fact that the beam is a standing wave, and the term in parenthesis is for a Gaussian beam. The trap depth can be calculated with (Metcalf and van der Straten, 1999):

$$U_0 = \frac{hI_0}{16\pi\, k_b} \sum\left(\frac{\Gamma_0}{I_{sat}*\delta}\right) \tag{3.2}$$

The sum is taken over the relevant transitions, which in this case are the D_1 and D_2 lines. Γ_0 is the line-width of the atomic transition, I_{sat} is the saturation intensity of the transition, and δ is the detuning of the trapping light from the atomic transition. h and k_b are Planck's and Boltzmann's constants. The result is in Kelvin. Equation (3.2) gives a trap depth of 150 μK for 100 W circulating power.

In the axial (y) direction the potential along the pancake stack takes the form:

$$U = U_0 Sin^2(ky) \tag{3.3}$$

where k is the wave-vector of the trapping light. If we take the derivative of this with respect to the y direction we obtain the force:

$$F = -\frac{\partial U}{\partial y} = -2kU_0 Cos(ky)Sin(ky) \tag{3.4}$$

If we expand this around $y = 0$ we can obtain a spring constant k_{sp} ($F = -k_{sp}y$). This spring constant gives us the axial trapping frequency:

$$\omega_{ax} = \frac{2\pi}{\lambda}\left(\frac{2U_0}{m}\right)^{1/2} \tag{3.5}$$

where λ is the wavelength of the light, and m is the mass of Cs. In the radial directions (x and z), the profile has the form of a Gaussian:

$$U = U_0 e^{-2r/\omega_0} \tag{3.6}$$

If we follow the same prescription we can obtain a radial trapping frequency of:

$$\omega_r = \left(\frac{4U_0}{m{\omega_0}^2}\right)^{1/2} \tag{3.7}$$

Using these equations, a 150 μK trap with a ω_0 = 570 μm has an axial trapping frequency of 130 kHz and a radial trapping frequency of 53 Hz.

3.1.5. MOT overlap with optical lattices

The experiment requires atoms in both cavities simultaneously. The atoms can be alternately launched into the two cavities and re-trapped at the top. Multiple launches into each cavity can provide a few cm long 1-D arrays of atoms. Our two optical lattices are separated by 1 cm along the z direction so we must have the ability to shift the MOT to these two different locations. Because the MOT coil axis is oriented along the z direction, the center of the MOT can be shifted along the z direction by adjusting the current in the coils. This changes the location of the magnetic field zero which is where atoms will collect in a MOT.

However, this poses strict requirements on the beam uniformity and overlap because the effects on the optical molasses cooling for imbalanced beams can be greatly exaggerated on the edges of the beams. These effects can become particularly enhanced during the launch procedure, where the atoms necessarily travel further from the center of the beams.

In order to mitigate these effects, each MOT beam is sent through an optical fiber to clean up its mode profile. They are then expanded with aspheric lenses to a waist radius of 10 mm. The mirrors directing the beams to the MOT chamber are 2” diameter, and great care is taken to ensure that the beams do not clip on anything. Also, neutral

density filters are used, when independent control from the AOM is not available, to ensure that the power imbalance of all beams is < 5%.

The MOT beams are aligned to be centered in the middle of the two lattice locations. Then the atoms are loaded from the Zeeman slower into the center location, typically for a few hundred ms. After a sufficient number of atoms has been collected, the MOT coil currents are ramped to the values that have been optimized to overlap the MOT with the optical lattice.

The MOT magnetic fields which give us good overlap with the lattices are found experimentally by adjusting the MOT currents, releasing the atoms, and measuring the amount of atoms left in the trap 30 ms after release compared to the initial number at that location. When fully optimized, 80% of the atoms loaded from the Zeeman slower to one of the lattice locations can be transferred into the lattice.

The atoms are released into the trap by ramping the MOT magnetic fields down to zero over 5 ms, while keeping the MOT beams at full intensity. The MOT beams now provide polarization gradient cooling for the atoms in the lattice.

3.1.6. Launch

The atoms are launched using the technique of moving optical molasses. The launch and re-trap procedure is described in Fang and Weiss (2009), but at the time of that work the experiment contained only one optical lattice and no electric field plates. Essentially, when a frequency difference is introduced between the ‘up’ and ‘down’ beams, the polarization gradient cooling mechanism cools the atoms into a frame of reference that is moving. Consider the ‘up’ beam frequency fixed at ω_0 and change the

frequency of the ‘down’ beam by δ. The ‘horizontal’ beams are always kept at the average frequency of the ‘up’ and ‘down’ beams.

Now consider the frame of reference moving upwards at a velocity, v. The frequencies of the ‘up’ and ‘down’ beams will be given by the first order Doppler shift:

$$\omega_{up} = \omega_0 + k\, v\, Cos(\theta)$$

$$\omega_{down} = \omega_0 + \delta - k\, v\, Cos(\theta) \tag{3.8}$$

Where k is the wave-vector of the light, and θ is the angle that the beams make with respect to vertical. There is a frame of reference in which $\omega_{up} = \omega_{down}$. In that frame, the atoms see a stationary three dimensional light field which is perfectly suitable for polarization gradient cooling and they will be cooled into that frame. In the lab frame, they will be launched with a velocity v. In our MOT, θ is π/4, and k = 2π / (852 nm). Solving for the velocity that makes $\omega_{up} = \omega_{down}$ we get:

$$v = \frac{\delta}{\sqrt{2}k} \tag{3.9}$$

In order for the atoms to properly follow the frame of reference, we use a several step procedure that is detailed in Figure 3-4. After we load atoms into the lattice we increase the detuning to -17 MHz and reduce the MOT beam intensity to 75 μW/cm^2 during the ‘cool’ stage. This cools the atoms to ~10 μK. During the ‘launch’ stage, we switch back to an overall detuning of -13MHz. The frequency of the ‘down’ beams with respect to the ‘up’ beams is linearly ramped from 0 to 6.75 MHz over 2.5 ms. Using Equation (3.9) this gives a velocity at the end of the ramp of 4 m/s. During the frequency ramp of the ‘launch’ stage we wish to bring as many atoms as possible into the moving frame. To do this, we use a relatively small detuning and large intensity to ensure the atoms remain within the capture velocity of the polarization gradient cooling.

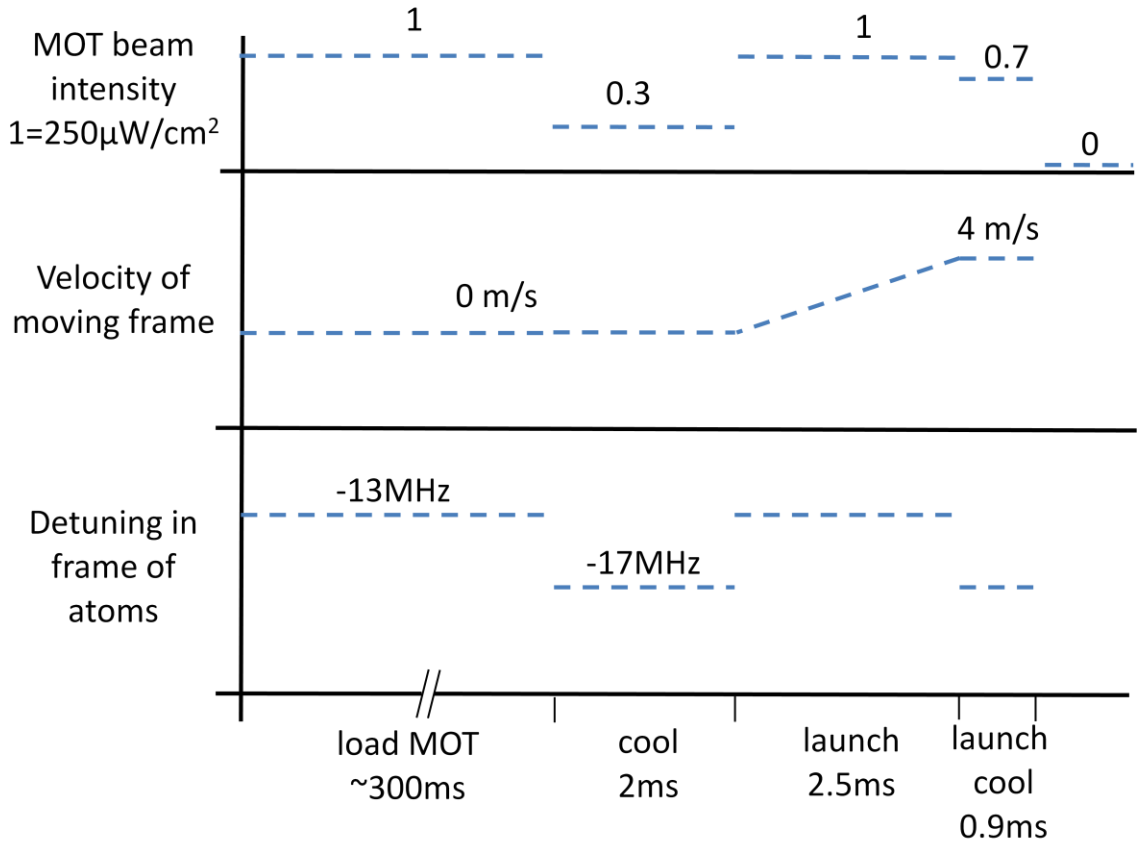

Figure 3-4. *Launch sequence*

The graphs in Figure 3-5 show that if the time of the linear ramp is too fast, then most of the atoms will not move at the final velocity. For slower ramps, at the end of the ramp the atoms move with the final velocity of 4 m/s. However, if the ramp is performed too slowly, the atoms will move out of the center of the beam before they are moving at the final velocity.

Then, during the 'launch cool' stage, the frequency difference between the 'up' and 'down' beams is kept fixed, but the overall detuning to the atomic resonance is increased to -17 MHz and the intensity is lowered to ~175 μW/cm^2. The purpose of the 'launch cool' stage is to cool the atoms as effectively as possible in the moving frame.

After 0.9 ms, the cooling beams are abruptly turned off. If this is not done, as the atoms near the edge of the cooling beams they will experience a low intensity and will reach the décrochage regime such that the light produces heating rather than cooling (Hodapp, *et al.*, 1995). The details of how we actually generate the RF frequencies for the AOMs are given in Fang (2007, pp. 120-122).

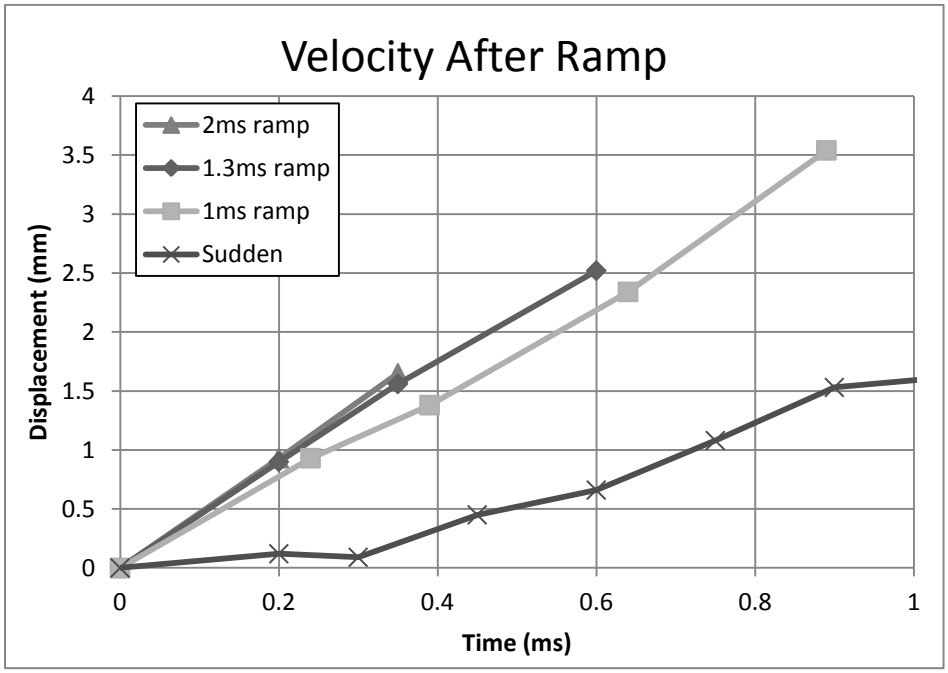

Figure 3-5. *Dynamics of launch*

This shows the displacement of the atom cloud as a function of time for ramps to 4.4 m/s of varying length. T = 0 is defined as the end of the ramp.

3.2. Re-trapping atoms in measurement chamber

3.2.1. Measurement chamber optics

Before we describe the re-trapping and cooling in the measurement chamber, let us first describe the optics of the measurement chamber. Because these optics are all inside the magnetic shield and are close to the atoms, they must be made of all non-

magnetic and preferably low-conducting materials in order to reduce Johnson noise. The materials used are glass, plastic, and some titanium where it is unavoidable. All of the horizontal beam optics are mounted on two plastic platforms inside a plexiglass cylinder. The light for the cooling is brought from the table to the measurement chamber in two optical fibers.

For non-critical mirrors and beam splitters, plastic mounts are used. Where more control is desirable, home-made titanium mounts are used. One example is shown in Figure 3-6. The entire mount is made of titanium, and the springs are non-magnetic phosphor bronze. These are described in more detail in Ebert (2007). The fibers are polarization maintaining single mode fibers with FC/APC connectors. The output of the fiber is a home-made output coupler where a bare fiber is positioned with respect to a collimating lens and is potted in place with epoxy as can be seen in Figure 3-6. The fiber can also be rotated to align with the correct polarization before it is glued in place.

After the beam from the fiber is collimated it is sent through a polarizing beam splitting cube to clean up the polarization. Then the beam goes through an aspheric f = 2.5 cm lens whose purpose is to expand the beam. After expanding, for 12.5 cm, the beam goes through an f = 10 cm cylindrical lens which collimates it in the horizontal direction at a $1/e^2$ intensity radius of 7.2 mm, and allows it to continue expanding in the vertical direction. The beams then bounce off several mirrors on their way to the measurement chamber so that at the atoms, the beam has a vertical radius of 7.2 cm. There are two fibers in the measurement chamber. One provides light that is polarized in the S direction and the other in P.

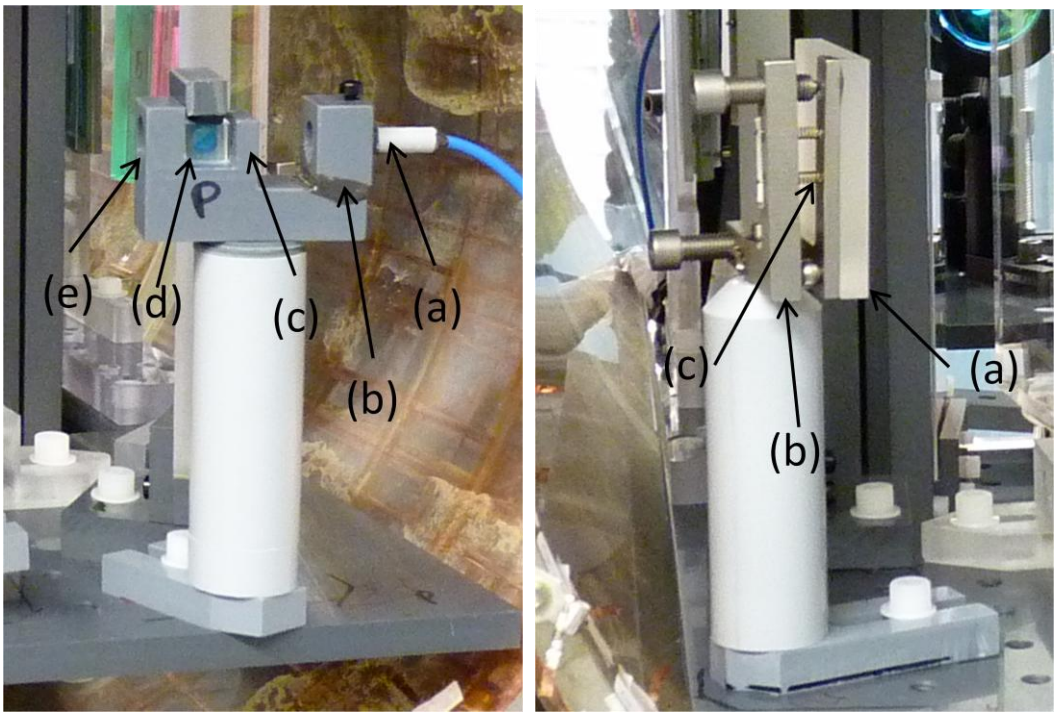

Figure 3-6. *Custom nonmagnetic optics*

Left: Home-made fiber output coupler. a) strain relief for bare fiber, b) housing for bare fiber that is potted in place, c) collimating lens, d) polarizing beam splitting cube, e) expanding lens. Right: Home-made titanium mirror mount, a) mirror mount, b) titanium L-shaped mount and titanium screws, c) phosphor bronze springs.

The S and P beams come from two opposite sides of the plexiglass cylinder and before the measurement chamber they are split so that one beam of each polarization goes to each side of the electric field plates. Currently these beams have a maximum intensity of about 1 mW/cm^2 at the atoms. The two horizontal directions for polarization gradient cooling are provided in the following way. The center plates are highly reflective on both surfaces, while the outer plates are anti-reflective on both surfaces (as described in 0). As seen in a top view of the measurement chamber in Figure 3-7, one beam provides two separate directions of cooling light on the atoms, represented by the green spots. The first direction is the incoming light, and the second direction is the

beam which is reflected from the highly reflective center plate. These are matched by beams from the opposite side. The beams have a 30 degree angle of incidence (AOI) on the plates.

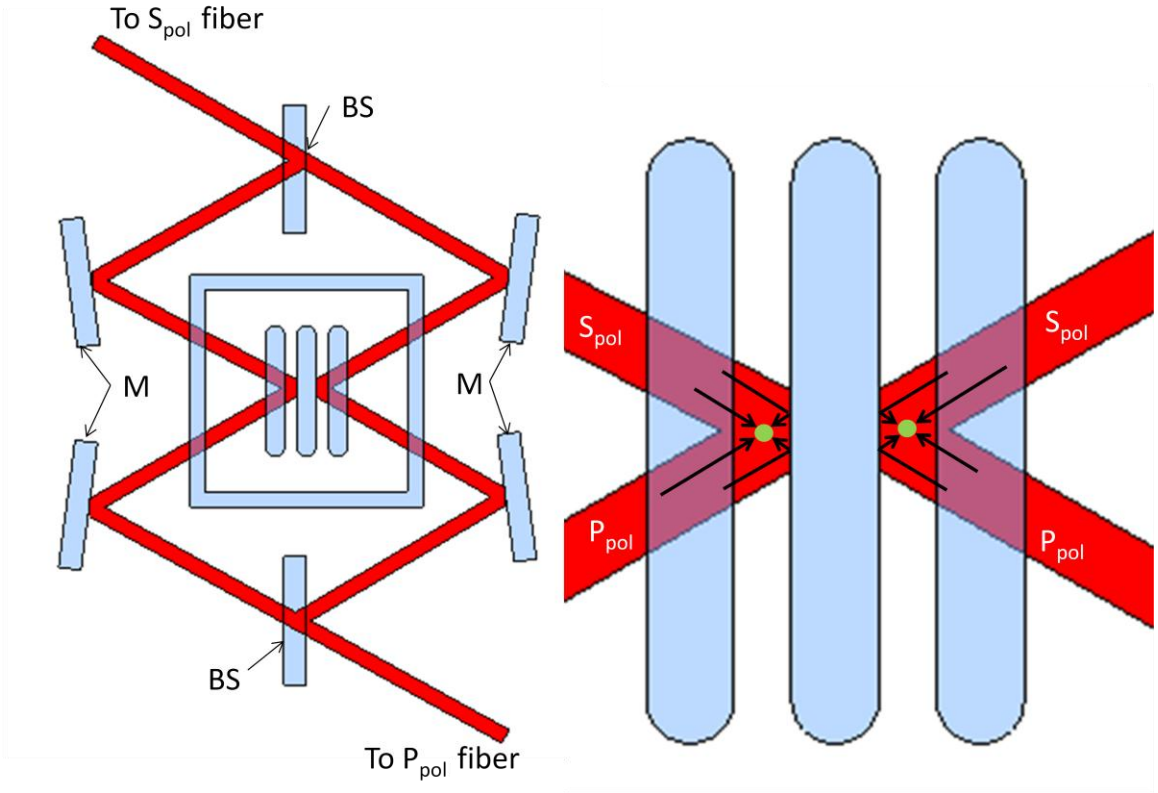

Figure 3-7. *Horizontal cooling beams on plates*
BS = beam splitter, M = mirror.

The vertical cooling is provided by a pair of collimated 1mm radius beams that enter the top and bottom vacuum windows. The beams enter the windows close (~1 cm) to the cavity beams. A pellicle beam splitter is used to align the cooling beams such that they are overlapped with the cavity at the position of the atoms in the measurement chamber. The top vertical cooling beam is linearly polarized and the bottom is circularly polarized. The bottom cooling beam will later serve as the probe for measurements of

the atoms in the measurement region. This beam is used because it can be easily tuned to resonance and the atomic scattering rate can be saturated. These beams have a maximum intensity of ~80 mW/cm^2. This beam configuration gives good polarization gradients for cooling in all three directions.

3.2.2. Imaging systems

For the majority of data discussed in this work, the atoms were fluorescently imaged onto a CCD camera (JAI, CV-A55 IR). This will not be the final imaging system for the EDM measurement. The imaging systems utilizes a 1/3 magnification with an f = 6 lens situated 24.6 cm from the atoms in the x direction (see Figure 3-8). The 1/3 magnification allowed both lattices, separated by 1 cm, to be imaged onto a single CCD camera with a 6.45 mm by 4.84 mm active area.

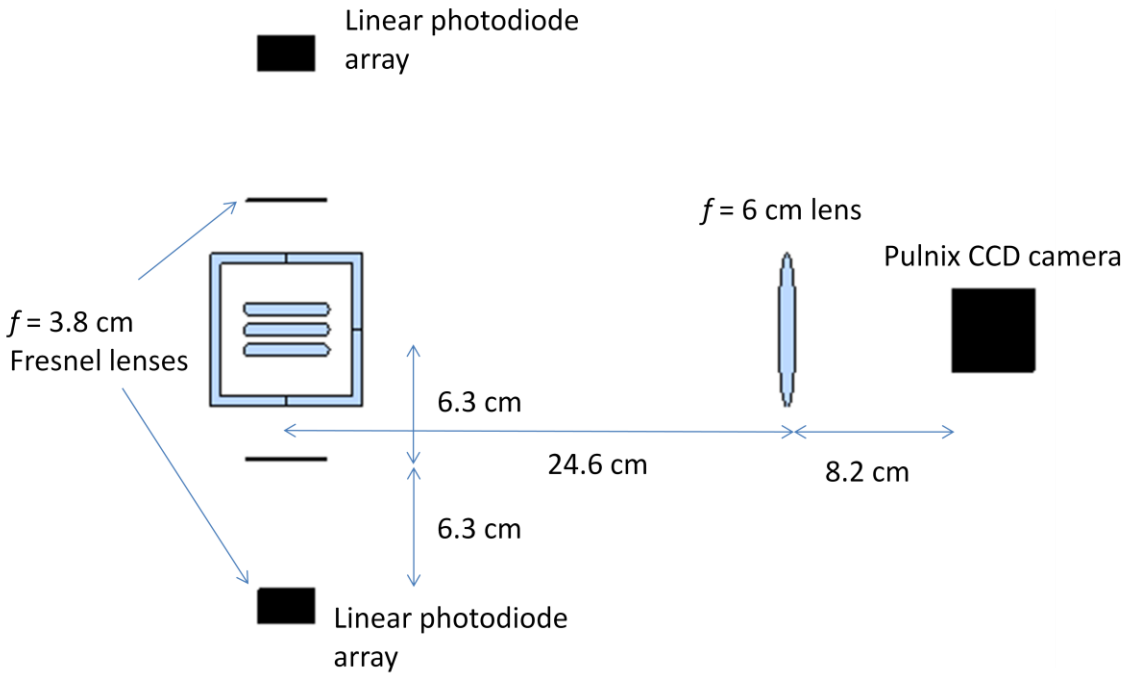

Figure 3-8. *Imaging systems*

The spatial resolution of a CCD camera is very useful when we want to know the width or position of the atomic cloud. An example image from the CCD is given in Figure 3-9. Here, the atoms are probed with the vertical cooling beam when they are near the top of their trajectory, before any cooling pulses have been applied to stop them and trap them in the lattice. In the bottom half of Figure 3-9 the image has been integrated along the vertical direction to obtain a horizontal atomic distribution. Unfortunately, the CCD must be removed from the magnetic shield during the final eEDM measurement because the body of the camera contains magnetic elements.

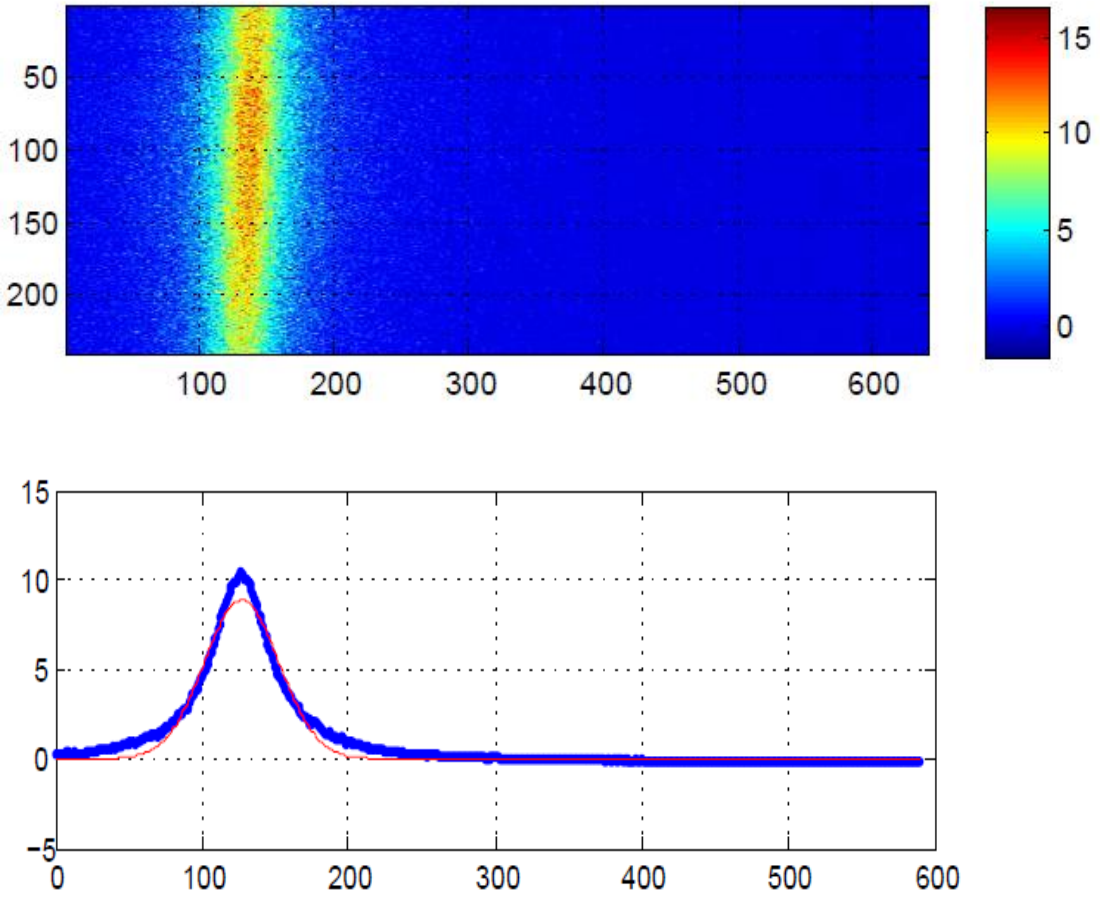

Figure 3-9. *Launched atoms imaged on the CCD camera*

Top: False color image of launched atoms before they are stopped and re-trapped. Bottom: a horizontal distribution found by vertically integrating the false color image. The red line is a Gaussian fit to the data.

For the eEDM measurement a completely non-magnetic imaging system must be used. For this purpose, a second system utilizes 1:1 imaging with a Fresnel lens located ~6.3 cm from the atoms in the z direction. The Fresnel lens focuses the light from the atoms (and from the reflection of the atoms off of the center electric field plate) onto a linear photodiode array (see Figure 3-8). Commercial photodiodes typically contain ferromagnetic materials. For our purpose, a completely non-magnetic photodiode array was developed. The photodiode array is a custom-designed non-magnetic array with individual photodiodes based on an Advanced Photonics photodiode (150-25-002D). Each photodiode array contains 25 vertically aligned photodiodes with an active area of 3.2 mm by 4.7 mm separated by 0.5 mm. Each photodiode has an individual cathode and anode which allows their signals to be brought out of the magnetic shield with a 2 m long mini-coaxial cable, and then amplified by a low noise, high gain, bootstrapped trans-impedance amplifier (Zhu, Solmeyer, and Weiss, 2012). It is estimated that this system will give a signal to noise ratio for the eEDM measurement of $3.7*10^3$ in each channel.

We use a Fresnel lens because we desire to collect as much light as possible in a location that is highly constrained for space from the horizontal cooling optics. The Fresnel lens design allows a thin lens with a short focal length (3.8 cm) to have a large collection area. Our Fresnel lens has a diameter of 6”, but is cut horizontally to a width of 1.6” so that it does not interfere with the horizontal cooling optics. A conventional lens of this size would be prohibitively big. The Fresnel lens comes at the cost of reduced

optical quality, but due to the size of the photodiodes and the fact that we will have a necessarily blurred image of the atoms and their reflection from the center plate, optical quality is not a stringent requirement. Even with the large size of the photodiodes, the current Fresnel lens imaging system is plagued with focusing issues that spread the atomic signal from one point over several photodiodes. A project is currently underway that will hopefully alleviate this problem.

3.2.3. Re-trap

We launch the atoms so that the top of their trajectory is at the center of the measurement chamber. When the atoms reach their apex we pulse on the cooling beams. When the atoms are stopped in the trap, they do not immediately fall into the trap's center because of the damping force associated with the optical molasses. The graphs in Figure 3-10 show the dynamics for two different iterations of the experiment. The atoms are launched and stopped, and then probed after a variable amount of time. The line of atoms is fit to a Gaussian and the peak value, the FWHM, and the location of the center is plotted for an average over a 1 cm vertical spread of atoms.

The first three graphs are the results obtained in October 2011. In this case, the loss is due to atoms not being stopped by the molasses, which can be seen by the sharp initial decline in the first 5-10 ms of the graph of the peak. The number of atoms stopped could be improved if the horizontal beam intensities were increased. We see by measuring the number of atoms stopped as a function of the horizontal beam intensity. Even as we approach our maximum intensity, the number of atoms stopped is still linearly increasing.

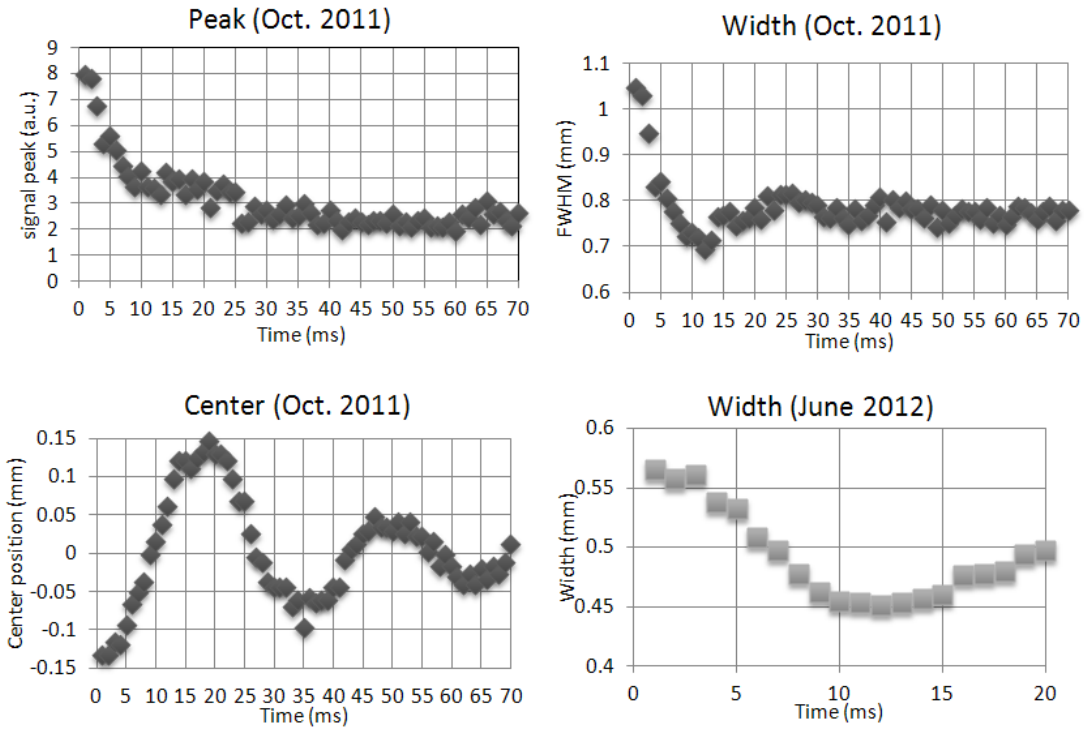

Figure 3-10. *Dynamics of re-trapping*

In addition, the atoms slosh back and forth in the trap, as can be seen in the graph of the center position of the atoms. By looking at Figure 3-7, it is clear that the atoms start off center in the horizontal beams. There are also interference fringes on the horizontal beams which come from the uncoated fused silica surfaces of the glass cell. These factors result in an unknown, time-varying, and unavoidable amount of imbalance of the cooling beams at the location of the atoms, which likely causes a pushing force that traps the atoms off center.

The atoms also have a breathing mode, as can be seen by the oscillation of the width. If we wait 10ms after the stopping pulse, the atoms have both sloshed to the center of the trap and their width is at a minimum. At this point we can pulse on a second

cooling pulse which locks in the center position and width. Multiple such cooling pulses ultimately provide a colder sample.

After the magnetic shields were partially installed in June 2012 (see Section 4.2.5), all of the optics in the cooling region had to be re-aligned. In this iteration there was no measurable sloshing mode, though the breathing mode remained (see Figure 3-10). This was presumably because there was a more favorable beam intensity balance.

For the June 2012 setup, the breathing mode reached a minimum width at 12 ms. After the second cooling pulse, another breathing oscillation occurred, albeit with a smaller initial width and a smaller amplitude. A third and final cooling pulse was added after waiting an additional 12 ms to optimize the cooling.

In the end, all beam intensities were optimized experimentally. The initial stopping pulse uses a relatively high intensity with a detuning of -13 MHz. The vertical beam is ~8 mW/cm^2 and the horizontal beam intensity is ~1 mW/cm^2 and the stopping pulse was 0.7 ms long. The subsequent cooling pulses were optimized with smaller intensities, around 0.5 mW/cm^2 for all beams, for about 1 ms each. This resulted in an atom cloud that had a FWHM of 300 μm as can be seen in Figure 3-11. The blue lines on the vertically integrated graph (lower) show the fitted FWHM and the center of each peak.

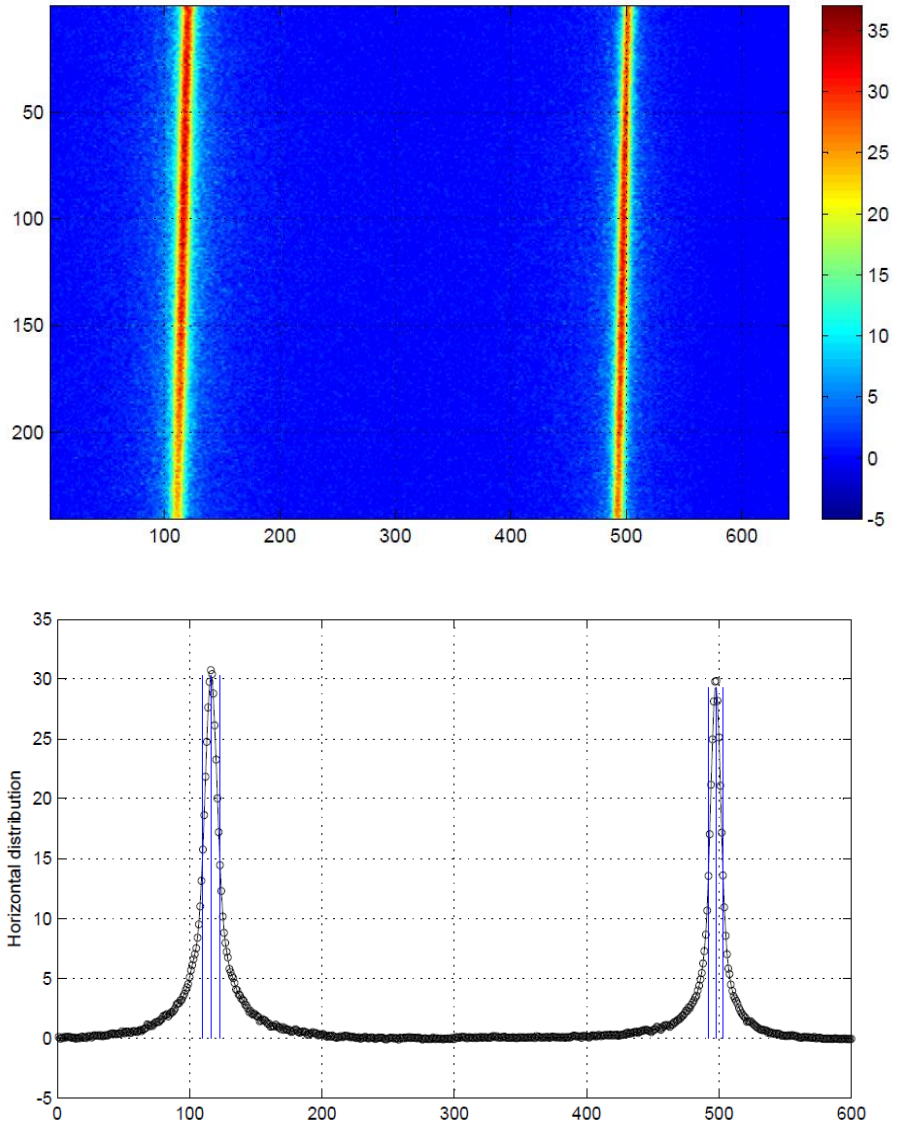

Figure 3-11. *Atoms re-trapped and cooled in measurement chamber*

In the measurement region, the light in the optical cavity has a waist radius of 580 μm and a trap depth of 100 μK. The temperature of the atoms re-cooled in the measurement chamber can be calculated by setting the potential energy associated with the atomic width in the harmonic trap equal to the thermal energy,

$$k_b\, T = \omega^2\, m\, \sigma^2 \tag{3.10}$$

where m is the mass of Cs, ω is the radial trapping frequency, and σ is the Gaussian width which can be found from the FWHM. Inserting the measured FWHM of 300 μm into Equation (3.10) corresponds to at temperature in the trap of ~20 μK.

We estimate that we trap a total of $5*10^6$ with a peak density of $4*10^{10}$ cm^{-3}, though these could be off by a fair amount due to the fact that this calibration was taken with the imperfect Fresnel imaging system described above . As mentioned before, the total number of atoms re-trapped could be increased by increasing the power of the horizontal cooling beams. This could be accomplished with a modest change to the laser system by installing a tapered amplifier into the path of the cooling lasers. Additionally, the MOT could be loaded faster if transverse polarization gradient cooling beams were added to the Zeeman slower directly after the oven nozzle. If atom number ever becomes a limitation, either of these can be implemented with relatively modest changes.

3.3. Cavities

Up until now, we have treated the optical cavities as providing two 1-D traps without describing them in any detail. We shall do so here. The basics of this system have been described in Fang (2007) but there are some notable differences which will be covered below.

3.3.1. Optics

The 1064 nm light used for the optical lattices is generated by YAG laser from Lightwave Electronics (Model M126-1064-100). The light is then increased up to a

maximum of 10 W with IPG Photonics fiber amplifier model YAR-10-1064-SF-PM. The light from the fiber amplifier is split into two parallel beams.

These beams are sent into the two parallel Fabry-Perot cavities whose internal field constitutes the optical trap. The cavities are nearly confocal to ensure that the degeneracy of the TEM_{00} and other nearby modes is lifted. Each cavity is composed of two mirrors with radii of curvature of 2 m and a length, L, ~2.05 m. The cavities have a Free Spectral Range (FSR) of $c/(2L)$ = 75 MHz, where c is the speed of light. The polarization of the cavities is linear and is P-polarized with respect to the Brewster plates. Note that this polarization also aligns with the z-axis in our lab coordinate system (i.e., the direction of the electric field). We have recently embarked on a more precise alignment of the cavity polarization, but its description will be given in Zhu (*forthcoming*).

The cavity mirrors are outside of the vacuum chamber and pass through two vacuum windows. The cavities also thread the three electric field plates. A schematic of the cavities is shown in Figure 3-12.

In this figure, we can see the input beams from the fiber amplifier (a). They pass through the input cavity mirrors (b) which have a transmission coefficient of T_{in} = 0.007 and a radius of curvature of 2 m. The top cavity mirrors (c) have a transmission coefficient of $T_{out} = 3.3*10^{-4}$ and a radius of curvature of 2 m. Both the top and bottom cavity mirrors are cut into a D-shape so that the beams can be at the center of the curvature even through the cavities are separated by only 1 cm. This minimizes a possible misalignment that could arise if the beams traversed the input mirror off center, causing the beams to be refracted.

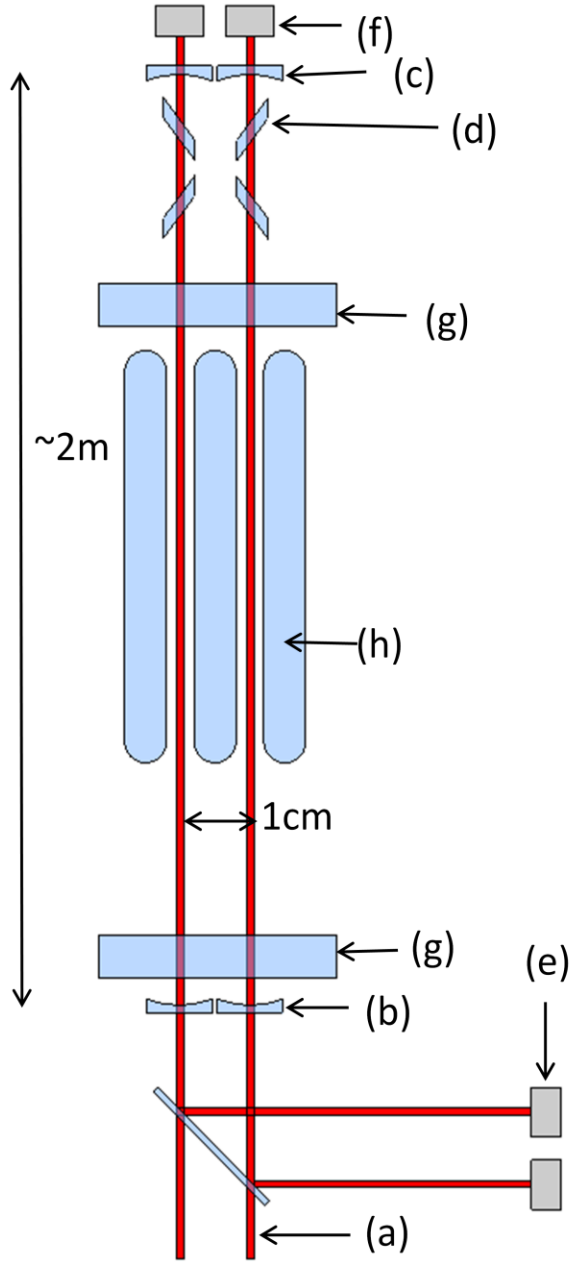

Figure 3-12. *Schematic of optical cavity*

a) input beams from fiber amplifier, b) bottom cavity mirrors T_{in} *= 0.007, c) top cavity mirrors* T_{out} *=* 3.3×10^{-4}*, d) Brewster plates, e) photodiodes for monitoring reflection for PDH lock, f) photodiodes for monitoring cavity transmission, g) infrasil vacuum windows, h) electric field plates.*

The cavity locking will be described in the next section, but for now I will describe the elements that are necessary for monitoring and controlling the cavity. Each cavity contains a pair of Brewster windows mounted on galvanometers (d). These are used to control the cavity length. They are at Brewster's angle so that the cavity polarization is in the P direction in order to minimize losses due to reflection. The top cavity mirrors are mounted on a piezo-electric transducer (PZT) crystal which are also used to control the cavity length. The two sets of photodiodes (e) and (f) are used to monitor the reflection from the input mirror for the locking scheme, and monitor the cavity transmission as a measure of the power circulating in the cavity.

Finally there are several elements in or around the cavities that do not serve any purpose for them, but are there and can potentially have an effect on them. The elements which can have the largest potential influence on the cavity are the vacuum windows (g). These can cause cavity loss either through absorption, reflection, or by the effect of birefringence. Absorption was a problem when normal fused silica was used, but switching to Infrasil, which has the OH removed from the glass, eliminates the OH absorption line that occurs near 1064 nm. The windows are also AR coated to minimize reflection. If there is birefringence on the windows, the polarization is rotated and there is a greater loss due to reflection from the Brewster windows. This can be detrimental. It and its solution will be described more in Sections 3.3.5 and 3.3.6. The electric field plates (h) nominally do not have any influence on the cavity. But they do create a slit that is 4 mm wide and 30.5 cm long through which the cavities must be aligned.

3.3.2. Cavity locking

The cavities are locked using the Pound-Drever-Hall (PDH) locking scheme (Drever *et al.*, 1983). In this scheme, the input beams pass through an electro-optic modulator. This modulates the phase of the input beams at 9.85 MHz which puts sidebands on the carrier frequency. The reflection from the cavity is captured on a fast photodiode (FND-100). The signal on that photodiode is a combination of the carrier and the sideband frequencies. When this signal is mixed with the local oscillator, it gives an error that can be used to determine how far the carrier frequency is from the resonance of the cavity. The details of the error signal and the locking electronics are given in Fang (2009).

The signal from the PDH electronics is fed back to a two-band servo system which locks the cavity length to the frequency of the laser light, allowing the cavity to remain in resonance. The Brewster windows on galvanometers provide feedback in the low frequency region, 0 to ~500 Hz. When the galvanometers rotate the Brewster plates so that the cavity beam path through the glass changes, it alters the optical length of the cavity. Using a pair of Brewster windows that rotate in the opposite direction ensures that changing the cavity length does not add a transverse displacement of the beam. The use of galvanometers in the low frequency band is necessary because in the low frequency band the large amplitude of the length noise is inaccessible to the PZT. The Brewster windows provide a feedback capable of tuning the cavities over several FSRs.

PZTs change their length when a voltage is applied to them. The PZTs mounted on each top cavity mirror (Noliac CMAR04) are ring shaped to allow the transmission of the cavity to be collected on a photodiode. A driver based on the Cirrus Logic high current operational amplifier PA16 was built to provide the feedback. It includes multiple

tunable notch filters to lower the response of electronic resonances in the PZT response function. The driver will be described in more detail in Zhu (*forthcoming*). The PZTs provide feedback in the region from 0.2 to 50 kHz.

The two-band feedback is provided by a custom-built control box. The box has a completely tunable proportional, integral, and differential (PID) lock for each frequency band for each cavity. The roll-off frequency for the low frequency band is also tunable. The circuit diagram for the lock circuit is given in Appendix B.

Because each cavity must be locked independently and their noise spectra are different, it is not possible to implement the alternative scheme of controlling the laser frequency with a PZT internal to the laser.

3.3.3. Mechanical resonances and damping

The high frequency feedback of the PZTs can induce a mechanical vibration on the mirror mounts. This will mostly only affect the cavity at mechanical resonance and anti-resonance frequencies particular to the mirror mounts. These resonances were characterized using the transfer function of the servo system. To measure the transfer function, we add an oscillating voltage V_{in} to the error signal after the PID circuit but before the driving electronics. Then we measure the error signal V_{err} while the cavity is loosely locked. The ratio V_{in}/V_{err} is proportional to the gain of the servo. We can also monitor the relative phase between V_{in} and V_{err}. A typical transfer function is shown in the un-damped curve of Figure 3-13.

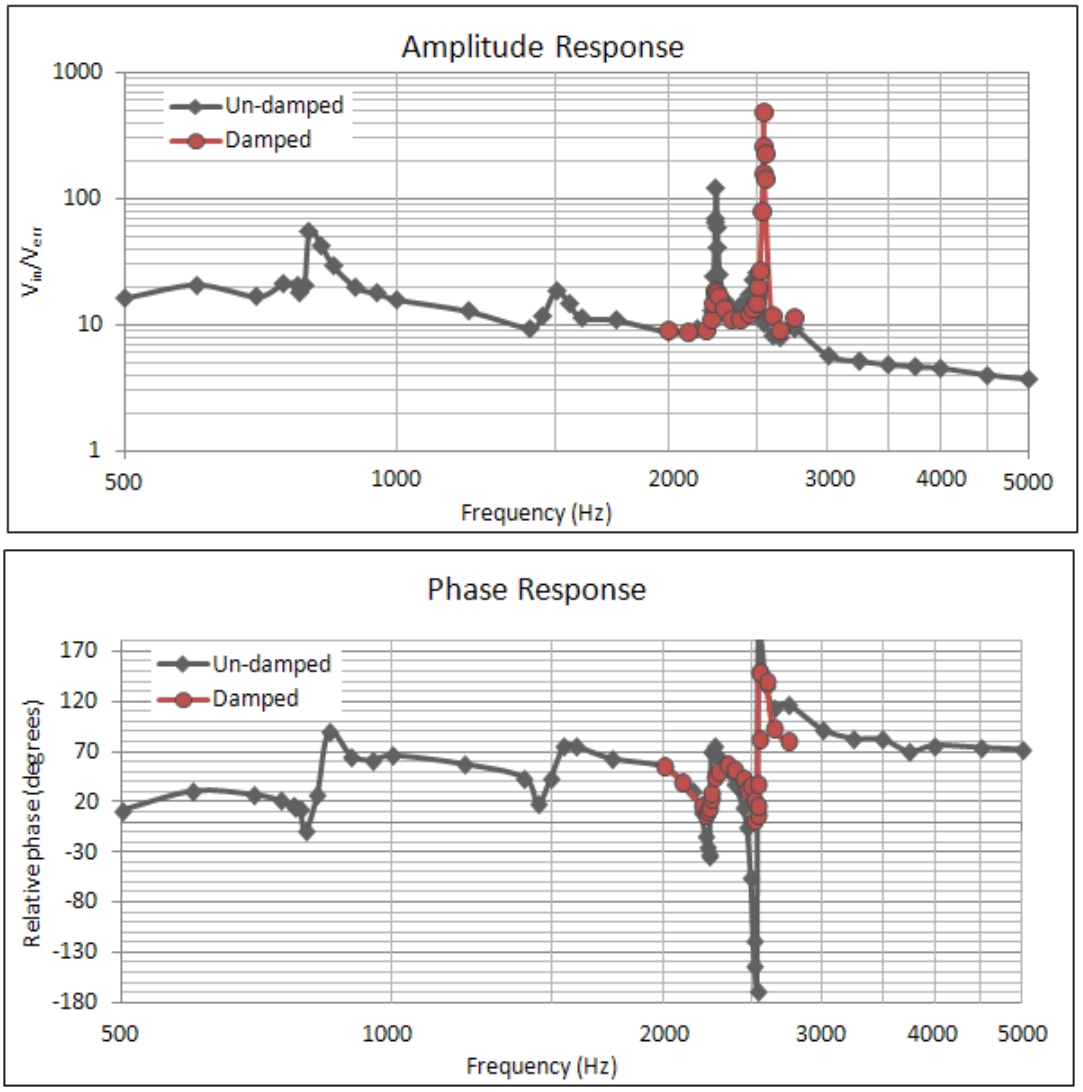

Figure 3-13. *Cavity transfer function*

As can be seen in the figure, a mechanical resonance shows up as a sharp peak in the amplitude response. There are two prominent resonances in this transfer function at 2255 Hz and 2525 Hz. What turns out to be more illuminating is the response of the phase. In the un-damped curve of the phase response, we can see that at the 2525 Hz resonance the phase response lags by more than 180 degrees so that it wraps around back to the original phase delay. This means that near the resonance, the feedback has the wrong sign. This type of phase wrapping make it impossible to lock the cavity.

In order to solve this problem, passive damping was added to the cavity mirror mounts that hold the PZTs. The damping was achieved by clamping down a piece of sorbathane between the clamp and the mirror mount. Sorbathane is a very pliable rubber that absorbs vibrations but keeps its own volume constant, such that once it has had a chance to settle there should be relatively little drift. Several types of damping were tried on the mirror mounts, such as damping from the top of the mount to the base plate breadboard, and damping between the front plate of the mirror mount and the back plate.

After trial and error, appropriate pressures and damping geometries could be found which alter the transfer function to the damped case as shown in Figure 3-13. It is notable that even though the amplitude response can still show a sizable resonance, as long as the phase response does not wind around a full 360 degrees, the cavity will be lockable. When the damping, alignment, and the lock parameters are optimized the optical cavities can stay locked for a day with ~1% intensity fluctuations.

3.3.4. Characterization and build-up

The build-up factor of the cavity is defined as:

$$B = \frac{P_c}{P_{in}} \tag{3.11}$$

Where P_c is the 1-way circulating power in the cavity, and P_{in} is the input power. P_{in} is known, and P_c can be measured directly with the transmission of the top cavity mirror. The build-up factor can be related to the cavity finesse and cavity loss with the following equations (Ma, Ye, Dubé, and Hall, 1999):

$$B = \frac{F^2}{\pi^2} T_{in} \tag{3.12}$$

Where T_{in} is the transmission of the input mirror (.007) and the cavity finesse is defined as:

$$F = \frac{FSR}{\gamma_c} \tag{3.13}$$

Where $\gamma_c$is the cavity line width FWHM. This can be measured directly by scanning the galvanometers across a cavity resonance and measuring the cavity line width and FSR on the same pass. The finesse is also related to the loss in the cavity through the following equation (Hood, Kimble, and Ye, 2001):

$$F = \frac{2\pi}{T_{in}+T_{out}+l_c} \tag{3.14}$$

Where l_c is the loss in the cavity. In practice, the build-up factors and finesse are directly measured and calculated with Equations (3.11) and (3.13) and Equations (3.12) and (3.14) are used to paint a complete picture of the cavity to check for anomalies and make sure nothing is out of order.

In a typical implementation of the cavities, we can achieve a maximum finesse of 350 and a build-up factor of 25. This gives a one way circulating power of about 100 W. This corresponds to a loss in the cavity of around 1%. However, the exact numbers achieved vary from one implementation to the next. As alluded to earlier, any addition of birefringence can have detrimental effects on the cavities.

3.3.5. Polarization

After the vacuum system was baked in the Fall of 2010, it was observed that the cavity power had been significantly degraded. The finesse had dropped to around 50 and the build-up factor was near 1 (i.e., no build-up). It was determined that the source of this problem was birefringence of the vacuum windows that had changed after the

bake. Birefringence can cause problems because the polarization rotation causes more reflection loss from the Brewster windows. Further, the effect of the birefringence can be very great due to the nature of the build-up. Consider the model of a photon in the optical cavity. In a build-up cavity the photons make many round-trips before being lost. Thus any birefringence inside the cavity will have a compounding effect which rotates the polarization each time the photon makes a pass.

The smoking gun of this effect is a measurement of the reflection of the light from the Brewster plates while the cavity is in lock. When the cavities are not in lock, the total reflection from all four surfaces of the Brewster plates is ~0.2% of the incident power. This is measured with the top cavity mirror aligned to retro-reflection so that the down going beam's reflection can be measured, but before the input mirror is in place. With the input mirror in place, there is not enough power transmitted to measure the reflection accurately. However, when in lock, the reflected power was usually more in the range of 1 to 2% of the circulating power when the more birefringent window mounting scheme was used. When the more birefringent window was misaligned to an unfavorable orientation for the cavity, i.e. when the build-up power was significantly compromised, the reflection from the Brewster plates could be as high as 5 to 7%.

3.3.6. Indium window mounting scheme

Our vacuum windows were originally mounted using a pair of gaskets which had a knife edge machined onto each side based on the designs in Noble and Kasevich (1995) and Crane and Ekstrom (2005). However, as described above, the resulting stress-induced birefringence was too large for our purposes. We developed a scheme

for mounting the windows using indium gaskets as described in Solmeyer, Zhu, and Weiss (2011).

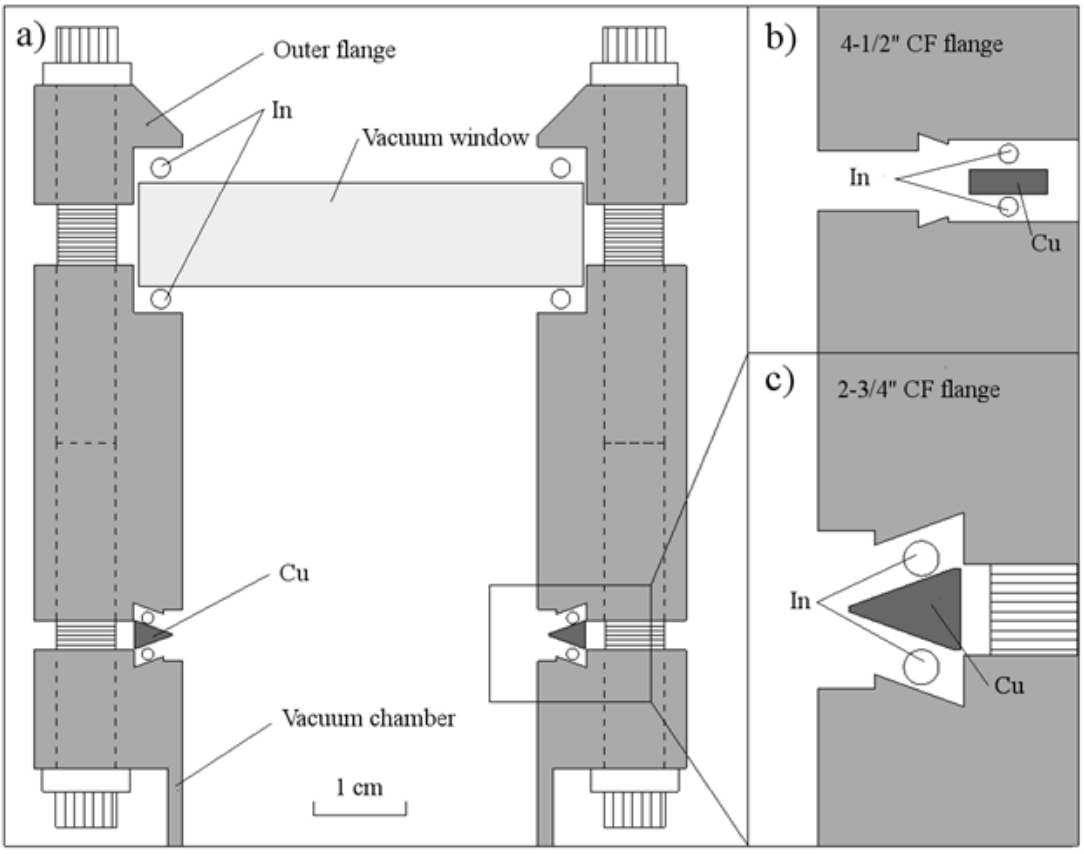

Figure 3-14. *Indiuim window mounting scheme.*

a) The adapter piece and window mounting scheme for a 2-3/4"CF flange, b) A scheme for mounting an indium gasket on a standard 4-1/2" CF flange, c) close up of the scheme for mounting an indium gasket on a standard 2-3/4"CF flange.

The solution involved replacing the copper gaskets with a ring of indium so that the torque required to obtain a vacuum seal is only 12 in-lbs, compared to the mounting scheme with copper gaskets which required as much as 3 or 4 times that amount. The vacuum seal is created when the indium is flattened between the window and a flat surface machined on the flange. This reduction in torque results directly in lower stress-induced birefringence. In addition, we developed a technique to enable this type of

mounting to be done on an existing ConFlat (CF) flange on our vacuum system (which cannot be altered). After lowering the torque required to seal the window, the limiting factor actually came from the stress induced when the flange was attached to the vacuum system on the other side. Changing to low torque indium seals for these flanges, and using thick adapters that do not deform provided additional improvement. The designs are shown in Figure 3-14.

The results of these designs are shown in Figure 3-15. The graph shows the fractional polarization rotation of several different mounting schemes in ppm (parts per million). The fractional polarization is measured by sending a linearly polarized beam through the mounted a window 1 cm from the window center, and measuring the amount of light reflected from a polarizing beam splitting cube after the window compared to the total beam power. The fractional polarization is shown as a function of the angle the window is rotated about its center. Case (a) is for windows mounted with double knife edged gaskets and has a maximum fractional polarization of around $3*10^{-3}$. Case (b) is when the window is mounted with indium, but the adapter is mounted directly to the vacuum chamber with a standard copper gasket. This had a maximum fractional polarization of $5*10^{-4}$. Case (c) shows the results when indium gaskets are also used to mount the adapter flange to the vacuum chamber. This case resulted in a maximum fractional polarization of $2*10^{-5}$, a two order of magnitude improvement over the copper gaskets.

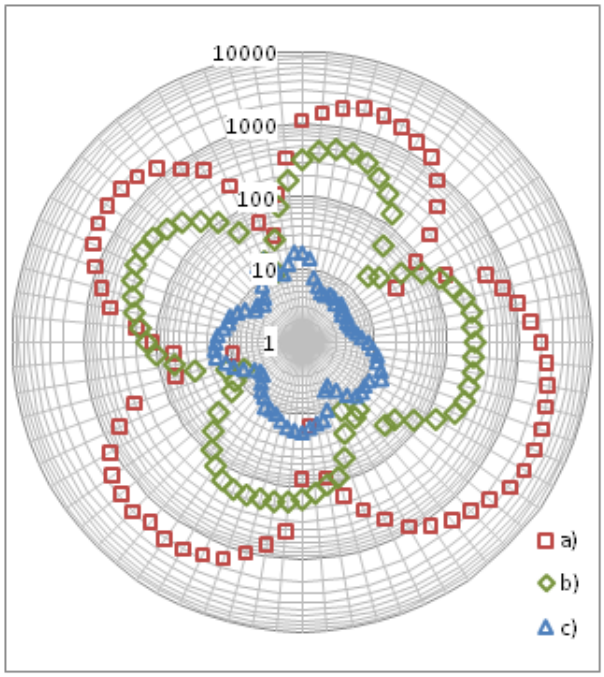

Figure 3-15. *Fractional polarization of vacuum windows*

The polar axis is an arbitrary angle on each measured window. The radial axis is the fractional polarization of the light after transmission of the window in ppm. a) Double knife edged copper gaskets, b) indium sealed windows, c) indium sealed windows in addition to indium sealing to the vacuum chamber.

Indium melts at 156.6°C which sets an upper limit for the temperature of a bake. Because we are reluctant to heat our glass cell and mounted electric field plates much higher than this, there is not much lost by keeping our bakes below 120 °C. The birefringence of the indium-sealed windows was stable under bakes and when installed onto the vacuum chamber, the cavities no longer suffered from problems due to polarization. With the cavity optimized, the power reflected from the Brewster plates while the cavities were in lock could be made as low as 0.05 to 0.07%. By adding fine tune control over all rotation angles of the Brewster plates, this has since been significantly improved (Zhu, *forthcoming*).

Chapter 4. Magnetic Shield

4.1. Theory

4.1.1. A magnetic-resistance model

An intuitive model of magnetic shielding can be constructed using the concept of magnetic resistance. If the magnetic flux lines are thought of like a current, and the magnetic permeability μ is thought of as a conductivity, then magnetic shielding works by concentrating the magnetic flux lines into the paths of least resistance (Jackson, 1962). This idea is illustrated in Figure 4-1. The uniform B field, shown in red, is concentrated in the material with high magnetic permeability, giving a low field inside the shielded region.

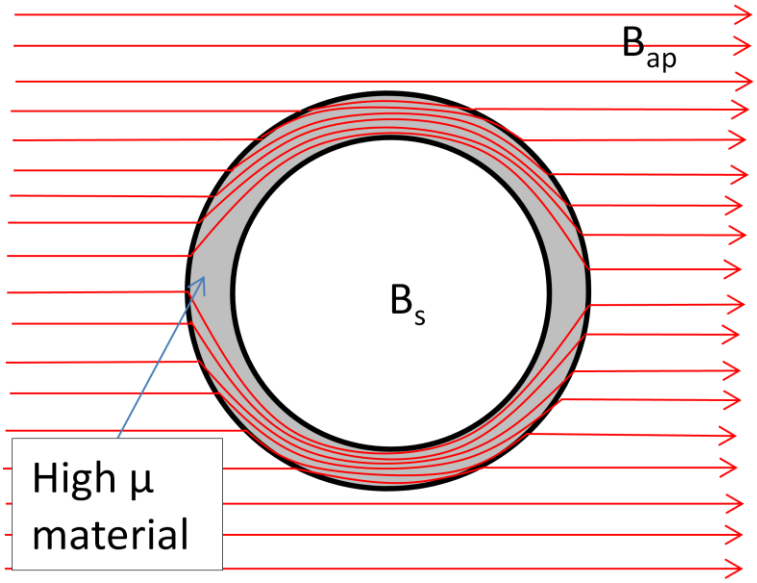

Figure 4-1. *Magnetic resistance model*

The shielding factor, S, is defined as:

$$S = \frac{B_{ap}}{B_s} \tag{4.1}$$

Where B_{ap} is the applied B field and B_s is the magnetic field in the shielded region.

We begin by discussing a few design principles suggested by this intuitive model. First, the overall geometry of the shield should be such that there is a natural path for the flux lines to follow. A sphere would be the best shape for shielding all directions. However, this is usually impractical to manufacture. Typically a cylinder with end-caps is used. The shielding is best for fields that point in the radial direction because the cylinder can be constructed so that there are no gaps in the shielding as there necessarily are between endcaps and the shield body. The shielding in the axial direction depends on the shape of the end-caps and is typically smaller. Again, ideally they would be shaped as a hemisphere, but due to practical considerations they are usually conical.

The magnetic resistance model suggests that any gaps in the shield can severely limit the shielding factor. Even a very small air gap in the path of a flux line will result in a very high resistance (i.e., relatively low magnetic permeability) relative to the path along the shield. The effects of a gap are directly proportional to how wide the gap is. Similarly, the effects of a gap can be mitigated if there is overlap between the parts where there is a gap.

Another design feature relates to holes in the shielding. Some holes are necessary to allow the shields to be constructed around the glass cell, and further holes are necessary in order to pass in optical fibers, microwaves, magnetic coil current wires, and the signal lines from the photodiodes. The larger a hole is, the more it will degrade the shielding factor. Further, the degradation from a hole can be partially mitigated by adding tubulations to the openings such that the incoming flux is captured and guided into the shield.

4.1.2. Mu-metal

Our magnetic shields were manufactured by Amnuneal Manufacturing Corporation. Their mu-metal is a high permeability alloy made of ~80% nickel, ~15% iron, and most likely with small amounts of copper, chromium, and molybdenum. It can have a relative permeability as high as 80,000, making good for magnetic shields. A ferromagnetic material is composed of many small ferromagnetic domains that, in general, point in random directions. In a magnetic field the domains orient themselves to oppose the applied field. If the applied field is large enough, all of the domains align and the shields will saturate. Above the saturation field, a shield no longer reduces the size of the applied magnetic field.

The shields will not saturate as long as the externally applied field obeys the following relationship:

$$B_{ap} < \frac{B_{sat}\, T}{2R} \tag{4.2}$$

Where *T* is the thickness of the mu-metal and *R* is the radius of the shield. B_{sat} is the saturation magnetic field which is a constant that depends on the material. In our case, B_{sat} is 8000 G (Maltin and Koch, 2009). The best shielding is found when the fields are as far away from saturation as possible. For this reason, around our optics table, we have three sets of very large magnetic field coils (diameters ~3 m) that cancel out the earth's 300 mG bias magnetic field to a level of ~5 to10 mG at the center of the shields. These cancelation coils are left on continuously so that the earth's magnetic field does not saturate the shields (and so that the magnetic fields in adjacent labs do not change because of us).

The permeability of mu-metal can be degraded if the material is under mechanical stress. Stress-induced crystallization of the ferromagnetic domains inhibits

them from aligning with the applied magnetic field. If the metal is bent within the elastic limit, it will regain its full permeability when the stress is relieved. But if it is deformed beyond the elastic limit, i.e., when the deformation no longer obeys Hooke's law, the permeability can be permanently degraded. Thus when the mu-metal is shaped into a magnetic shield, it certainly is deformed in a non-reversible way and must be annealed at a high temperature (2100 °F) in a controlled hydrogen environment. After annealing, the permeability is restored to its full value, and care must be taken to ensure that no unnecessary stresses are put on the shields. This drives many of the design elements of the shields.

In the case of a real magnetic shield, with seams between multiple pieces and holes, the measured shielding factor is always less than what is expected when the ideal permeability is used for calculations. As an engineering rule, the real shielding expected from a shield with geometric imperfections can be calculated using an effective permeability of ~15,000 (Maltin and Koch, 2009). For design considerations, I will use a conservative relative permeability of 11,000.

4.1.3. Multi-level shield

The magnetic resistance model of shielding captures an intuitive description of magnetic shielding, but for specific design shapes, a more sophisticated theory is desirable. Sumner, Pendleburry, and Smith (1987) derive the shielding factor for an infinitely long, multi-layer cylindrical shield by solving Laplace's equation with the appropriate boundary conditions at each layer. This approximation is accurate provided that the length is greater than the radius of the shields. Their results for a shield with n layers are as follows:

$$S = 1 + \sum_{j=1}^{n} S_i + \sum_{j=1}^{n-1}\sum_{j>1}^{n} S_i\,S_j\left(1-\left(\frac{R_i}{Rj}\right)^2\right) + \sum_{i=1}^{n-2}\sum_{j>i}^{n-1}\sum_{k>j}^{n} S_i\,S_j\,S_k\left(1-\left(\frac{R_j}{R_k}\right)^2\right)\left(1-\left(\frac{R_i}{Rj}\right)^2\right) + \cdots + S_1S_2\ldots S_n\left(1-\left(\frac{R_1}{R_2}\right)^2\right)\ldots\left(1-\left(\frac{R_{n-1}}{R_n}\right)^2\right) \quad (4.3)$$

Where R_i is the radius of the ith layer, and S_i is given by:

$$S_i = \frac{\mu_i\,T_i}{2\,R_i} \quad (4.4)$$

Where μ, T and R are the relative permeability, thickness, and radii of the shielding layers respectively. In words, Equation (4.3) gives the sum of the contribution of each individual layer, and the double sum term has an element for each permutation of two shield layers, the triple sum term has an element for each permutation of three shield layers, etc. until the final term includes all n layers.

These equations show that adding additional shield layers is far superior to making one layer thicker, if the amount of material is kept the fixed. In particular, the shielding of one layer is linear with the permeability and thickness, but the shielding of a four layer shield scales roughly as the permeability and thickness each to the fourth power. Thus, multi-layered shields have a significant advantage over single shield layers.

It can also be seen with these equations that the larger the outer shield layer is, the better the shielding factor. Similarly, the smaller the inner-most layer, the better the shielding factor. However, as the inner-most shield layer gets too close to the atoms, another limitation appears. The shields are conductive and therefore produce a magnetic field through the Johnson noise (see Section 8.3.5), or through a residual magnetization of the magnetic shields. In our case, practical considerations led us to a shield with four layers.

4.1.4. Tapered spacing

The first step in the design of a multi-layer shield is to determine the spacing of the layers. The design of our magnetic shield has two constraints. In Figure 3-1, we see that the outer-most shield layer must fit within the space between the top and bottom 6-way crosses, i.e., its diameter must not be more than the length of the glass cell. Thus we fix the radius of the outer most layer at 17", which allows for ~2" of clearance to the glass cell's flange. A similar constraint on the inner-most layer is given by the plexiglass cylinder that will be described in Chapter 5. We would have a difficult time fitting in all the necessary optics for cooling and imaging if this plexiglass cylinder were significantly smaller. In order to allow clearance to the outer side of the cylinder which holds magnetic coil sets, the radius of the inner most shield layer is fixed at 8.5".

With these two radii fixed, the space of possible configurations for a four layer shield fills a two dimensional space where the dimensions are the radii of the second and third shielding layers, i.e., R_2 and R_3. In order to find the optimal radii, we calculate Equation (4.3) for all possible radii in this two dimensional space using a step size of 0.1". The results are shown in Figure 4-2.

The optimal shield radii can be extracted by taking the maximum shielding factor. For our constraints, the radii which give the maximal shielding factor are {8.5", 10.1", 12.8", 17"}. Note that the spacing between each layers is not constant, it is tapered such that the spacing between the inner layers is smaller and the largest spacing is between the two outer most layers.

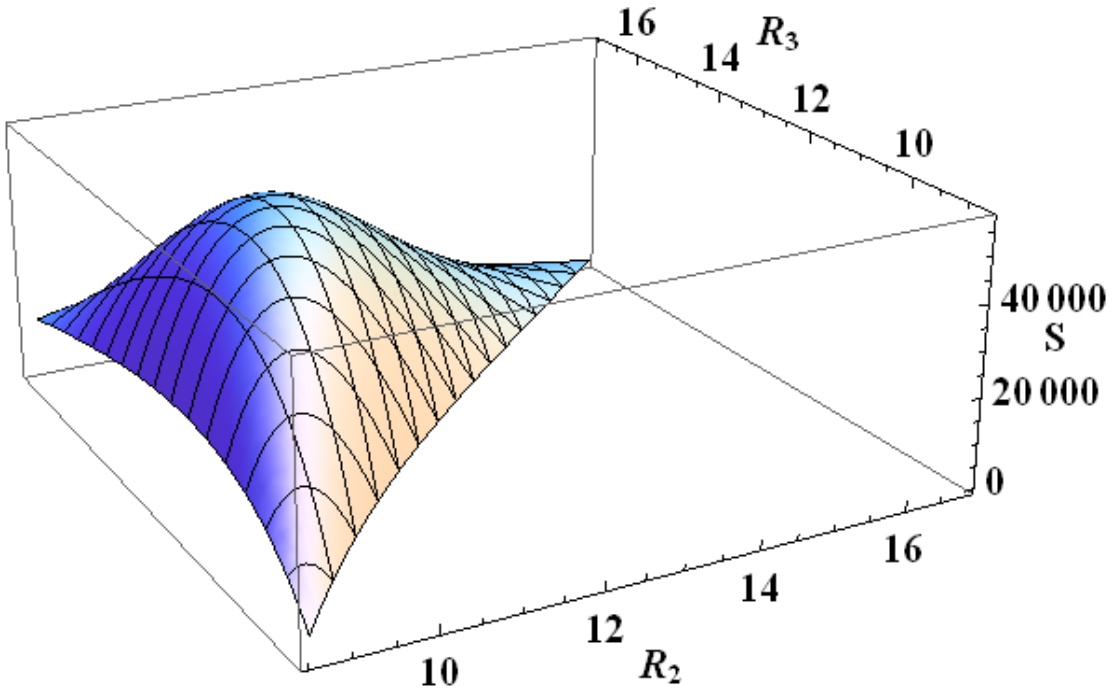

Figure 4-2. *Optimization of shield spacing*

Using the conservative effective permeability of 11,000, the calculated radii above, and a mu-metal thickness of 0.062”, the expected radial shielding factor is S = $5*10^4$. The mu-metal thickness was chosen as a trade-off between higher shielding factor and the cost and weight of the shield.

4.2. Practical considerations of shield construction

Although an infinitely long cylindrical shield is impractical, as long as the ratio of the length to the radius of the shield is > 1, the infinite length approximation is fairly accurate. For the end-cap design, a hemispherical shape is economically prohibited. A conical shape with a flat end is used as an approximation. The design of the end-cap shape is such that the conical section has a 45 degree angle.

The shield dimensions can be fully specified with the following definitions: *R* is the radius of the cylindrical portion, L_{cyl} is the length of the cylindrical portion, L_{end} is the length to the end of end-cap, and R_{end} is the radius of the end-cap flat section, as pictured in Figure 4-3. The dimensions of all shielding layers are summarized in Table 4-1. All distances are given in inches.

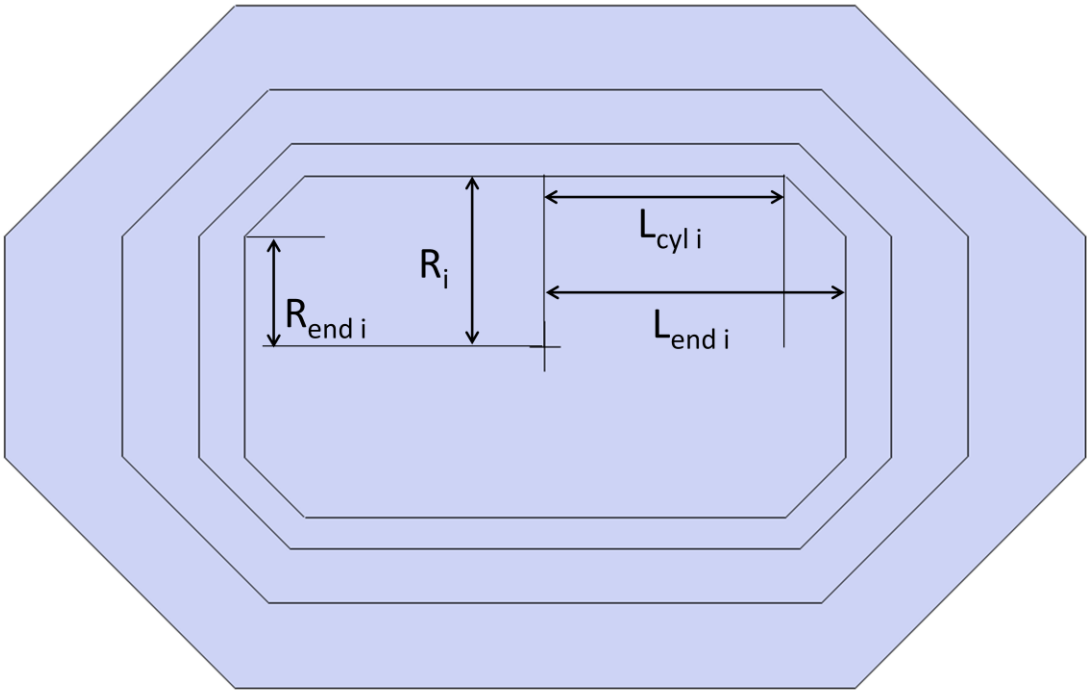

Figure 4-3. *Shield 2D schematic*

Shield layer	R_i	$L_{cyl\ i}$	$L_{end\ i}$	$R_{end\ i}$
1	8.5	12	15	5.5
2	10.1	12.7	17.3	5.5
3	12.8	13.8	21.1	5.5
4	17	15.5	27	5.5

Table 4-1. *Summary of shield dimensions*

4.2.1. Tubulations

Some clearance holes will always be necessary in a shield. The magnetic flux lines can leak in through such holes. The two factors that determine how much magnetic field leaks in are the size of the hole and its distance to the place of interest. As Khriplovich and Lamoreaux (1997) describe, the magnetic field from a hole falls off exponentially as:

$$B = B_{ap} e^{-1.5\frac{h}{r}} \tag{4.5}$$

Where B_{ap} is the externally applied field, *h* is the distance to the hole, and *r* is the radius of the hole. The factor of 1.5 is a numerical geometric factor. Using Equation (4.5) one could roughly estimate the expected field that bleeds in for our holes:

$$\frac{B}{\mathrm{B_{ap}}} = \sum_{holes} \prod_{layers} e^{-1.5\frac{h_i}{r_i}} \sim 10^{-6} \tag{4.6}$$

This is a sum of the four holes in each direction. The product is taken so that the distances h_i, are the distances between subsequent shield layers, until the inner-most shield layer which is the distance to the center of the shield. The holes on the top and bottom are 1.75” diameter, and the holes on the end-caps are 1.5” diameter. Almost the entire residual field comes from the holes for the glass cell. This shows that without tubulations, the shielding could be compromised near the 10^6 level, however this is a rough estimate. The effect from a hole will primarily be a magnetic field along the direction from the hole to the atoms. The overall geometry of the shield ensures that there are no holes along the direction of the field that we care the most about, i.e., the z direction.

In order to partially mitigate the effects of the hole, tubulations can be added to the holes so that the incoming magnetic flux is captured and directed into the shield

(Burt and Ekstrom, 2002). A cut-away cross section of a tubulation on the end-caps is shown in Figure 4-4.

For a single shield layer, the longer the tubulation the better. However, for a multi-layer shield, when the length of the tubulation becomes too long, the flux that is concentrated into the outer shield has a low resistance path to jump into the next inner layer. This can reduce the shielding factor.

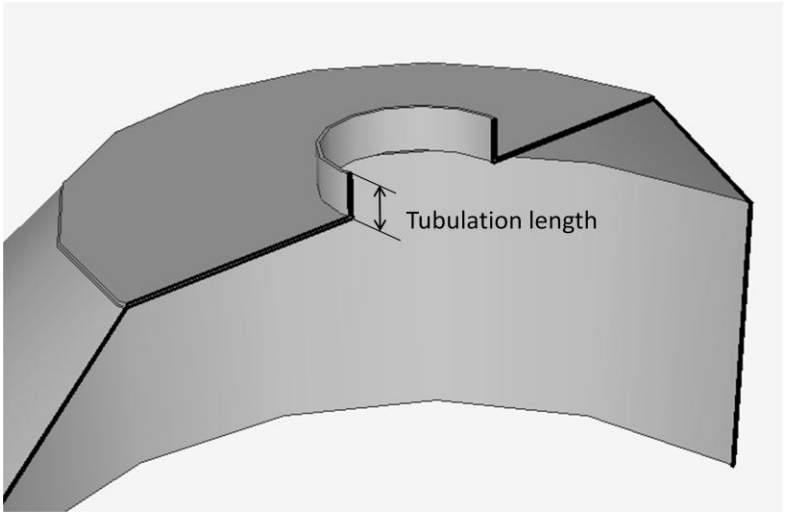

Figure 4-4. *Tubulations*

To determine the optimal tubulation length, commercial finite element software (COMSOL Multiphysics) was used to model a static magnetic field with tubulations of different lengths on a multi-layered shield. The simulations used the cylindrically symmetric case. The length of the tubulation is scaled to the distance to the next shielding layer. The real hole sizes and distances between our shields were used. The results of the cylindrically symmetric case, i.e., the end-cap holes, were assumed to be an approximation to the non-cylindrically symmetric case of the tubulations on the mid-piece holes.

The results are shown in Figure 4-5. The optimal length appears to be when the length of the tubulation is about 30% of the distance to the next shield layer. This result was used on all tubulations in our shield design. Each shield layer has four holes, one on the top and bottom to allow the passage of the glass cell, and one on either end-cap to allow passage of various cables. The tubulations can increase the shielding by about 30% as compared to the case with no tubulation.

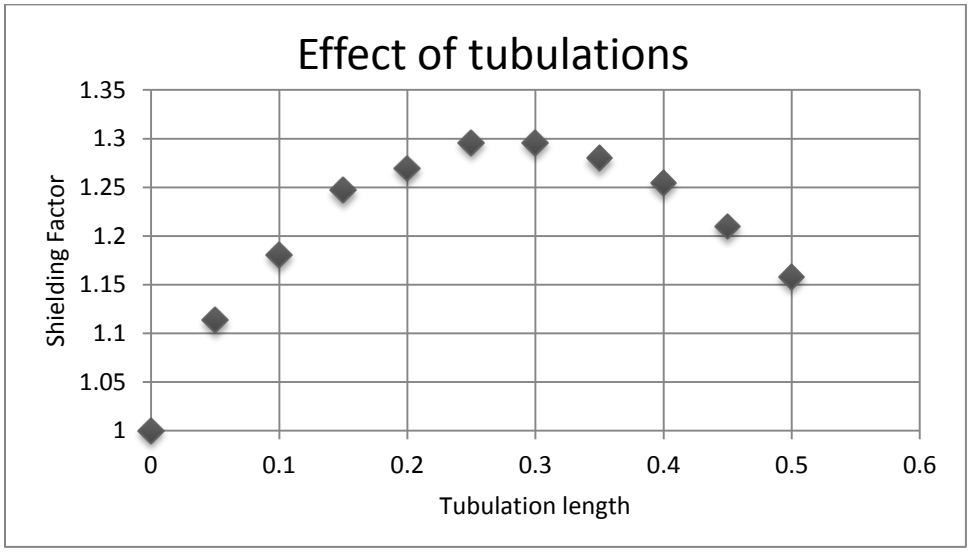

Figure 4-5. *Effect of tubulations*

The shielding factor is scaled to the case of a hole with no tubulation. The tubulation length is given as a fraction of the distance to the next shielding layer.

4.2.2. Three piece construction

Due to the nature of our setup, we must first install the glass cell onto the vacuum system, and then construct the magnetic shield around the glass cell. This, along with the desire to keep the shield pieces from being unmanageably heavy, led us to a design with three sections for each layer as can be seen Figure 4-6.

The plexiglass cylinder (a) is shown already installed around the glass cell (b). The central portion of the shield (c) has clearance slots on the top and the bottom so that it can be installed around the glass cell. A small piece was manufactured to cover up the majority of this slit once the shields are constructed. In order to mount the shields with as little stress as possible, sets of large aluminum rings (d) were glued around each shield layer with ~1/8” to 1/4” of Loctite Superflex RTV Silicone Sealant. This provided enough mechanical stability of the rings, as well as providing a layer of rubber that can absorb stress and vibrations. All tight connections, which might introduce stress, are then made directly to the aluminum rings rather than to the mu-metal shield. The rings were cut out of 3/8” and 1/4” thick aluminum for the end-cap rings and center piece rings, respectively. Bethlehem Aluminum cut the rings directly and some details were machined onto them in house for the mounting.

The shields are supported underneath by a structure built up from the table using 1.5” diameter steel posts. A rail system built of from Thorlabs 66 mm line forms the structure above the posts. On these, several aluminum blocks hold 0.75” diameter titanium support rods (e) at a 30 degree angle. The ends of these rods are attached to the plexiglass cylinder with titanium screws. Further, a set of aluminum clamps (f) are attached to the titanium rods using a compression lock. The aluminum clamps for the center piece hold an aluminum cross bar which runs through holes on the bottom of the aluminum rings. These bear the weight of the center shield pieces.

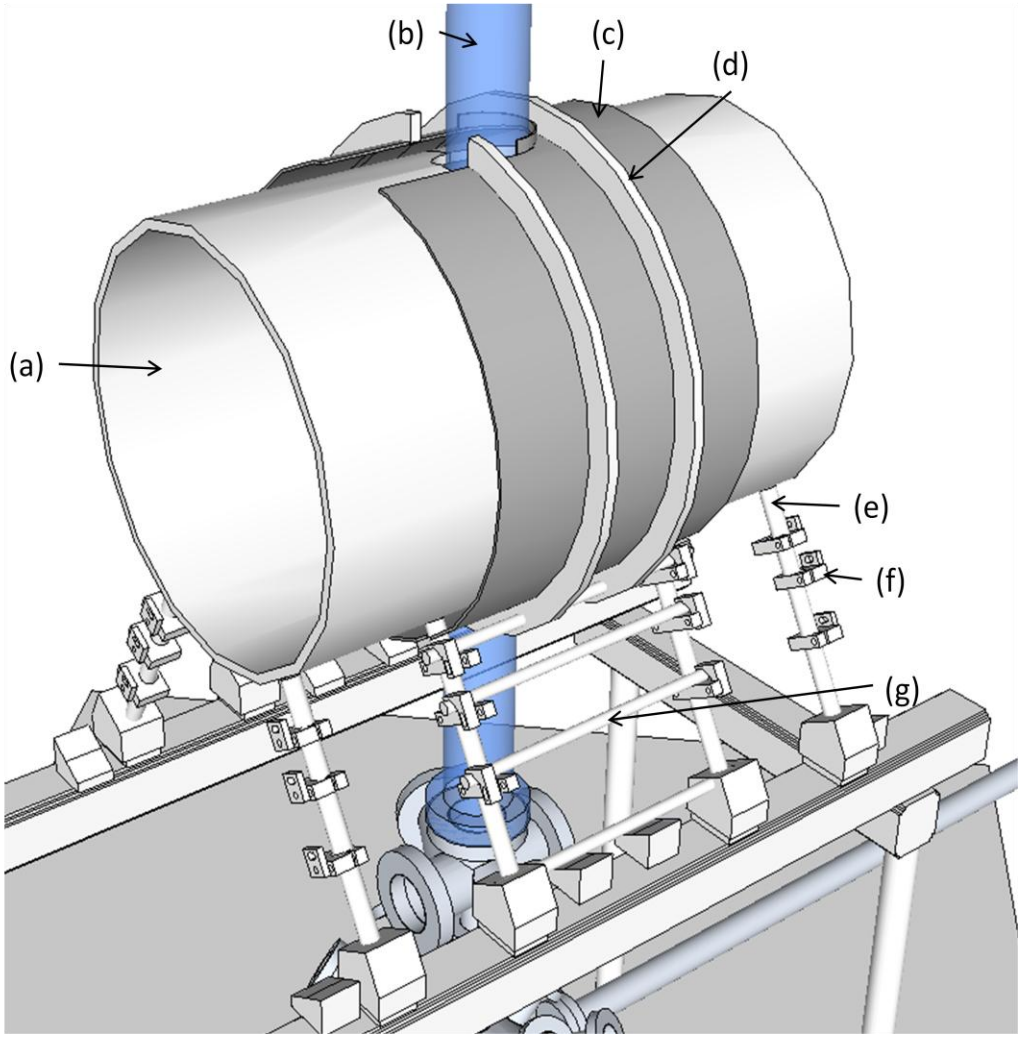

Figure 4-6. *Shield construction*

a) Plexiglass cylinder, b) glass cell, c) mid-piece of shield, d) aluminum ring, e) titanium support rods, f) aluminum clamps, g) aluminum cross bars.

Figure 4-7 shows more details for the end-cap mounting. The end-cap (a) can be slid into place so that the weight is supported where the aluminum ring rests directly on the aluminum clamps (b). The rings are then screwed onto the clamps for stability. A clearance slot (c) allows the end-cap to be mounted even though the titanium support rods are already installed. The central pieces also have a small slot so that the central support rods can fit into them snugly.

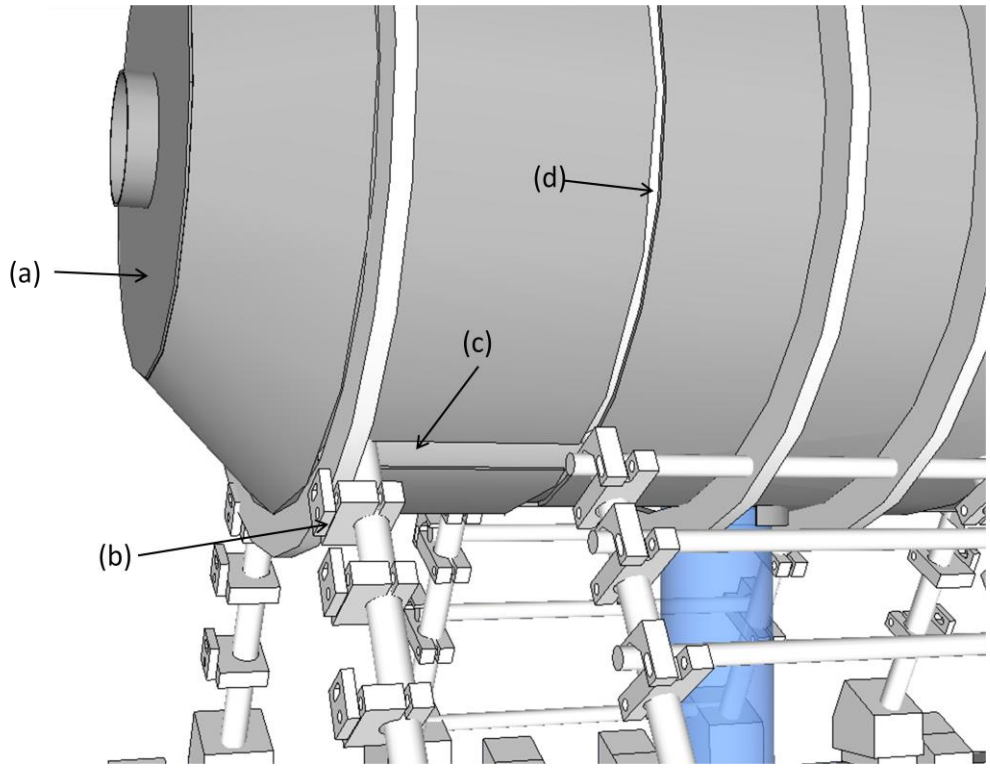

Figure 4-7. *Further shield details*

a) end-cap, b) aluminum clamp, c) clearance slot for titanium rods, d) mid-piece to end-cap seam.

When finished, there is a seam (d) between the mid-piece and the end-piece. If we recall the discussion from Section 4.1.1 these types of gaps can create problems for the shielding factor. Typical shield designs will have an end-cap that has a 'joiner band' which is slightly larger than the mid-piece so that it can close fit over the mid-piece. Then the joiner band is screwed into the mid piece at several points around the radius. Because we must install our magnetic shields in-situ around the delicate glass cell, we favored a mounting procedure that did not require us to balance heavy shield pieces over our table while we made close fitting connections. Second, the bolting of the joiner band onto the mid-piece introduces additional stress to the shield layers, which should be avoided if possible. Our solution to this problem is described in the next section.

4.2.3. Belts

Our shield design includes the use of ‘belts’ that can be wrapped around the seam between the mid-pieces and the end-caps. The belts have a slit on one side so that they can sit loosely around the mid-piece while the end-caps are brought into place. After the end-caps are secured in place, the belts are cinched tightly with a 1.5” wide nylon strap. The clearance slots on the bottom allow the belts to slide over the titanium mounting rods. An example of a belt is shown in Figure 4-8. In order to cover the hole from the slit, each seam was covered by two belts with the opposite handedness. Each shield layer had four belts, two for each seam. The belts have a width of 9” and are made of 0.04” thick mu-metal.

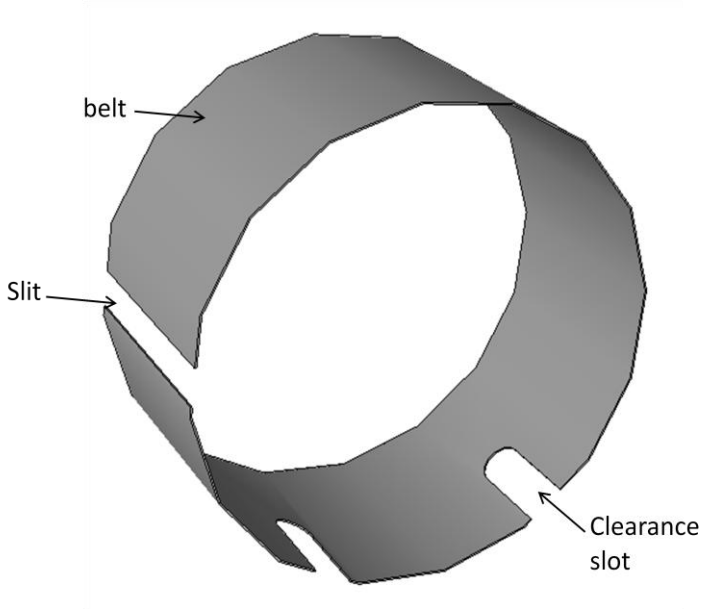

Figure 4-8. *Magnetic shield belts*

The belts were made as long as possible while still being consistent with the base mounting structure. This gave them maximal overlap with the endcap and midpieces in order to minimize the effects of the gap between them.

4.2.4. Shims

Due to the large size of the shields and the uncertainty of the annealing process, neither the end-caps nor the mid-pieces were perfectly round. This resulted in gaps of various sizes between the belts and either the end-caps or the mid-pieces. These gaps were about ~1/4” at their widest, and were distributed more or less randomly around the shields. In order to fill in this gap, we had a collection of thin mu-metal shims made. The shims were 0.75” wide, 0.02”, and 0.004” thick, and of various lengths. During and after the mounting procedure, the shims were used to fill in as much of the space between the belts and the end-caps and mid-pieces as possible.

4.2.5. Mounting procedure

There is one practical aspect of the shield mounting that has not yet been discussed. In order to do the mounting, one must first mount all four mid-pieces while supporting them from only one side, with a structure that is separate from the final mounting structure. If the four central titanium support rods are put in place for the inner-most shielding layer, the next layer could not be installed because it would run into the legs. For this purpose a ‘temporary tower’ was constructed that used a collection of steel beams on which the shields could be cantilevered temporarily until the fourth layer was in place. When the outer-most mid-piece is in place, the 4 titanium support rods can be

installed and the mid-pieces can be securely attached to them. This sequence is depicted in Figure 4-9.

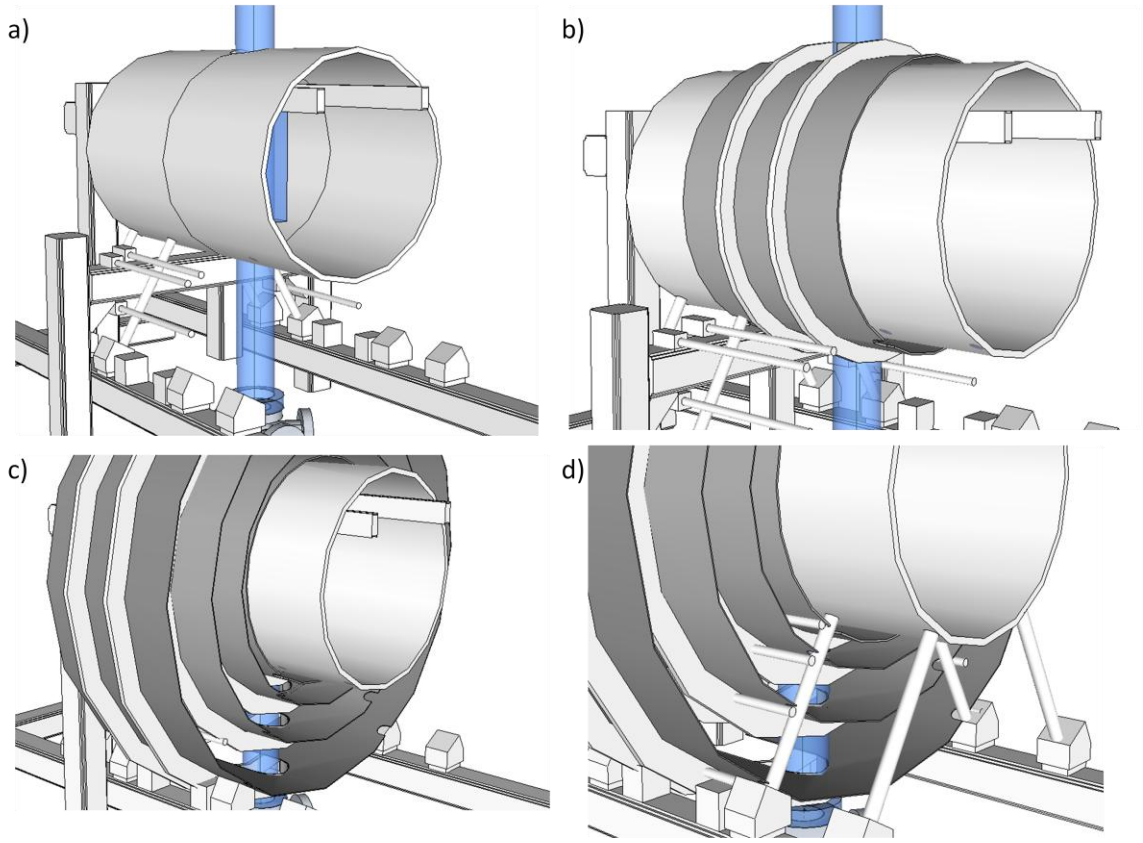

Figure 4-9. *Temporary mounting tower*

a) the temporary tower with steel cantilevers is constructed on one side of the shield. There is also a support for the plexiglass cylinder, b) the inner-most layer can be brought in, and the weight of the shield rests on the cantilevers through the aluminum ring, c) each layer can successively be brought in and rested on the cantilevers, d) with the outer-most layer in place, the other side of the titanium legs can be brought into place and they can be secured.

With the mid-pieces on but without the end-caps, access to the optics of the measurement region is unhindered. At this point, the cooling and trapping beams for the measurement chamber, the imaging systems, and the state preparation devices can be setup with the shields partially installed. This is necessary because during the first stage of the shield mounting procedure it is possible that some optics may be bumped or

misaligned. The access to the optics in the measurement chamber with partially installed shields can be seen in Figure 4-10.

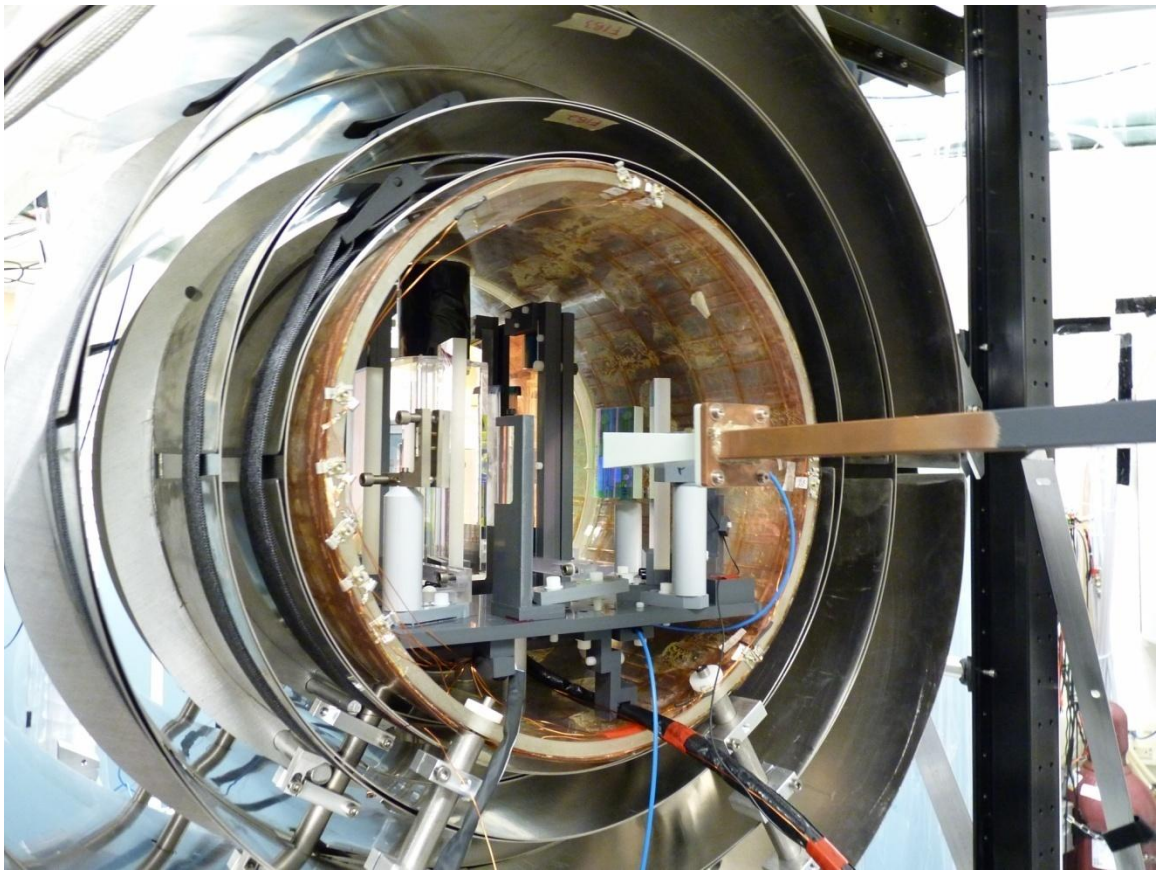

Figure 4-10. *Measurement chamber optics in partially installed shield*

Once the experiment is realigned and optimized, the end-caps can be installed. The clearance slots on the end-caps are slid over the outer set of titanium legs and their aluminum clamps are secured. Working from the inner-most layer out, the shims are placed into the gaps between the belts and the shield layers, and the nylon strap is cinched tightly around the belt. In addition, the top of the aluminum ring on the end-cap is tied to the ring on the center piece to prevent the end-cap from tilting. This is repeated until all four end-caps are in place.

Altogether, the four-layer shield is comprised of 32 separate mu-metal pieces. With the aluminum rings, the shield weighs around 350 lbs. The shield is mounted ~1 m above the optical table around the glass cell. The clearance from the shield to the cell is ~0.5”. The shield mounting is completely independent from all other mounting including that for the vacuum chamber and the tower which holds the optics above the vacuum chamber. A cross-section of the complete shields is shown in Figure 4-11, and a picture of the installed magnetic shields is shown in Figure 4-12.

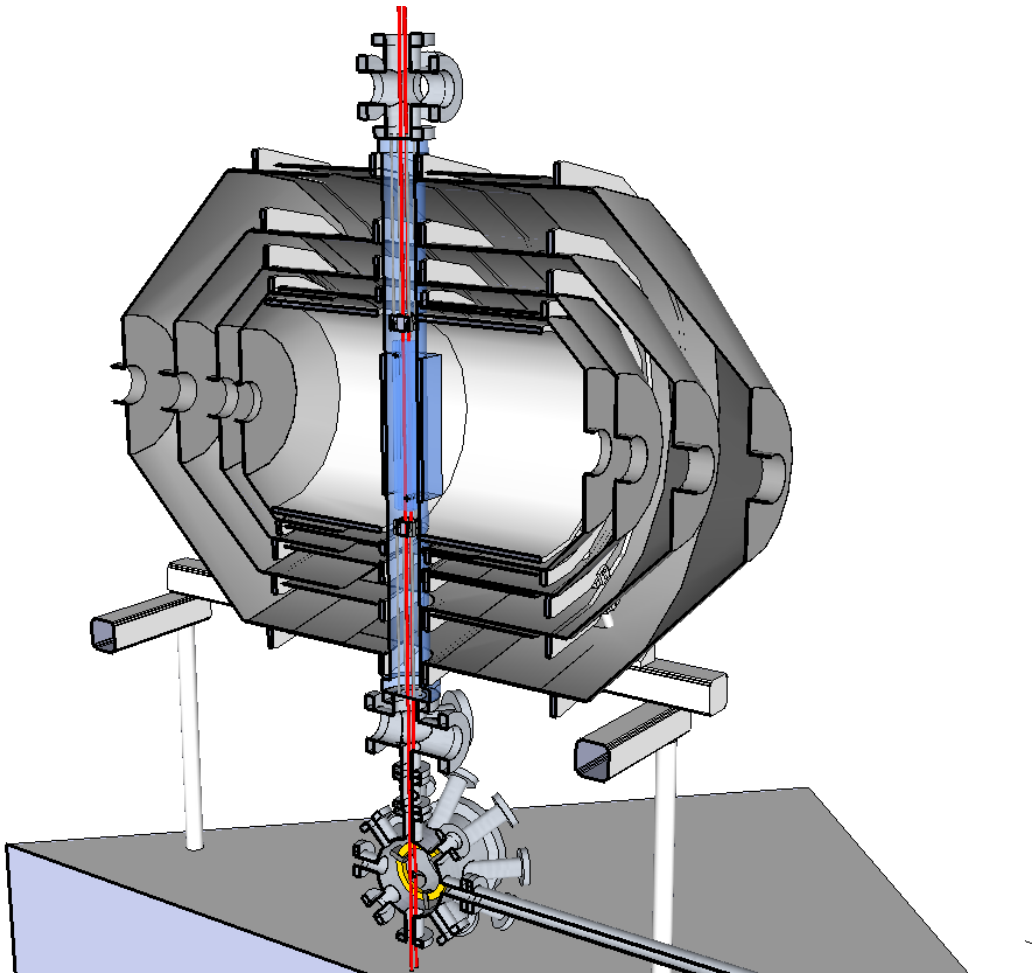

Figure 4-11. *Cross section of full magnetic shield*

Figure 4-12. *Picture of magnetic shields on table*

4.3. Operation

4.3.1. Degaussing

In order to obtain the optimal shielding performance, one must first ensure that the directions of the small ferromagnetic domains are effectively randomized. This is accomplished with a procedure called degaussing. To degauss a shield, first an oscillating magnetic field must be applied that is large enough to completely saturate the shields. Then the amplitude of the field is slowly ramped down to zero so that the domains end the process pointing in random directions.

The geometry of the degaussing coils is shown in Figure 4-13. The cylinder represents all four shield layers. The degaussing coils are wrapped through the shield so that when a current *I*(*t*) is applied, it produces a field, *B*(*t*), that circulates around the shields as shown in the figure.

The applied current is of the form:

$$I(t) = I_d n\, Sin(vt)(1 - rt) \tag{4.7}$$

Where I_d is the peak amplitude of the current (20 A), *n* is the number of turns in the degaussing coils (23), *v* is the frequency of the alternating current (5 Hz), and the term in parentheses is a linear ramp where *r* is chosen such that *I*(*t*) goes to zero after 2000 or 3000 cycles of the alternating current (400-600 seconds).

A low frequency (1 Hz) high pass filter is used to ensure that there is no small DC bias offset on the current in Equation (4.7), which could lead to residual magnetization of the shields. When the linear ramp is over, i.e., *I*(*t*) = 0, the current is shut off permanently. The electronics for the degaussing coils will be described in Zhu (*forthcoming*).

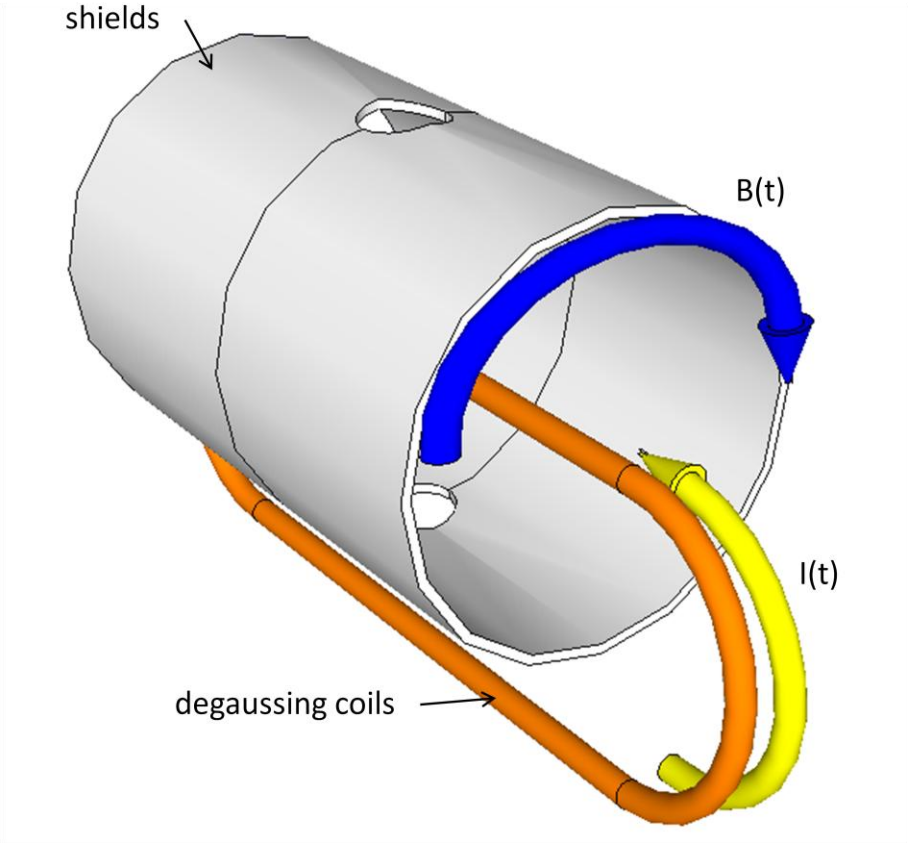

Figure 4-13. *Degaussing coils*

In this diagram, the orange loop represents the path taken by the loops of the degaussing coil, the yellow and blue arrows represent that when the current is applied in the direction indicated by the yellow arrow, the magnetic field follows the magnetic shields in the direction indicated by the blue arrow.

During degaussing, a pick-up coil, which is wrapped in the same way as the degaussing coils, can be used to monitor the field induced in the shields. By watching the voltage induced on this pick-up coil, one can verify that the shields do in fact saturate under the applied magnetic field.

4.3.2. Results

The shields were tested by placing a magnetometer inside the shield, applying a calibrated magnetic field from the outside, and measuring the field at the magnetometer. The shields were mounted in a separate room and tested. In several ways this test was less than ideal, because the separate room did not contain cancelation coils for the earth's magnetic field, and at the time of the test, the shims were not used on the shields. However, there is no safe way to insert a magnetometer into the shields when they are installed on the system without risking bumping optics or other devices inside the shield, and the magnetometry with the atoms is still currently in progress, so these tests will have to suffice for now.

The shielding factor along the z direction was measured to be $> 5*10^4$. No externally applied magnetic field was measurable inside the shields with the magnetometer we had, with a sensitivity of 3 μG. We did not upgrade our magnetometer or our ability to apply a larger field to measure the shielding factor more accurately because of the fact that the measurement was not ideal for the reasons already mentioned.

The axial shielding factor was measurable and was found to be $1.3*10^4$. This is a factor of 2 or 3 worse than what is expected for the axial shielding factor, and this measurement was the impetus for using the shims.

Chapter 5. Magnetic coil set

In order to optically pump the atoms, to provide a small bias B field for the measurement procedure, and to cancel out residual fields and field gradients, we need to have the ability to produce magnetic fields inside the magnetic shield. These coils need to produce a uniform field over the entire volume of trapped atoms which could stretch up to 10 cm in the vertical direction. They also need to have a small profile so that they can fit between the plexiglass cylinder and the inner-most magnetic shield layer and must be made of non-magnetic materials.

Individual coils for uniform bias magnetic fields in each direction will be used for control over the quantization axis for microwave transfers. In order to cancel out any spatially varying fields, we also wish to have an individual handle on all first order derivative fields. Maxwell's equations limit the number of independent first order derivatives that are allowed in free space.

Using the following definitions we can define all first order derivatives:

$$G_{ab} = \frac{\partial B_a}{\partial b} \tag{5.1}$$

The entire set is given by:

$$G_{ab} = \begin{pmatrix} G_{xx} & G_{xy} & G_{xz} \\ G_{yx} & G_{yy} & G_{yz} \\ G_{zx} & G_{zy} & G_{zz} \end{pmatrix} \tag{5.2}$$

If we consider the two Maxwell's equations:

$$\nabla \cdot \boldsymbol{B} = 0$$

$$\nabla \times \boldsymbol{B} = 0 \tag{5.3}$$

It can be easily shown that $G_{ab} = G_{ba}$ and that only two of the G_{aa} are independent. This results in there being only five independent first order gradient fields. We use the following set: G_{xx}, G_{zz}, G_{xy}, G_{xz}, and G_{zy} plus the three bias fields which we will label G_x,

G_y, and G_z. Thus a total of eight coils are needed in order to have an independent handle on all bias magnetic fields and all first order derivative fields.

5.1. Ideal sheet currents

The design of the coils that would give these fields bears some consideration. The geometry of our experiment limits the possible coil shapes to fit on a cylinder with its axis along the x direction, i.e., they must be constructed on the plexiglass cylinder that holds the measurement chamber optics. Second, their shape must be optimized for operation inside a magnetic shield. The image currents induced in the high permeable shield can change the shape of the magnetic field produced, so in order to achieve as uniform a field as possible, the shields must explicitly be considered in the design.

To design the coils one could try to adopt the philosophy of Helmholtz coils and successively place individual coils in positions to cancel out the higher derivatives of field. That is, in order to have uniform fields, one wishes the higher derivatives of the field to be equal to zero. There have been some calculations for specific field shapes (Hosoya and Goto, 1991), but it is not obvious how this strategy can be generalized to all of the coil shapes we require.

A second approach based on the work of Suits and Wilken (1989) defines boundary conditions at the magnetic shield and then calculates the ideal sheet currents flowing on the cylindrical geometry that produce the desired field. Unfortunately, it is not possible to actually construct sheet currents, so once the sheet currents are derived, line currents can be found from them. We use the cylindrical coordinate system shown in Figure 5-1 along with the lab coordinate system.

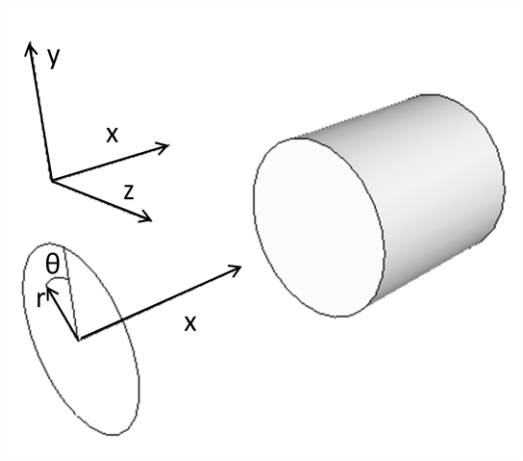

Figure 5-1. *Cylindrical coordinate system*

In this coordinate system we have the standard cylindrical coordinate system transformations. It is obvious from the geometry that some of the designs can be can be obtained by a simple π/2 rotation about the x axis. That is we can get G_y from a π/2 rotation of G_z and G_{xy} from a π/2 rotation of G_{xz}. And as will be made clearer below, G_{zy} can be obtained by a π/4 rotation about the x-axis of the G_{zz} coils. This reduces the total number of field coils we must design to five.

The boundary conditions for a magnetic field, ***H***, near a surface can be found in Jackson (1962) for example. They are:

$$\boldsymbol{n} \cdot (\mu_1 \boldsymbol{H_1} - \mu_2 \boldsymbol{H_2}) = 0$$

$$\boldsymbol{n} \times (\boldsymbol{H_1} - \boldsymbol{H_2}) = \boldsymbol{K} \tag{5.1}$$

Where ***n*** is the vector defining the surface, and ***K*** is the surface current. Call region 2 the shield, and region 1 the air inside the cylinder in the region we care about. We take the limit where $\mu_1/\mu_2 \to 0$ because the mu-metal has a relative permeability of 80,000. Also, because the region we care about, region 1, has $\mu_1 = \mu_0$ we have ***H*** = ***B***, and the condition becomes:

$$\boldsymbol{n} \times \boldsymbol{B} = \boldsymbol{K} \tag{5.5}$$

Each coil will have its own B field, which we will define as a Cartesian vector in the form {i, j, k}. These vectors are summarized in Table 5-1.

Coil	**B** (cart.)	**K = n**X**B** (cart.)	**K = n**X**B** (cyl.)
G_x	{1,0,0}	{0 , -Sin(θ) , Cos(θ)}	{0 , 1 , 0}
G_z	{0,0,1}	{-Cos(θ) , 0 , 0}	{0 , 0 , -Cos(θ)}
G_{xx}	{x,-y/2,-z/2}	{0 , -x Sin(θ) , x Cos(θ)}	{0 , x , 0 }
G_{zz}	{0,-y,z}	{-2 Cos(θ) Sin(θ) , 0 , 0}	{0 , 0 , -Sin(2θ)}
G_{xz}	{z,0,x}	{-x Cos(θ) , -Sin(θ)^2, Cos(θ) Sin(θ)}	{0 , Sin(θ) , -x Cos(θ)}

Table 5-1. *Summary of magnetic field coil design*

For the bias fields we require a vector field that is constant in one direction. Hence these fields are simply proportional to a constant vector in one direction. It is easily verified that all derivatives of the magnetic fields (**B**) for G_x and G_z in Table 5-1 are equal to zero.

The Maxwell's equation that reads $G_{xx}+ G_{yy}+ G_{zz} = 0$, implies that in order to consistently define a field for G_{xx} we must also have components in the y and z direction. To minimize the electromagnetic field energy we set the z and y components equal to each other (Suits and Wilken, 1989). Again, it is easily verified that this field has no bias field in the center of the cylinder, (i.e., x = y = z = 0), and has a linear derivative in the x direction.

The G_{zz} coil is defined with a similar condition, but it also imposes translational symmetry along the x direction as is natural for the cylindrical geometry. Finally, the G_{xz} similarly satisfies Maxwell's equations and produces a field with the appropriate characteristics. For the G_{zy} coil, note that if you apply a π/4 rotation about x on the G_{zz} coil, you get the vector {0 , y+z , y-z}. It can be easily verified that this field has satisfies

the requirements for G_{zy}. So we will just simply rotate the design of the G_{zz} for the G_{zy} coil.

To solve the boundary value equation, Equation (5.5), we must first note that the vector that defines the surface is given by:

$$\boldsymbol{n} = \boldsymbol{r} = -Cos(\theta)\boldsymbol{j} - Sin(\theta)\boldsymbol{k} \tag{5.6}$$

The surface current is then simply given by the cross product in Equation (5.5). These are summarized in Table 5-1 in Cartesian form as well as being converted into cylindrical coordinates {r,θ,x}. These currents are drawn in the x-θ plane in Figure 5-2 where the vector field shows the current directions and the false color shows the current magnitude.

It can be seen that the G_x coil is simply a solenoid, and the G_{xx} is an anti-solenoid coil. G_z is the familiar 'cosine θ coil' distribution. In this terminology, the G_{zz} coil could be called a 'sine 2θ coil.'

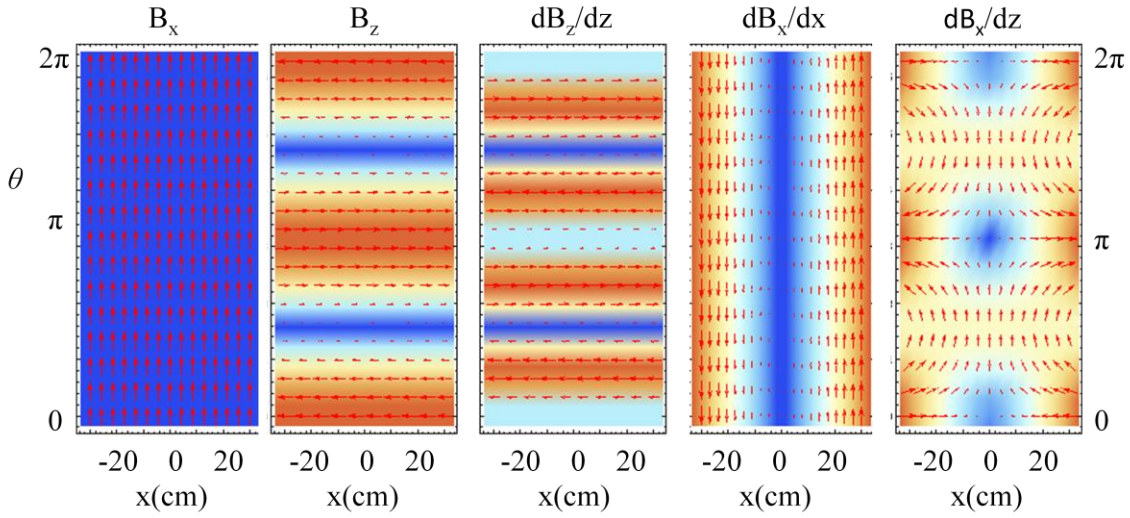

Figure 5-2. *Drawing of sheet currents in xθ plane*

5.2. Line current approximations

To determine the lines of current which approximate the shapes of Figure 5-2, we need to draw lines in the direction of the current that have a density proportional to the magnitude of the current. In other words, we need to find the fields lines of the 2-dimensional vector fields in the fourth column of Table 5-1. Note that the divergences of these fields are 0, ensuring that there is no source, and that these currents can be created by real distributions.

The field lines of a 2-dimensional vector field in the x-θ plane satisfy the differential equation:

$$\frac{\partial x}{\partial \theta} = \frac{K_x}{K_\theta} \tag{5.7}$$

The field lines for G_x, G_z, G_{xx}, and G_{zz} are trivial because they are only in one direction. The field lines for G_x and G_{xx} are of the form $x = a_i$, where the a_i are constants. Similarly G_z and G_{zz} have field lines of the form $\theta = a_i$. The field lines for the remaining G_{xz} coil are somewhat less trivial, but can be solved to be $x = a_i/\mathrm{Sin}(\theta)$.

Now all we need to do is determine the a_i for each coil set so that the density of current lines is proportional to the magnitude of the sheet currents. For the four coil sets with currents in only one direction, this is straightforward. For the G_{xz} it can become straightforward once you realize that the magnitude of the field:

$$|\boldsymbol{K}_{xz}| = \sqrt{Sin(\theta)^2 + x^2\, Cos(\theta)^2} \tag{5.8}$$

is constant for $x = \pm 1$ and $\theta = 3\pi/2$. Then one needs to find a set of a_i that gives constant spacing along these lines. As it happens, this is true for equally spaced a_i. In Figure 5-3. *Line current approximations to the ideal sheet currents* we plot the results of the properly spaced field lines for all eight coil sets.

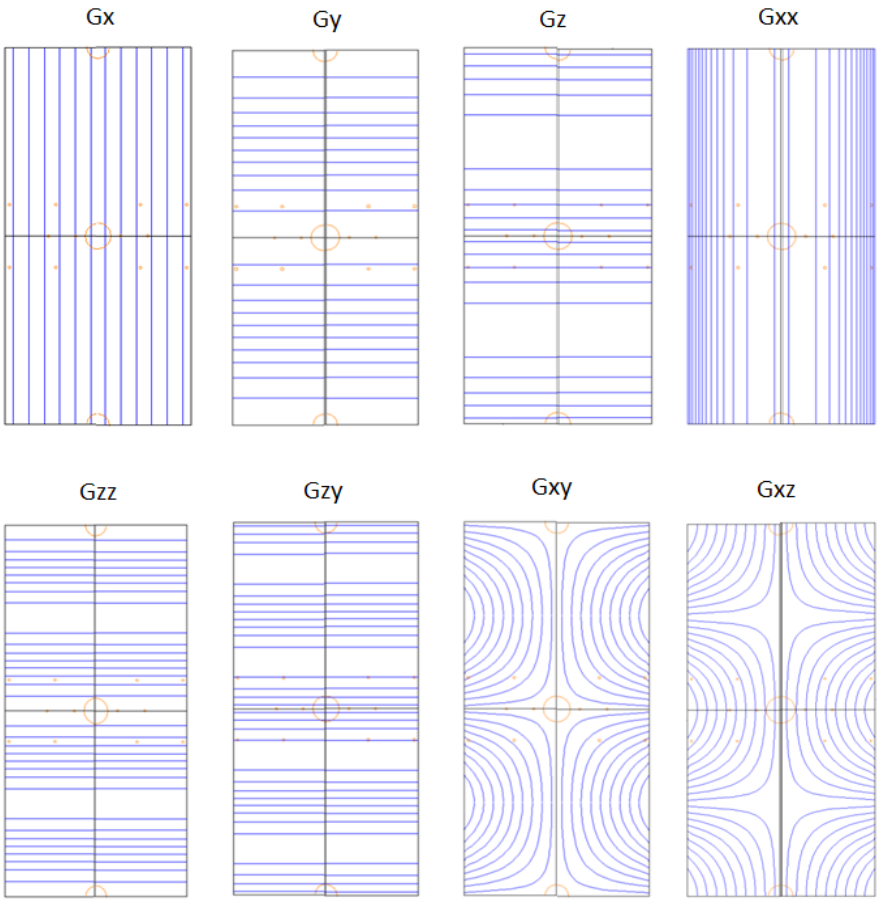

Figure 5-3. *Line current approximations to the ideal sheet currents*

5.3. Construction

The eight coil sets were constructed out of 50 μm thick 2.5 mm wide copper foil. Pure copper was used to ensure that the coils are non-magnetic. The thin foil was used so that all eight coils could be constructed on a relatively thin layer on the outer surface of the 8” diameter plexiglass cylinder and still fit within the 8.5” diameter inner layer of the magnetic shield.

In order to assemble the cylinder around the glass cell, it must be built in two pieces, and then put together around the cell. This means that any coil sets that have a

component of the current that runs along the cylinder in the x direction must make connections between the two cylinder halves in-situ after they are installed around the glass cell. Also, the coils must allow for the magnetic shield mount legs to pass through them to the cylinder, as well as the clearance hole for the glass cell.

The shapes in Figure 5-3 were drawn and printed to scale on large templates. Holes for the glass cell and magnetic shield mounting legs were drawn where they would be when the templates were wrapped around the cylinder. Then, a large piece of transparent 125 μm polyester film was secured over each template and the coil was manually laid out on the polyester and secured with superglue. The coils were guided around the clearance holes, and leads were added to the edge of the cylinder. To simplify construction, two coil layers were put on each template, and were kept isolated with 25 μm thick Kapton foil. When all was done, the total amount of copper foil used was approximately 190 m long and about eight bottles of superglue were used. This construction should be done in a well ventilated place.

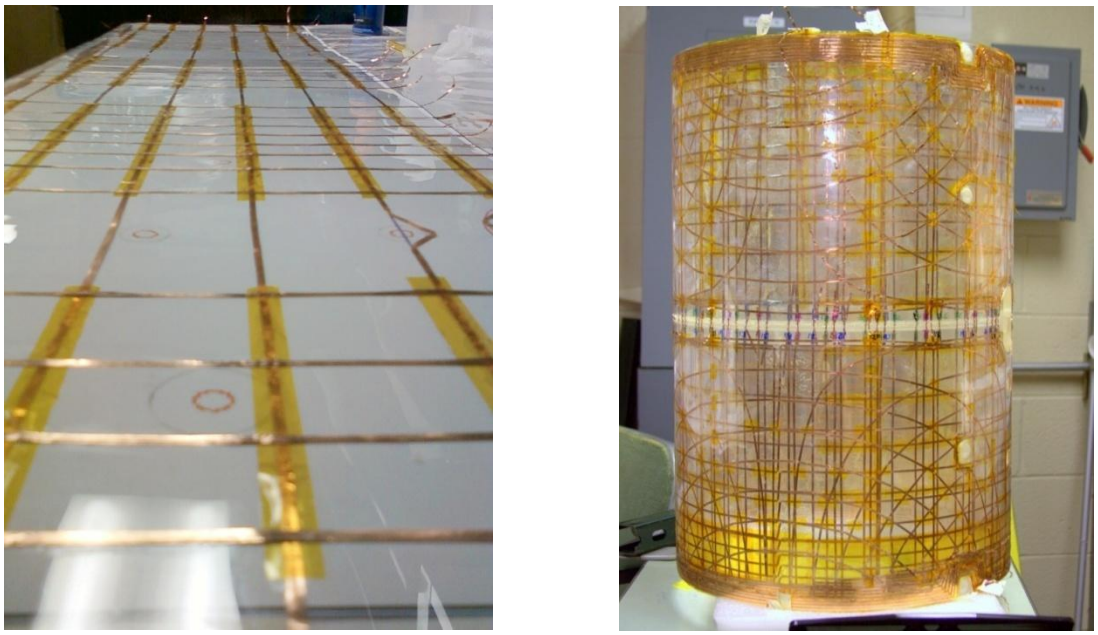

Figure 5-4. *Magnetic coil construction and completed set*

After the polyester sheets were completed, each layer was successively glued (Elmer's Ultimate Glue) in place around the plexiglass cylinder. For those coil sets that have currents that must flow continuously around the θ direction, a silver epoxy (Epoxy Technology E4110) was used as a 'heat-less' solder to complete the circle around θ. See Figure 5-4 to see the magnetic coils during construction and the complete set.

There are a total of 104 in-situ connections that must be made between the cylinder halves. Ultimately, these connections were soldered in-situ. This is not ideal because we would prefer the connections to be easily reversible. But this was a solution in response to the fact that our potential solution was unsuccessful.

That potential solution to this is sketched in Figure 5-5. The copper foil leads (a) are wedged into a small slot on a nylon clamping piece (b). Then a thick, short copper wire lead (c) is pressed into the nylon clamp. The press fit of the copper wire into the nylon clamp sure ensure that the wire presses onto the copper foil giving a solid electrical connection. The nylon clamps are separated by 2 mm giving the ability to do many connections in a very small distance. Though this idea worked well in the proto-type stage, when constructed on the actual system, the connections unfortunately had a small but untenably large failure rate. The fix was to solder the small copper lead to the copper foil leads on either side. These solder joints are less than ideal because they must be irreversibly broken when the system is taken apart and the hot soldering iron near the nylon clamps and polyester sheets tended to cause a slight amount of melting. In the end, the soldering was able to make all the connections. Unfortunately, after being installed for some time, and after the inner magnetic shield layers were installed (making access to the in-situ connections impossible) one of the connections on the G_{zy} failed and this coil developed an infinite resistance. These in-situ connections should be re-

thought and re-done in a subsequent stage of the experiment, i.e. when the magnetic shields are taken off.

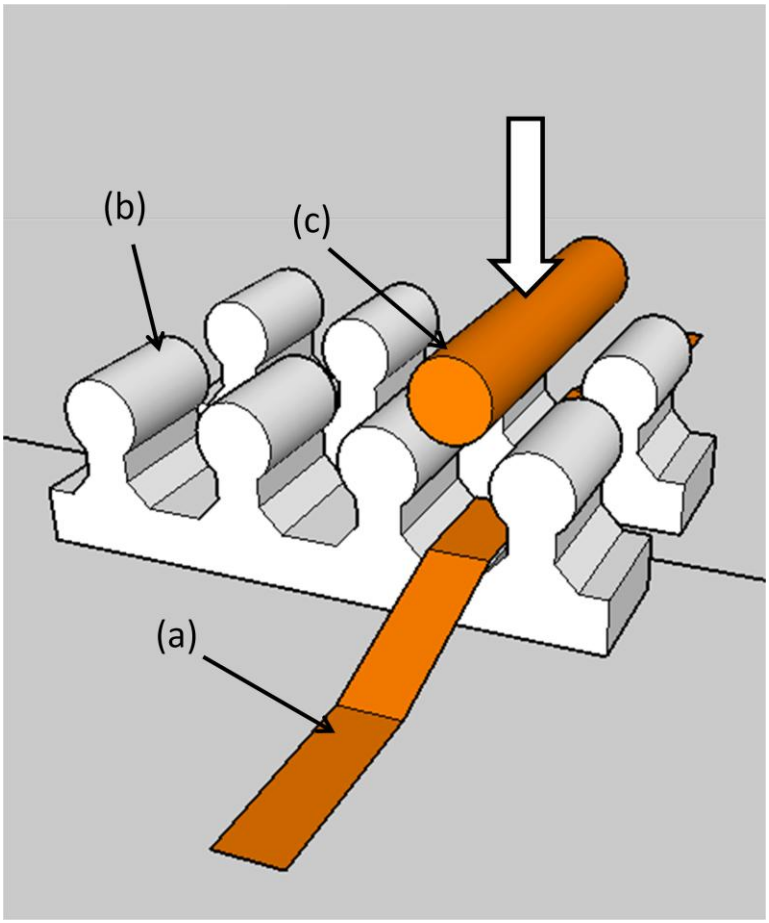

Figure 5-5. *In-situ connection idea and fix*

a) copper foil lead to the magnetic coils, b) nylon clamp array, c) copper wire which press fits into the nylon clamp.

5.4. Current supply

The current supply for the coils is a home-made, 8-channel, programmable, low noise current supply. It is described in some detail in Ebert (2010), a Penn State undergraduates Honors thesis, so I will only give an overview here. The design is based

on a stable voltage digital to analog converter (DAC) and a low temperature coefficient of resistance (TCR) resistor to produce a stable current. The low TCR resistor has a resistance of ~100 kΩ and a TCR of 0.2 ppm/ °C. Such a design is stable under drifts of the magnetic coil resistance.

The DAC is the Analog Devices part AD5542C, a 16-bit DAC with 31.2 μV resolution with a 2.048 V reference (Analog Devices ADR440B). When operated as a bipolar source the DAC has a resolution of 62.4 μV. With a 100 kΩ resistor this gives a least significant bit (LSB) of 312 pA, which will be used to compare noise and error sources.

The performance of the current source can be characterized with the integral non-linearity (INL), i.e., the deviation of the actual output from that expected from the DAC. Using a pico-ammeter (Keithley Model 6485 Picoammeter), the current output was monitored as a function of digital number. The INL was found to deviate as much as 3 LSB over the full range of output. This could be due to bit flip errors or individual differences in the elements which can be slightly unpredictable.

The long term stability was characterized by measuring the output of a single value every 28 seconds for 12.8 hours. The output was seen to fluctuate by ~40 pA, or ~0.15 LSB. As long as the long term stability can be met to less than 1 LSB, it should be possible to define a transfer function to correct the errors in the INL described in the paragraph above but this has yet to be implemented.

Chapter 6. Electric Field Plates

6.1. Plate manufacture

The electric field plates are central to the experiment. The goal is to apply ± 60 kV at a separation of 4 mm to produce a uniform electric field of 150 kV/cm. The central plate is the high voltage electrode while the outer two plates are grounded. A typical material for high-voltage electrodes is metal. However, for several reasons metal is not acceptable in our experiment. First, metal plates would not allow the type of optical access as illustrated in Figure 3-7. The second is that the Johnson noise associated with bulk metal electrodes would limit the sensitivity of the experiment. Instead, the plates are made of fused silica which can be machined to be very flat and polished to optical quality. They are coated with high-reflective (HR) and anti-reflective (AR) dielectric coatings to ensure the optical access we need. Furthermore the outermost layer of the plates is made of indium-tin-oxide (ITO) which is a transparent conductor. This allows the fused silica plates, which are otherwise insulators, to be used as the electrodes while allowing optical access.

The dimensions of the plates are 12” x 1.66” x 0.24”. The design drawings of the plates are given in Fang (2007). Their edges are curved with diameters of curvature equal to the plate thickness. The curvature is necessary because sharp edges can create peak electric fields that limit the applied electric field. There are blank holes on the outer surface of the two outer plates for plate mounting and electrical connection to ground and tabs on the top and bottom of the central plate for connecting the high voltage. The plates were manufactured by Stefan Sydor Optics.

The plates have a surface flatness of 1/2 wave (642 nm) per 1”. The parallelism between the two plates was quoted to be < 30 arc seconds. The wedge of the plates was independently measured using a wide He-Ne laser beam. The number of interference fringes from the etalon formed by the front and back surfaces of the plates were counted over a given distance as a measure of the wedge between the surfaces. The measured wedges were between 20 and 50 arc seconds. The wedges were constant along the width of the plate and rotated as much as 180 degrees from the top to the bottom of the plates.

6.2. Coating

In order to obtain the optical access shown in Figure 3-7, for the first iteration of the plate design, the surfaces of the plates are coated in the manner shown in Figure 6-1. The coating is uniform in the vertical direction. The coatings were done by Evaporated Coatings Incorporated (ECI). The center plate has a HR coating on each side. The measured reflection coefficients for these surfaces are > 97% for wavelengths 780-852 nm, random polarization, and AOI between 0 and 30 degrees.

The outer plates have AR coatings on either side. They have reflection coefficients < 0.25% for the wavelengths between 780 nm and 852 nm, random polarization, and AOI between 0 and 30 degrees. The total transmission coefficients are > 96%. The entire measured spectral curves, as measured by ECI are shown in Appendix C.

The ITO coating is continuous around the entire center plate. The inner surfaces as well as the curved edges of the outer plates were coated with ITO. The outer surfaces were not coated with ITO on the first iteration of the plates in an attempt to reduce the absorption associated with the ITO. This turned out to introduce a problem in the

application of high voltage, as shall be discussed in Section 6.4.4. The ITO coatings are on average 30 nm thick and have sheet resistances of 350-555 Ω/sq.

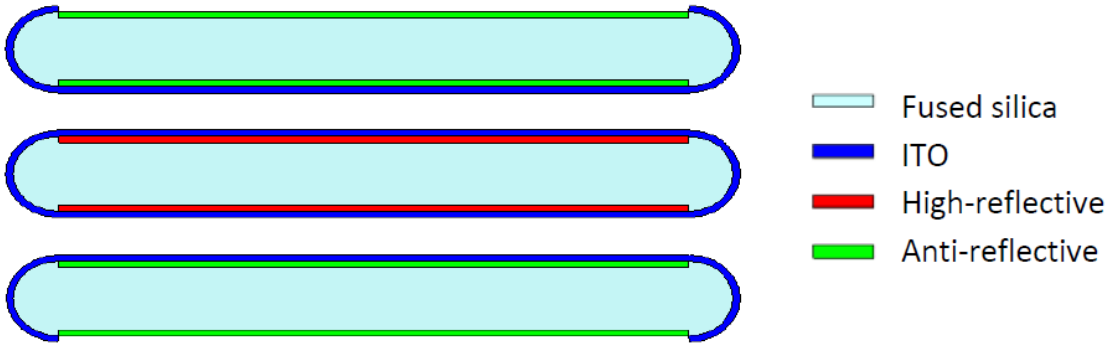

Figure 6-1. *Plate coating schematic*

6.3. Mounting

Mounting the plates is a non-trivial engineering problem. Because they are glass, the plates are fragile. They must be mounted with uniform separation to ensure uniform electric fields. They must be mounted inside of the 1m long glass cell, and the high voltage lead and ground leads must be fed out of the vacuum chamber so that the electrical circuit of the plates is isolated from the vacuum chamber. The mounting must be stable enough to survive the installation procedure as well as bakes up to 120 °C. Further, the mounting is inside an ultra-high vacuum, must be non-magnetic, and must be compatible with voltages as high as 60 kV. This places stringent conditions on the materials that can be used and the geometry of the mounting.

6.3.1. Glass spacers

In order to ensure a very uniform plate separation we use precisely machined fused silica spacers between the plates. The fused silica spacers have a low enough conductivity that they do not lead to significant leakage currents, as described by Fang (2007).

The fused silica spacers are 0.375” in diameter, and are 0.157” (4 mm) thick. They are specified to have thickness with a tolerance of ±13 μm, and a wedge of less than 5 arc seconds. The spacers were also manufactured by Stefan Sydor Optics.

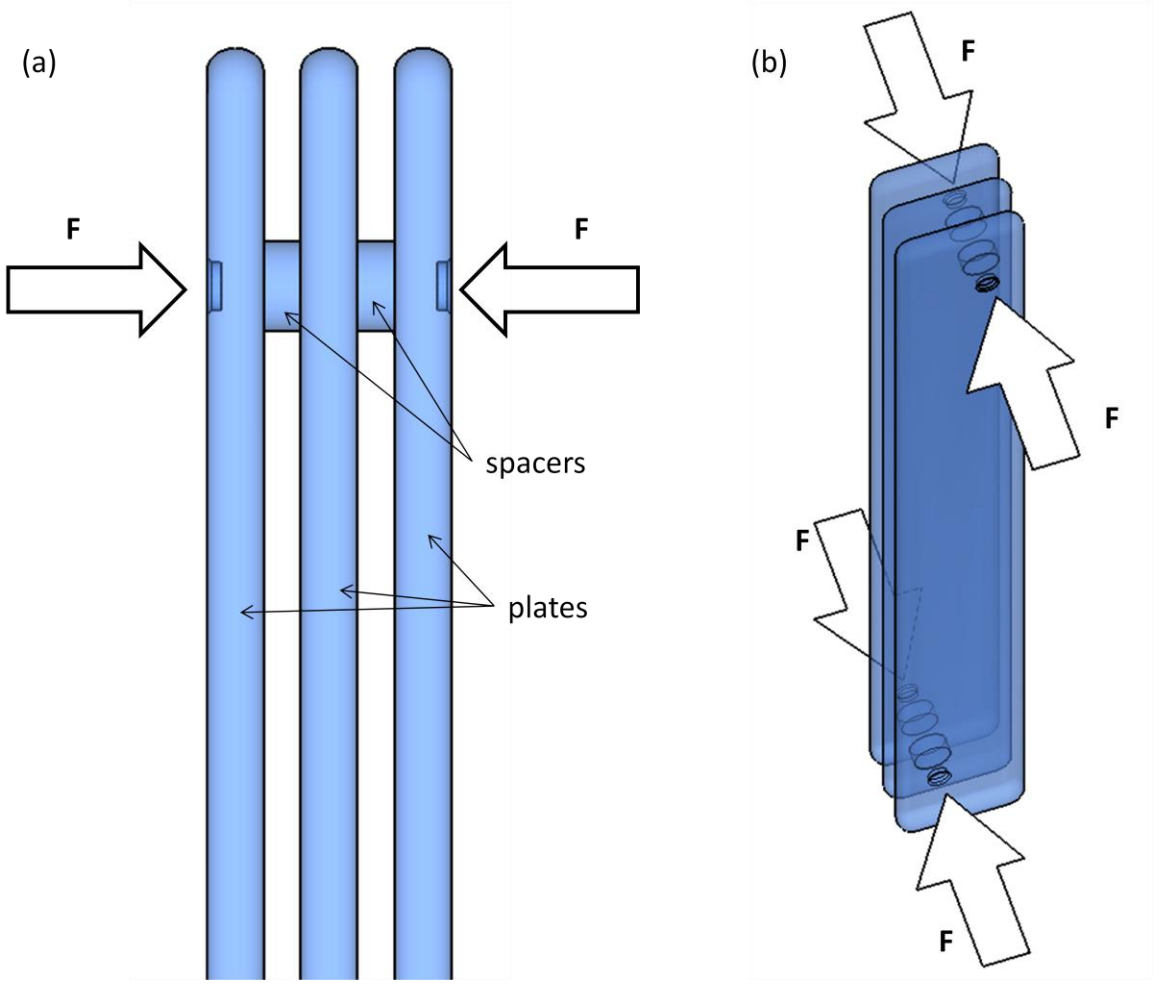

Figure 6-2. *Plate mounting with spacers*

The fused silica spacers are aligned with the holes placed on the outer facing sides of the outer plates as shown in part (a) of Figure 6-2. A force, ***F***, is applied on the blank hole such that the friction between the plates and the spacers keeps them from falling apart. There are two sets of holes and spacers for the mounting on opposite ends of the plates as shown in part (b) of Figure 6-2.The holes are on opposite sides of the plate width so that the optical cavities can pass through the center without hitting the spacers. To ensure their clearance through the plates, the vertical cooling beams for the optical molasses in the measurement region are aligned at an angle with respect to the cavities that is the opposite angle that of the spacers. The blank holes are 1” from the edges in the vertical direction and 0.41” in from the edge in the horizontal direction.

The challenge for the mounting is how to apply a controllable force at the locations indicated in part (b) of Figure 6-2 while meeting all of the constraints and requirements mentioned in the previous section.

6.3.2. Titanium mounts

The solution to this problem is based on a set of titanium clamps. The clamps are made of titanium because, unlike steel, it is non-magnetic and it has mechanical properties that are suitable for the mounting. A simplified drawing of the clamps is given in Figure 6-3.

The full design drawings of the clamps are given in Appendix D. The clamp body holds a hammer arm at an angle so that the hammer head aligns with the holes on the plates and the glass spacers. The hammer heads have a radius of curvature that allows

them to be seated in the blank hole on the plates as shown in the right side of Figure 6-3.

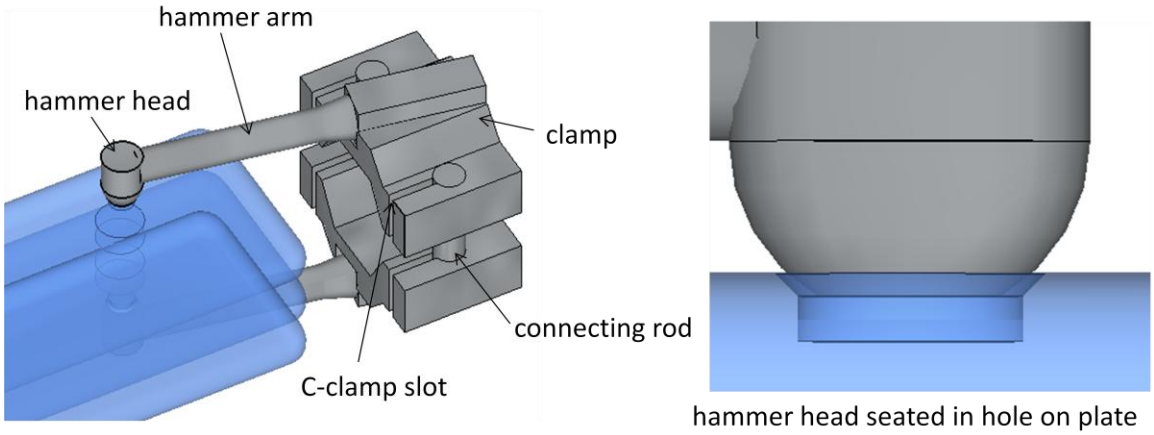

Figure 6-3. *Schematic of titanium clamps*

The two clamps are connected by two connecting rods. These rods are in a tight fitting hole on the clamp which has a C-clamp-like slot on it. The clamps can be pushed together while the connecting rods are allowed to slide so that the hammer heads compress the spacers, and then the rods can be locked in place with a screw that tightens the C-clamp slot, compressing the connecting rods.

All of the screws are made of titanium. All of the screw holes are vented to prevent virtual leaks. All of the corners and edges of the clamps and hammer arms are machined to have a radius of curvature in order to prevent peak electric fields. In order to prevent the machine tools from chipping and embedding magnetic materials into the titanium, all tools that were used to machine the titanium were coated with an Alcrona (AlCrN) coating. Titanium has a low heat conductance and can get very hot, and it also tends to be gummy when machined. Alcrona coatings are hard and perform well at higher temperatures. Using specially coated tools and making sure that the machining is done slowly and carefully minimizes the risk of contamination from the machining

process. In addition, all of the titanium pieces were electro-polished before finally being mounted in order to reduce any micro sharp edges.

6.3.3. Mounting procedure

The compression mounting described in the previous section must be done in a controlled and reproducible way to ensure the safety of the plates. A special mounting jig was designed for this purpose as shown in Figure 6-4. The pushing was done with a translation stage, (e) in Figure 6-4, through a load cell (Cooper Instruments LFS 210) (d), so that the applied force would be known and consistent for each attempt. We found that when the clamps were compressed with something between the hammer heads, the torque on the clamps caused a stress on the connecting rods that prevented them from sliding in the close-fit slots. A torque-balance piece (f) was added off of the back of the clamps eliminating the overall torque on the clamps from the pushing force. The torque balance piece can be removed after the clamps are tightened.

In addition, if the pushing on the clamps is not uniform they tilt, resulting in the same sort of stress on the connecting rods. Using an adaptor piece (c) to push the clamps simultaneously on all four corners solved this problem. With the combination of the torque balance and the uniform pushing, as much as 120 lbs of force could be applied to the clamps while still allowing the connecting rods to slide freely in the slots.

The clamps for the two ends of the plates are mounted on a linear rail (g) that runs the length of the plates. This alleviates any transverse stresses that might be applied to the plates if the hammer heads are not initially perfectly aligned with the blank holes on the plates.

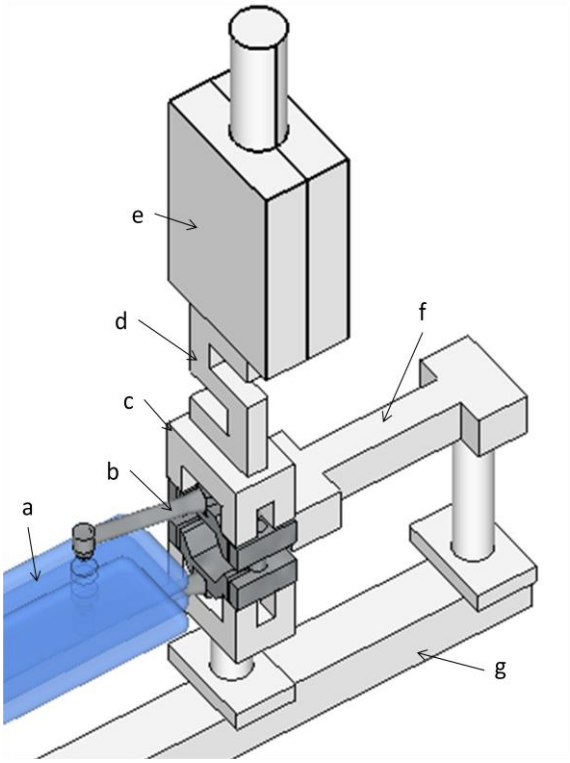

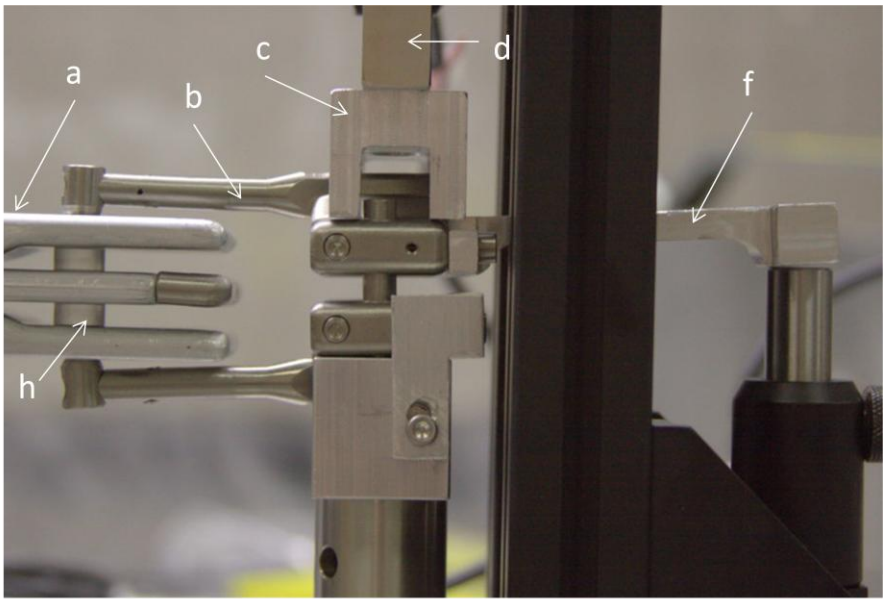

Figure 6-4. *Drawing and picture of mounting jig*

a) plates, b) titanium clamps, c) uniform pushing adaptor, d) load cell, e) translation stage, f) torque balance piece, g) linear rail, h) spacers.

The jig was tested extensively on aluminum plates that have the same shape and blank holes as the actual plates. Because it is not possible to directly monitor the force on the hammer during the actual mounting procedure, the first test is to calibrate the force on the hammer arm as compared to the force applied on the clamp. A second load cell is placed below the hammer head, and the force on the hammer head was plotted against the applied force. The results are shown in Figure 6-5. The results are for seven independent trials over the course of a few days, disassembling and reassembling the mounting jig between trials to ensure reproducibility. The result is that the force on the hammer head is one third of the applied force. If the system were perfect, we might expect a slope of a half, rather than a third, because the force would be equally distributed between the hammer head and the torque balance piece. The discrepancy likely stems from a slight tilt or bend in the clamps or hammer arms. The standard deviation of the data in Figure 6-5 is 1.7 lbs. This ensures that we can apply as much as 40 lbs to the hammer heads with an uncertainty of 5%. Above 120 lbs applied force, the translation stages became difficult to operate.

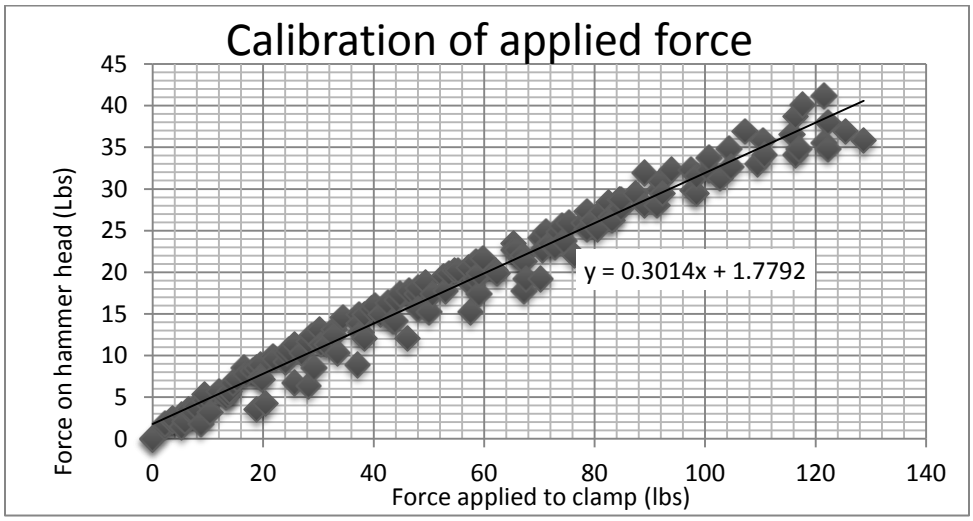

Figure 6-5. *Calibration of applied force*

In order to verify that the pushing in fact behaves in a predictable manner, the coefficients of friction were measured of the center plate with respect to the spacers. Three test plates with spacers were mounted between two clamps. The center plate was then pushed transversely with a load cell to the force of the hammer heads. The force at which the center plate started moving (static coefficient of friction) and the force on the center plate for a sustained linear motion (dynamic coefficient of friction) are plotted against the force on the hammer heads in Figure 6-6. The results are a static coefficient of friction of 0.24 and a dynamic coefficient of friction of 0.28.

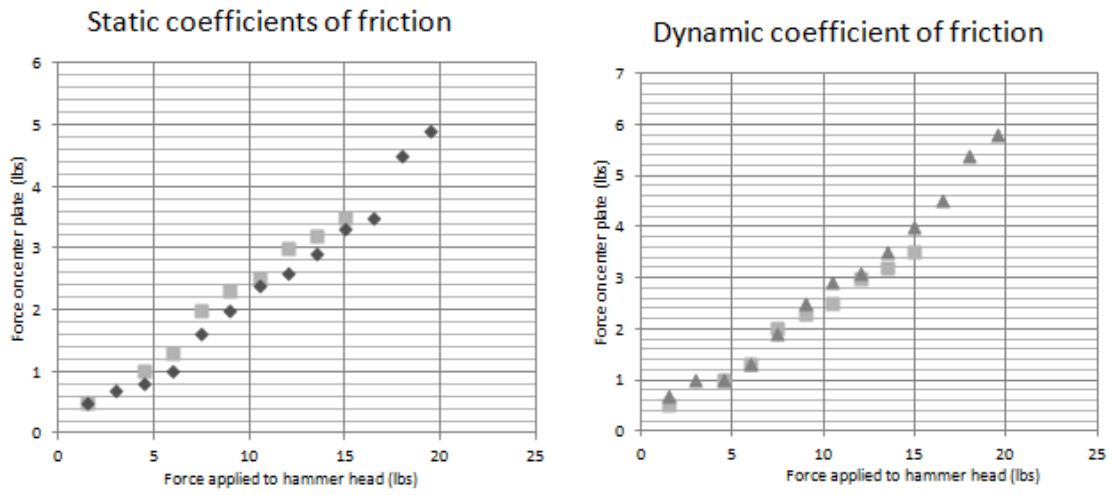

Figure 6-6. *Coefficients of friction*

The final test on the mounting was testing the effects of a bake. The three test plates and spacers were mounted on the clamps with the maximum force between the hammer heads of 40 lbs. Then the setup was placed into a standard kitchen oven and was baked at 200 °C for several hours. Then the oven was cooled off and the plates and clamps were allowed to cool before being visually inspected for any cracking or slipping.

This procedure was repeated several times, sometimes with weights dangling off of the center plate. Up to 3.8 lbs dangling off the center plate, there was no evidence that any damage to the plates or slippage occurred during the baking.

6.3.4. Mounting to chamber

So far we have described how the plates are mounted together and now we will describe how they are mounted into the glass cell. There are four long titanium legs that attach to the back of the clamps. These run up the glass cell and are secured to a stainless steel ring holder. Stainless steel is acceptable here because the ring holder is far enough away to be outside of the shields. As will be described in the following section the legs must be electrically isolated from the ring holder because they also provide the electrical connection to ground. The legs thread alumina beads that are inserted into holes in the ring holder to insure isolation. In addition, stainless steel springs are attached on either side of the ring holder so that the weight of the plates is actually suspended on the springs. This provides strain relief if there is any expansion of the cell during a bake, as well as some strain relief as the mounting is tied in place. The connection to the ring holder is shown in Figure 6-7. Also seen in Figure 6-7 is the ring holder installed in the flange of the glass cell. The tab on the flange fits into the detail on the ring holder so that it can be aligned.

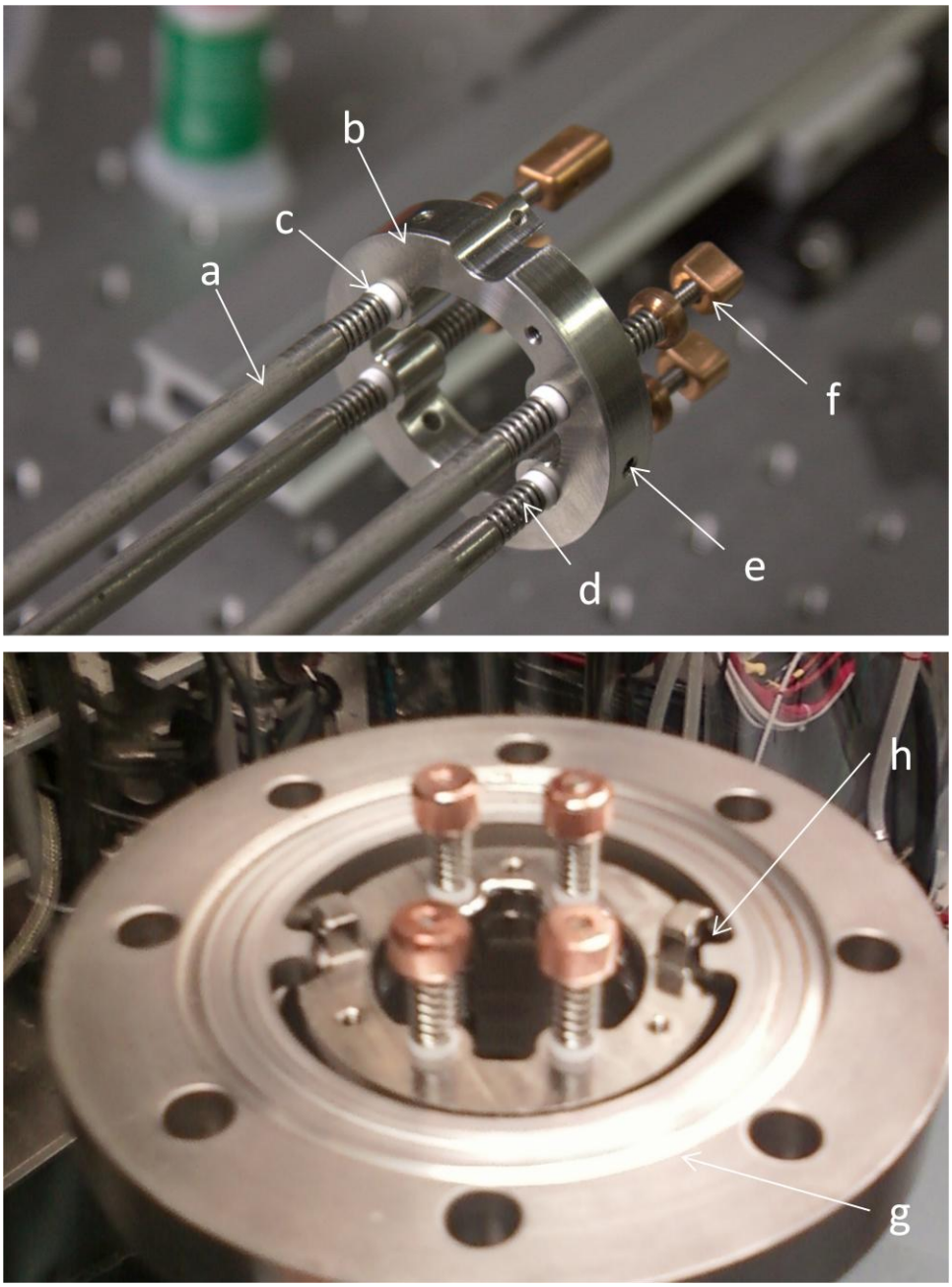

Figure 6-7. *Picture of ring holder*

a) titanium legs, b) stainless steel ring holder, c) alumina beads for electric isolation, d) stainless steel springs for strain relief, e) tapped hole for set screw, f) copper nuts for ground connection, g) glass cell flange, h) tab for aligning ring holder.

The ring holders attach to a specially designed flange on the glass cell. Three set screws are screwed out of the ring holder into a slot machined in the inner radius of the flange to hold the ring holders in place.

I will briefly describe the entire mounting procedure from beginning to end. First, using two identical mounting jigs on either side of the plates, the force is alternately increased up to a total of 40 lbs applied at the hammer heads and the connector rods on the titanium clamp are tightened into place. At this point, the torque balance piece, and much of the mounting jig can be removed. The clamps are then held tightly while the legs and ring holders are attached on either side of the plates with the assembly shown in Figure 6-7. The ring holders are attached to a rail which is gently lifted and rotated until the plates are vertical. It should be noted that in this arrangement, the plates are free to rotate in the plane of the plates, so when being lifted the plates must be kept horizontal. The rail holding the plate structure is then attached to another rail that vertically dangles the plate structure over the glass cell. The rail jig is slowly lowered with a winch, guiding the plates into the cell. When the plates are in the center of the glass cell, the set screws on the ring holder can be tightened into the flanges, and the glass cell and plate structure are one ‘solid’ piece.

Then the cell can be mounted onto the chamber. There are further complications with this aspect of the mounting which have to do with the electrical connections. We shall discuss this in the following section.

6.3.5. Electrical connections

As we have briefly mentioned before, the center electric field plate is connected to the high voltage and the outer two plates are connected to ground. We make the

electrical connections to the plates on both the top and the bottom in order to ensure most of the leakage current that might flow along the spacers does not flow next to the atoms. With the connections made on the top and the bottom, the leakage current should take the path closest to ground, the amount of current that flows along the plates should be suppressed by about an order of magnitude.

The ground connection is made through the titanium legs. Wires lead from the copper nuts at the top and bottom of the legs, as seen in Figure 6-7, and run to vacuum feedthroughs on the top and bottom 6-way crosses as seen in Figure 3-1. The legs are connected to the clamps, and a special copper foil piece, which is connected to the hammer arm, is pressed against the plate to ensure a stable electrical connection. This can be seen in Figure 6-8. Due to issues related to those discussed in Section 6.4.4, this ground connection will be changed on a subsequent iteration of the plate mounting because the sharp corners of the copper foil could potentially produce a peak electric field.

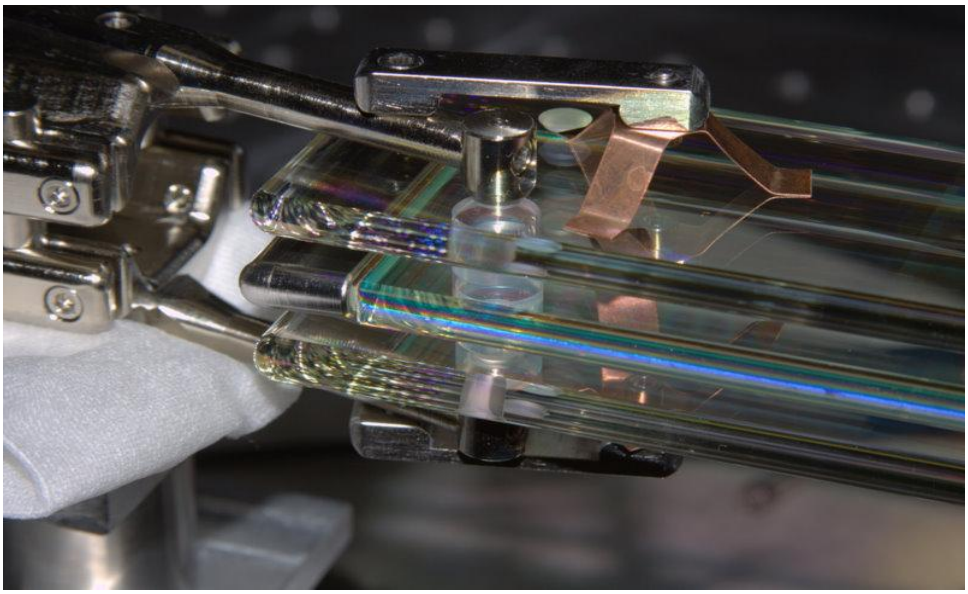

Figure 6-8. *Ground connection to plates*

A lot more care needs to be taken with the high voltage connection. The high voltage pin must always be kept a safe distance from any conductors near ground in order to avoid inducing peak electric fields that might lead to arcing. In addition, all of the materials in the high voltage path must be rounded and polished to avoid high fields.

The high voltage is brought into the vacuum chamber with high voltage feedthroughs (MDC part # 9442013-PWR–60kV–3AMP) in the top and bottom 6-way crosses. The stainless steel pin from the HV feedthrough fits into a clearance hole on a copper connecter, as shown in Figure 6-9. It is held in place with a set screw. In addition there is a titanium rod which fits into a second clearance hole on the copper piece and is also held with a set screw. This titanium rod leads up to the center plate. It comes into the copper piece at an angle so that the copper piece is away from the center of the chamber to allow the lattice and cooling beams to pass. All clearance holes on the copper piece are machined to have rounded corners to avoid peak electric fields and the set screws fit entirely within the piece.

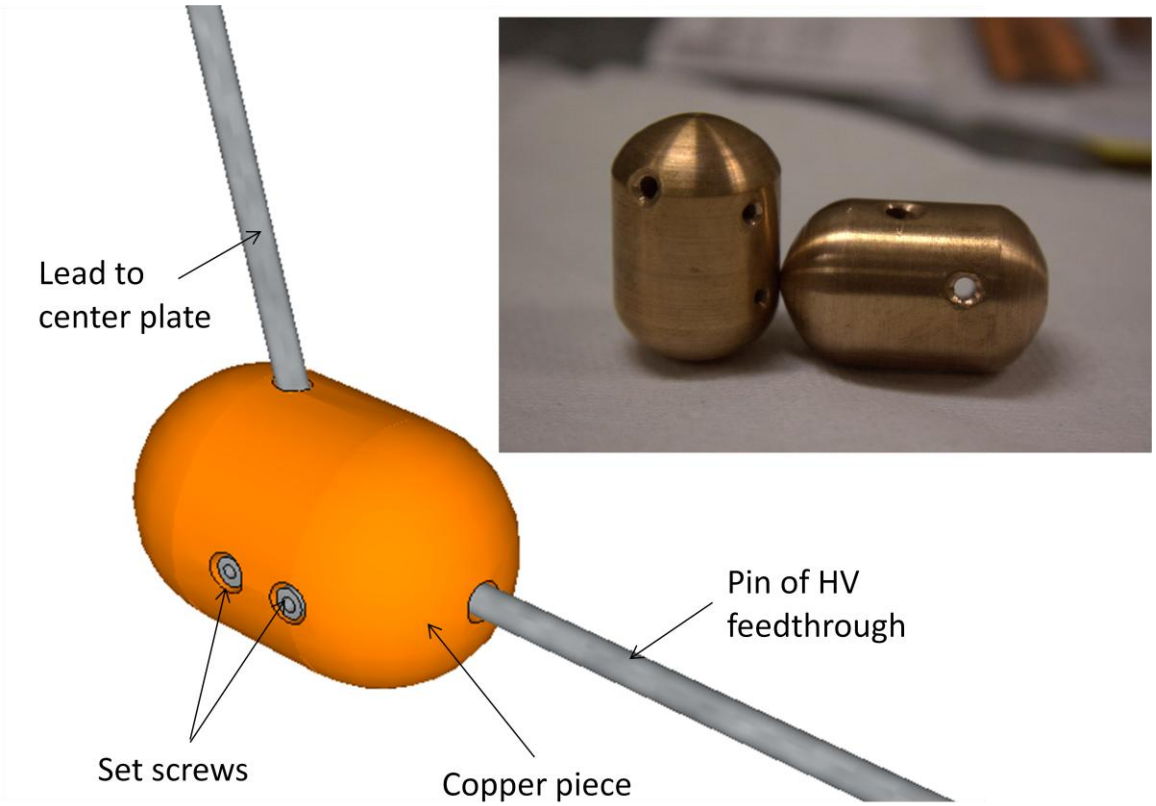

Figure 6-9. *Copper connector*

To understand how the electrical connection is made from the titanium rod to the center plate we must describe an aspect of the center plate design that has not been mentioned. The glass part of the center plate in fact has a tab on the top and bottom. A titanium cap fits over the tab so that when a folded 5 mil copper foil is nested inside the cap and the cap slid over the tab, the bend in the copper provides enough springiness to hold the titanium cap in place. This is shown in Figure 6-10. The tab surface of the plate is coated with ITO such that the conductivity is continuous from the tab surface to the face of the plates. The titanium rod then screws into a tapped hole on the top of the titanium cap. The titanium cap design is also given in Appendix C. As with the ground connections, there are identical connections made on the top and bottom of the plates.

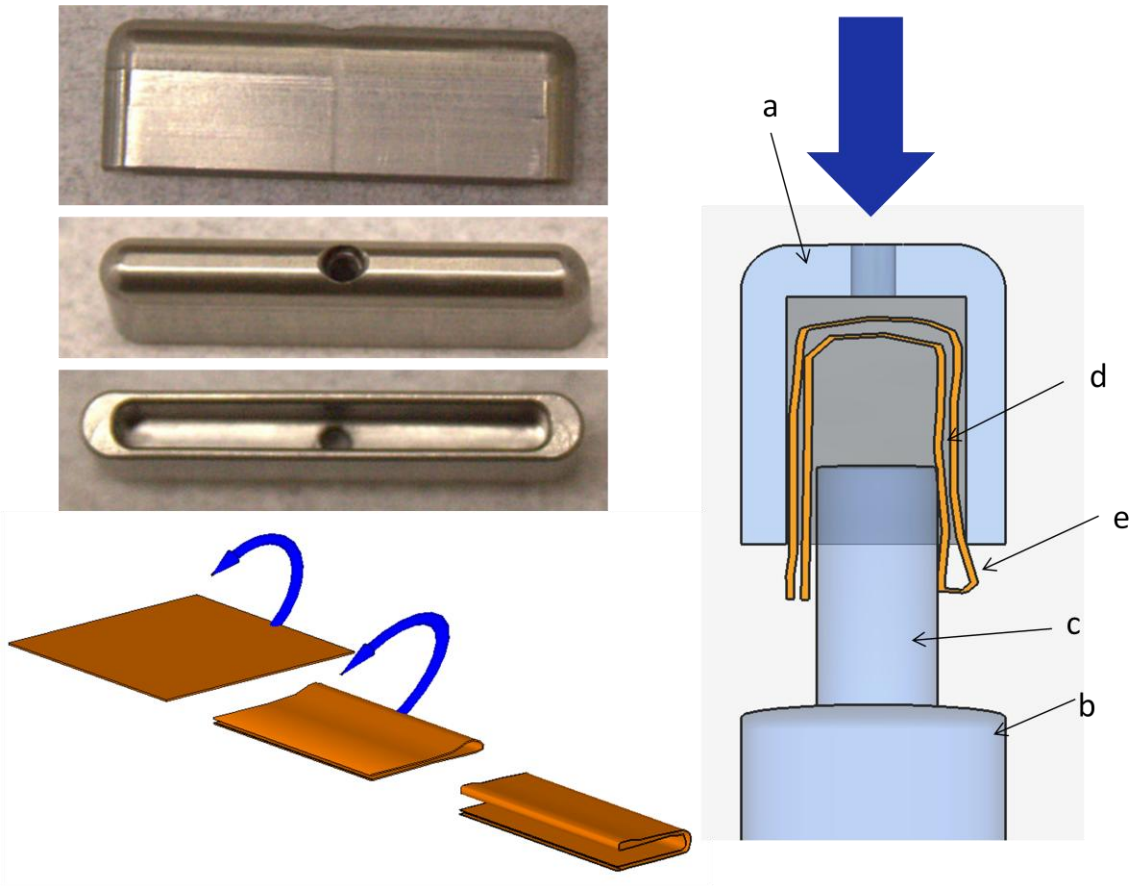

Figure 6-10. *Titanium cap and HV connection to plates*

Top Left: Three views of the titanium cap. Bottom Left: A 0.9" x0.9" x 0.005" copper foil square is folded twice. Right: cross section of connection, a) titanium cap, b) plates, c) tab on top of plates, d) copper foil sits around tab, e) the circle of the fold in the copper foil compresses as the titanium cap is pressed onto the tab.

Many aspects of the mounting system (e.g. the titanium clamps, the titanium cap, the stainless steel ring holder, etc.) were modeled using COMSOL Multiphysics to ensure that they would not produce a peak electric field larger than that produced at the plates.

The mounting procedure is complicated because the high voltage electrical connections sit above and below the length of the glass cell and must not touch anything else. The copper connector needs to be rigidly held in place during the mounting

procedure until it can be attached to the high voltage feedthrough pin. Otherwise there can be a lot of stress applied to the center plate. This was accomplished with a ‘scissor’ like holder piece that, when extended, secured to the ring holder. When the high voltage feedthrough pin was connected, the temporary piece could be removed through a separate flange on the top and bottom vacuum chambers. Figure 6-11 shows some images of the installed plates with various pieces identified.

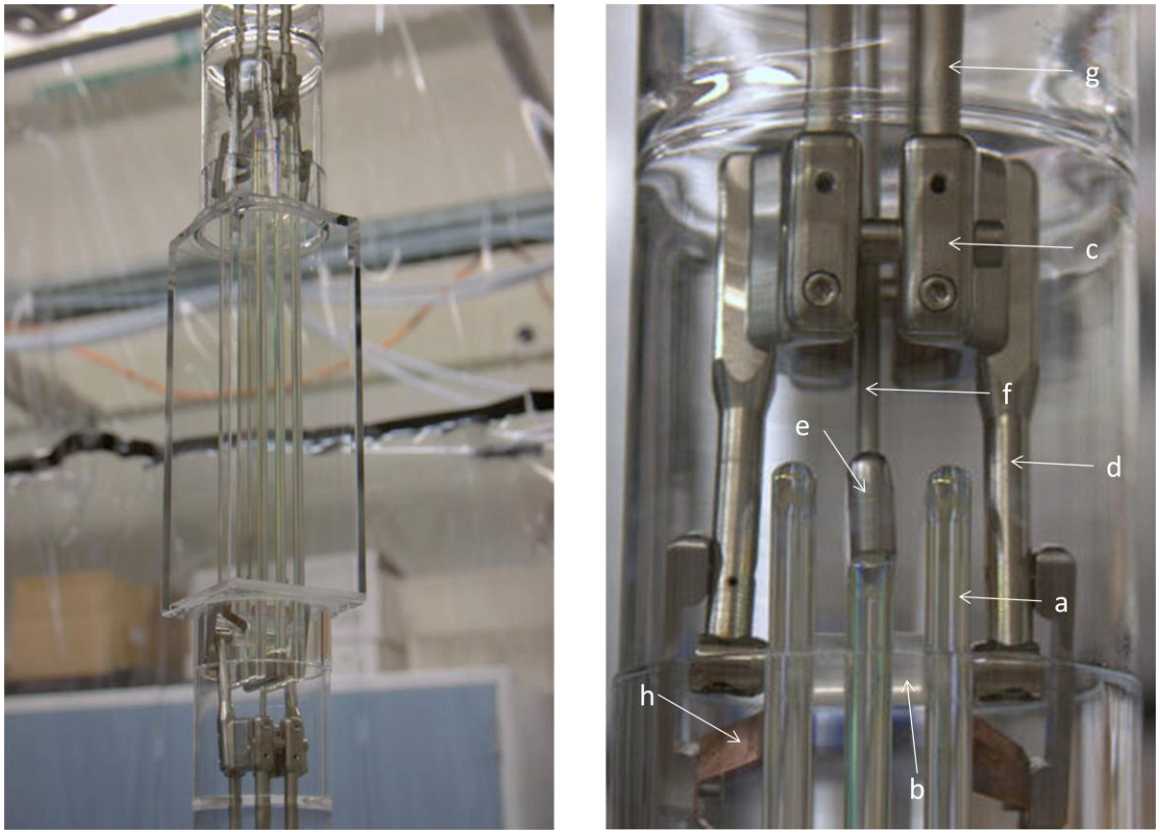

Figure 6-11. *Installed plates*

a) plates, b) spacers, c) titanium clamps, d) titanium hammer, e) titanium cap, f) center HV rod, g) titanium support rod/ground connection, h) ground connection to plates.

6.3.6. Plate separations

The separation of the plates was measured in situ using a white light interferometer based on the work of Patten (1971). The plate separation measurements will be described in more detail in Zhu (*forthcoming*). The basic design of the measurement uses a broadband light source in a Michelson style interferometer. If one of the arms of the interferometer partially reflects off two separate surfaces, then sets of interference fringes can be observed as the length of the second arm is adjusted. These interference fringes will occur when the length of the second arm is equal to the optical lengths of the paths that reflect off of one of the surfaces. In our case, the two partially reflecting surfaces are the inner surface of the outer plate and the HR surface of the center plate. The second arm has a mirror on a translation stage, so that the distance between the sets of interference fringes can be measured as accurately as the precision of the translation stage.

A broadband light source is needed because if a single frequency source is used, the interference fringes will be periodic. The broadband light source must have a coherence length shorter than the plate separation. Then the measurement of the plate separation can be made as accurately as the translation stage that is on the mirror in the second arm of the interferometer.

This method cannot be used to measure the thickness of the plate because the dispersion in the glass is different for the two paths of light, and the contrast of the interference fringes is lost. The results are summarized in Figure 6-12. I show the separation between the plates along a vertical line of the plates as well as the wedge in the x direction as a function of the vertical position. These graphs show a parabolic shape along the vertical direction. Over ~5 cm, the plate separation changes by as much

as 6 μm, which corresponds to a wedge of 120 ppm. At the center region, near the maxima of the parabolas, the wedge is more like 0.5 to 1 μm over 2 cm (.25 to .5 ppm). The wedge in along the x direction varies along the vertical and ranges between -20 and 150 ppm for the two different plate separations.

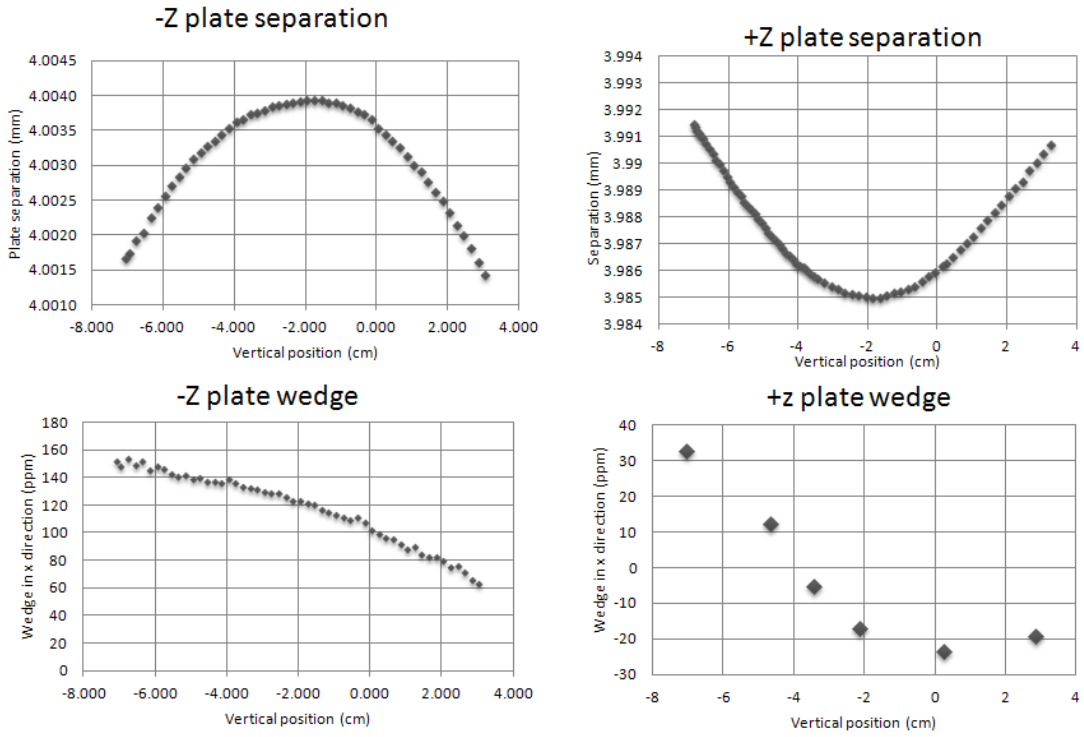

Figure 6-12. *Plate separation data*

6.4. High voltage system

6.4.1. Voltage supply

The voltage is provided by a pair of high voltage power supplies (Glassman High Voltage model# PS/EH 60 PO1.5), one operating at a positive voltage and the other at a

negative voltage. A home-made relay gives the ability to switch between positive voltage, negative voltage, and ground. The voltage is carried on a coaxial cable (Coaxial Cable Systems RG-8U) which is shielded with a tinned copper sheath to reduce noise from RF-pickup.

An equivalent circuit diagram of the entire high voltage system is given in Figure 6-13.

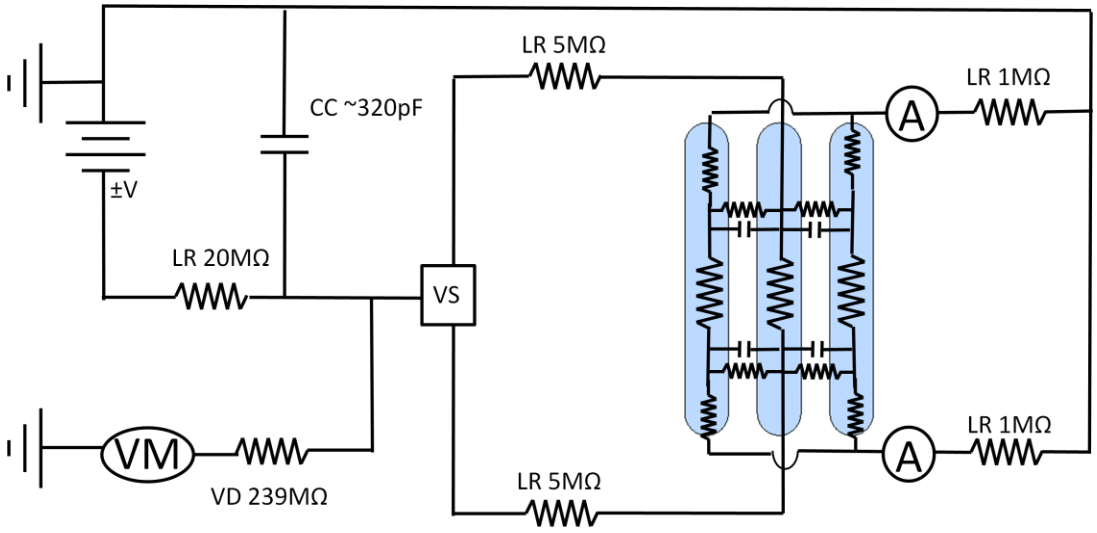

Figure 6-13. *Equivalent circuit diagram of high voltage system*

The voltage supply is on the left. LR = various current limiting resistors, CC = the capacitance of the longest length of coaxial cable. VS = voltage splitter, VD = 1000:1 voltage divider, VM = volt meter, A = pico-ammeters. The resistance of the center plate is a total of 527 Ω. The total parallel resistance of the ground plates is 330 Ω. Assuming the leakage current is all along the spacers, the total parallel resistance of the four spacers connecting the plates is ~1-2 GΩ. The total parallel capacitance of the plates is 54 pF.

The 20 MΩ resistor directly after the voltage supply is necessary to limit the peak charging current. Without this resistor, the large currents during charging or discharging can produce RF fields which can cause the computer to crash. The length of coaxial cable (~10 m) from the high voltage source to the vacuum chamber is the largest source of capacitance in the system at ~1 nF. The voltage is divided by 1000:1 voltage divider (Ross Engineering Corp. model# 60-6.2Y-BD-LD-ALBD) which has a 239 MΩ resistance

to ground so that the voltage can be monitored in real time to ~1 ppm using the digital multi-meter (Agilent 34401A).

The voltage is then split with a commercial high voltage splitter (High Voltage Concepts LLC), so that it can be sent both to the top and bottom 6-way crosses to connect to the top and bottom of the plates. A 5 MΩ resistor in each path is used to limit the possible circulating current in the loop that runs from the splitter through the plates. Such a current could be caused by a thermo-electric effect associated with the dissimilar conductors along the current loop, i.e., steel, copper, titanium, and ITO. The sheet resistance of the ITO on the center plate gives a measured resistance of 527 Ω across the plate. Roughly 1/12 of that resistance is from above the spacers and 1/12 from below the spacers.

The gap between the center plate and the outer plates has a capacitance of 54 pF and a resistance of roughly 1 GΩ. The measurement of that resistance will be described in Section 6.4.3. For the purposes of this circuit diagram, we assume that the entire leakage current runs along the spacers. The two ground plates in parallel give a resistance of 330 Ω. Roughly 1/12 of that resistance is from above the spacers and 1/12 from below the spacers. The current from the plates to ground is monitored with pico-ammeters on both the top and the bottom in order to monitor leakage currents from the plates.

There is a large 60 Hz noise (~4 nA peak to peak) at the pico-ammeters presumably from inductive pickup in some of the various loops formed by the high voltage system. The DC current can be monitored to better than 50 pA with the 60 Hz noise filtered by a passive notch filter. Because the 60 Hz noise is so large, a small DC bias offset is measured with no applied voltage.

6.4.2. Previous high voltages tests

As described by Fang (2007), tests of a very similar high voltage system were performed on glass plates coated with ITO by Thin Films Devices. The test plates had a similar radius of curvature and were mounted in a similar manner with fused silica spacers. These tests were done with a 3 mm separation.

For a positive voltage, as much as 150 kV/cm (45 kV) could be applied before the leakage current began to rise non-linearly. At 150 kV/cm the steady state leakage current for positive voltage was less than 10 pA. A non-linear rise in the leakage current can be seen as a precursor to electric field breakdown. For negative applied voltage the leakage current at 66 kV/cm (20 kV) was as high as 2 nA. The asymmetry in voltage polarity is due to a well known effect in high voltage physics (Beukema, 1973). In essence the cathode will field emit electrons from its surface. Those electrons can be accelerated to another surface where they will dislodge adsorbed particles and create ions. Those ions can then be accelerated back towards the cathode and can result in a runaway breakdown process. The asymmetry arises because when the anode is at the same potential as the surrounding chamber, the ions emitted from the surrounding chamber will contribute to the runaway process. Whereas, when the cathode is at the same potential as the chamber, the ions created on the surface of the surrounding chamber will not be accelerated back to the electrodes. Thus, typically, electric field breakdown occurs at a lower absolute value of the voltage for negative charging than it does for positive charging.

Though the actual leakage currents and breakdown voltages depend on the geometry of the setup these tests serve as a proof of principle that glass plates coated

with ITO can be used for high voltage applications. They also show that the fused silica spacer will not allow significant leakage currents and will not damage the plates.

6.4.3. High voltage tests with plates

The high voltage system was tested with the glass plates described above. The charging current was monitored with the pico-ammeters as well as the voltage from the voltage divider. The results of the charging are shown in Figure 6-14. The peak of the charging current is measured with no filter because the filter can alter the real-time signal (a). The result is ~2 μA which is, within an order of magnitude, what is expected from 2 kV with a ~25 MΩ resistances. The charging current corresponds to a 40 ms exponential charging time constant. This suggests a charging current of 1 nA/V. A close up of the charging current is also shown without the filter (b). In this graph, the 60 Hz noise is clearly visible. The offset of the oscillation clearly goes to less than 1 nV. In order to see the near DC component of the charging current more clearly we measure the current with a 60 Hz notch filter (c). As the graph in Figure 6-14 shows, the charging current drops to less than 100 pA within a second of a 4 kV charging. The longer time scale decay of the charging current seen in the ranges of 10-40 seconds can be seen to be caused by a slow drift upward of the voltage as measured directly from the voltage divider (d). Over the first 40 seconds the voltage drifts by ~.1 V, which would imply a charging current of ~100 pA. This suggests that the long time scale charging current is solely due to the voltage drift, not a leakage current across the plates. This drift is associated with the changing of the load on the voltage sources as the relay is switched from ground to the high voltage. A feedback loop to the control on the voltage source can correct for this drift.

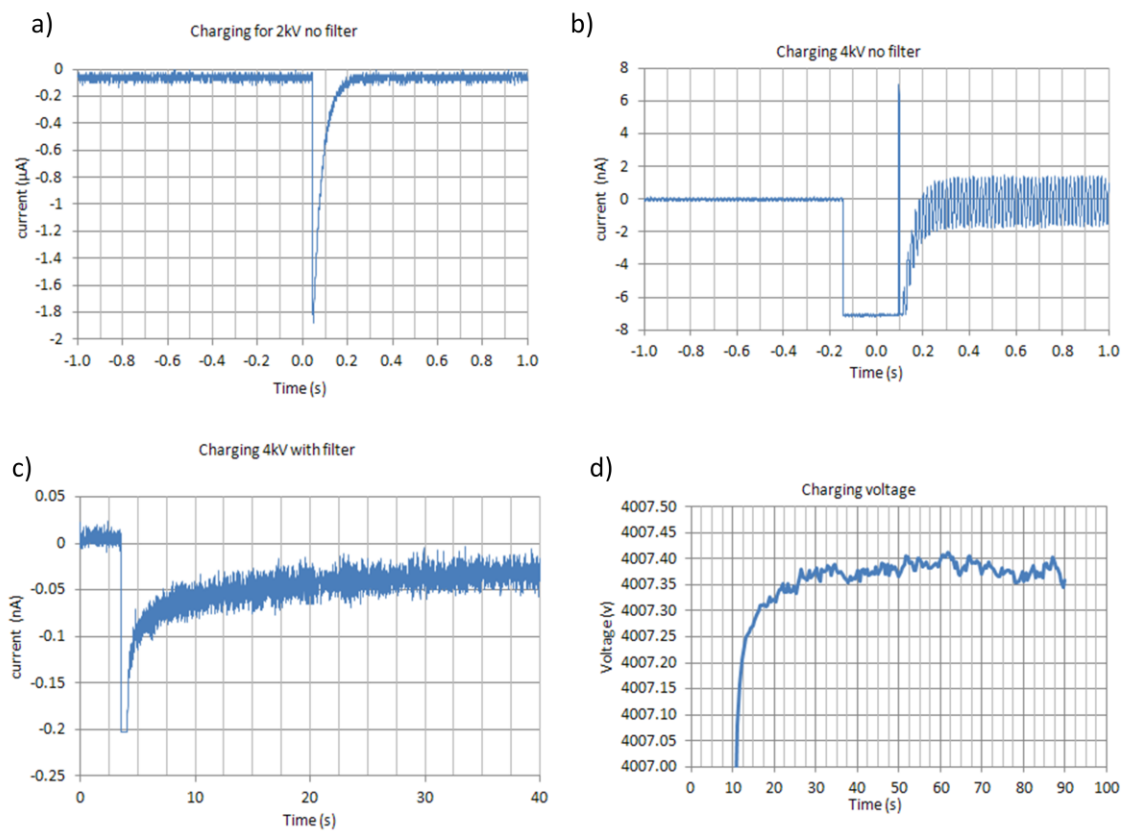

Figure 6-14. *Charging currents*

a) the charging current is shown for 2 kV, the peak is ~ 2 μA with a charging constant of 40 ms, b) a blown up picture of the charging current, only with 4 kV applied, the pico-ammeter is maxed out during the charging, but as the current drops below ~7 nA, the 60 Hz oscillation is visible as the offset of the current approaches zero, c) the charging current after a 60 Hz notch filter is applied shows the long time constant decay of the charging current, the current drops below 100 pA after ~1 second of charging, d) the voltage measured at the divider multiplied by 1000, during the charging time, the qualititative drift of the voltage over the first 40 seconds is ~100 mA.

In addition to monitoring the charging current, the steady state leakage current of the plates was measured as a function of voltage. Due to the drift seen in Figure 6-14, the steady state leakage current was measured many seconds after the voltage was applied to the plates when it became stable. In addition, when the voltage is changed, the voltage supply takes 15 to 30 minutes to stabilize before giving a steady value. The

results for the steady state leakage currents, measured with the 60 Hz notch filter, for voltages between -9 kV and 9 kV are shown in Figure 6-15.

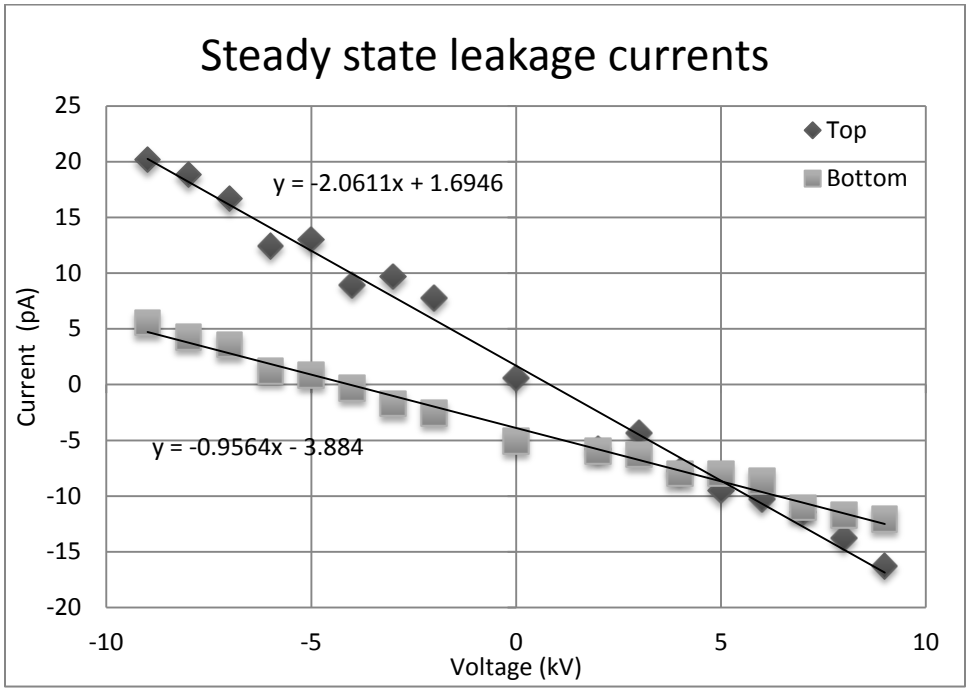

Figure 6-15. *Leakage current as a function of voltage*

This figure shows the steady state leakage currents measured by the pico-ammeters located in the ground path of the connections to the top and bottom of the plates for voltages between positive and negative 9 kV. The top has a steady state leakage current of 2 pA/kV, and the bottom shows 1 pA/kV.

As mentioned above, this steady state leakage current gives an equivalent resistance of the gap between the plates of roughly 1-2 GΩ. Further the steady state leakage current is reliably linear in this range of voltages. If this linear relationship were to hold up to 60 kV it would predict leakage currents in the range of 100 pA. This is within the range of what is acceptable for our experiment. The data for the bottom pico-ammeter shows a 5 pA offset at 0 V applied which comes from the residual of the 60 Hz noise that was not filtered out.

6.4.4. E-field breakdown

The goal of high voltage electrode design is to have the field between the electric plates be the peak field. That way, the electric field is limited only by the intrinsic properties of the electrodes and not some other design feature. With our curved electrodes, there is a peak field that is larger than the nominally applied field by about 20%. This was modeled with (COMSOL Multiphysics), and can be seen near the curvature of the center plate in Figure 6-16.

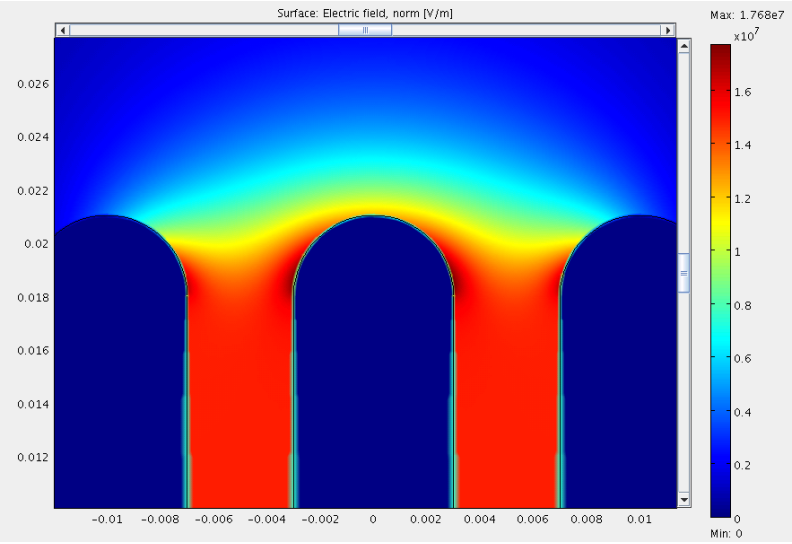

Figure 6-16. E*lectric field near plates*

Unfortunately, with the current plate setup, electric field breakdown occurred at 10 kV. When the voltage was raised from 9 kV to 10 kV the leakage current increased by at least an order of magnitude and a faint blue glow was observed coming from a spot on the plates. The voltage was shut off within a few seconds to minimize damage to the plates. Small patches of discoloration were observed on the rounded edges of the plates with the majority of the damage being on the center plate. It is important to note that the electric field breakdown was observed on positive 10 kV and not on -10 kV. To avoid

further damage to the plates which could possibly expel flecks of coating into the vacuum chamber, the negative breakdown was not tested further.

The explanation for this relatively low breakdown voltage has to do with the geometry of the coating. Figure 6-1 shows that the ITO does not extend across the back of the ground plates. This was done to minimize absorption loss from the ITO. However, this creates a thin edge of conducting ITO. The coating is 30 nm thick and it may taper out into an even sharper edge. Even though this plate is grounded, and there is no direct line of sight to the high voltage electrode, the field lines that curve all around the entire plate concentrate to the ITO edge and produce a peak electric field larger than that in Figure 6-16.

One piece of evidence for this explanation is the fact that breakdown occurred with positive voltage before negative voltage. This is the opposite polarity of the field emission effect described in Section 6.4.2. This suggests that at 10 kV, the peak electric occurred at the thin edge of ITO, such that the ground plate, being relatively negatively charged, was the emitter of electrons that lead to catastrophic breakdown. At -10 kV, the ground plates are relatively positively charged and will not release charge carriers as readily.

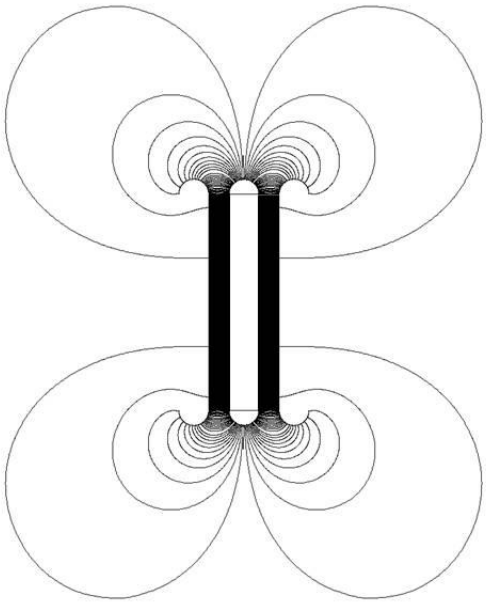

Figure 6-17. *Electric field lines of plates*

Another piece of evidence for this cause is the location of the damage observed on the plates. Electric field lines lead directly from the curved edges of the center plate to the thin edge on the back of the ground plates as seen in Figure 6-17. Electrons emitted from the thin ITO edge would tend to follow the electric field lines to the curved edge of the center plate.

Finally, we used COMSOL Multiphysics to conduct a series of static electric field simulations to model a thin conducting edge located on the back of the ground plates. Because the 5 order of magnitude difference between the 30 nm thickness of the thin film and the 6 mm thickness of the plates made direct simulation infeasible. Instead, thicker ITO edges were modeled and the results showed a clear dependence that could

be extrapolated down to 30 nm. The results of one such simulation are shown in Figure 6-18.

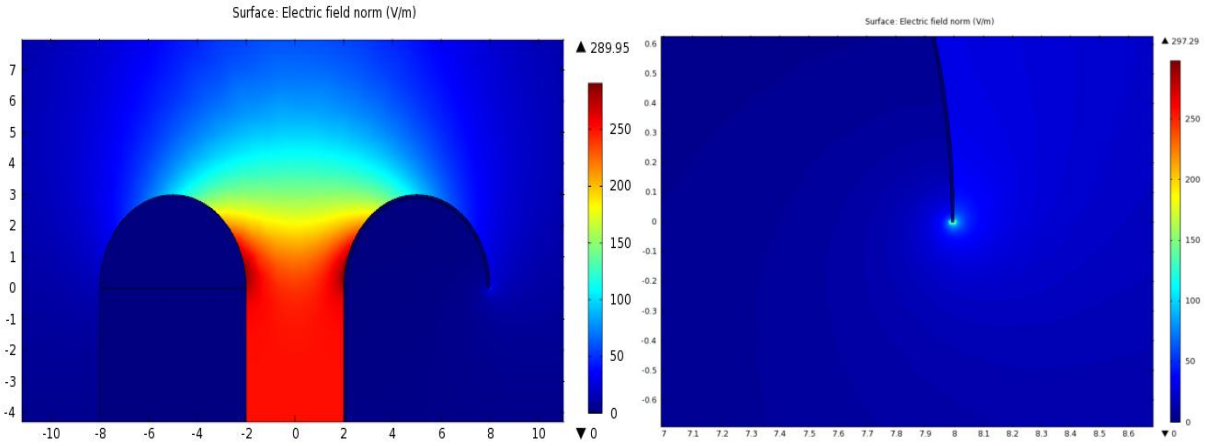

Figure 6-18. *Peak electric field at the thin ITO edge*

The peak electric field near the knife edge as a function of film thickness is shown in Figure 6-19. For these simulations, 1 volt was applied to the center plate, giving a nominally applied electric field of 250 V/m. Extrapolating the curve down to the 30 nm thickness gives a peak field of ~2000 V/m, eight times the nominally applied field. This, as well as the evidence given above, seems to give a plausible explanation for why the electric field broke down at a voltage more than five times smaller than what is expected and what was tested with the test plates.

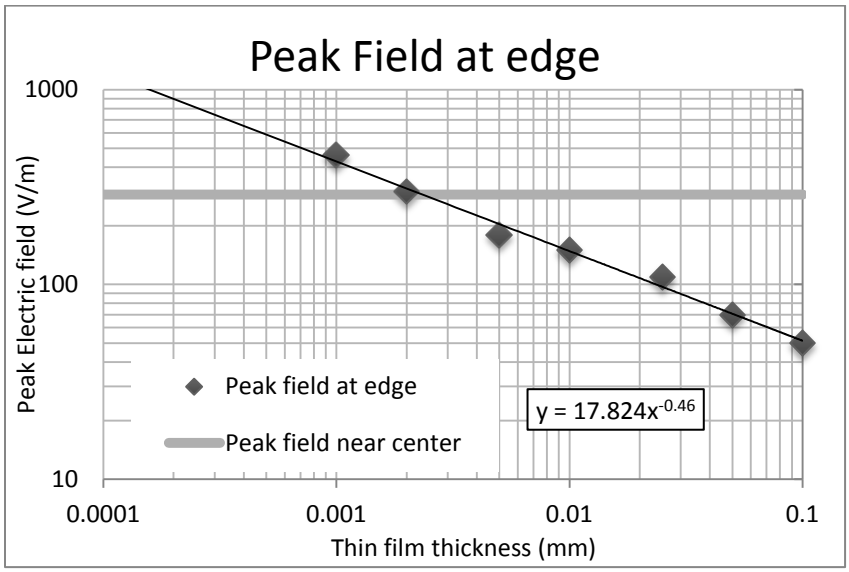

Figure 6-19. *Peak electric field as a function of film thickness*

Fortunately, the solution to this problem is conceptually simple; extend the ITO coating across the entire back of the plate. However, the manufacturing of the plates, their coating, and the plate installation each take several months and at the time of writing this dissertation, the new plates are still under construction.

Chapter 7. State Preparation

As described in Chapter 2, the first step in the measurement procedure is the state preparation in the magnetic sublevels of the hyperfine state. The precursor to the actual interferrometric measurement is a state preparation into the hyperfine ($F = 3$, $m_F = 0$) sublevel. This is accomplished by first optically pumping, followed by a sequence of microwave transitions performed in a magnetic bias field. In order to test the system while access to the measurement chamber was still possible, the state preparation of the atoms was tested before the end-caps were put on the magnetic shield. This allowed us to adjust the devices and optics in the measurement chamber, and to image the atoms on a CCD camera, which provides more information than the linear photodiode array.

7.1. Optical pumping

The optical pumping beam is overlapped with the vertical optical molasses beam for the measurement region. It enters the chamber from below. Before entering the chamber, the beams pass through a polarizing beam splitting cube.

Then the beam is split into two, one for the two cavities, and each is individually circularly polarized with a set of zero-order waveplates (i.e., a λ/2 and λ/4 for the beam for each cavity). The optical pumping beam is tuned to resonance on the $F = 4$ to $F' = 4$ hyperfine transition. Optically pumping to the dark state ($F = 4$, $m_F = -4$) minimizes the number of photons absorbed and the heating from the optical pumping pulse. The optical pumping pulse is 40 μs long with an intensity of 1 mW/cm^2. Our polarization is σ^-

with respect to the bias field, so after the optical pumping beam, the atoms will be pumped into the (4,-4) magnetic sublevel of the hyperfine state. This is achieved with fidelity of > 99.9%.

Because these beams are necessarily misaligned from the optical cavity beam, the axis for optical pumping is slightly off-vertical. For these tests, the optical pumping takes place in a bias magnetic field of ~20 mG. In order to align the magnetic field with the optical pumping, a low intensity long duration optical pumping beam is applied to the atoms and the bias magnetic field is adjusted until the heating from the optical pumping is minimized.

7.2. Microwave system

The second step in the state preparation is to transfer the atoms between the magnetic sublevels of the $F = 3$ and $F = 4$ ground state of the Cs atom. The main portion of the microwave frequency is generated by a synthesizer at 9.152 GHz (MITEQ SLFS-09.100-09.300-1M-10M). That frequency is mixed with a second frequency from a direct digital synthesizer (DDS). The DDS is based on the work of Schreck and Meyrath (2006), is programmable, and operates around 40 MHz. The DDS allows for tunable microwave frequencies as well as arbitrary frequency sweeps or pulses.

The signal is then amplified to a peak output power of 12 W (Microwave Amps AM53-9-9.4-40-40). An all copper microwave horn built by AINFO emits the microwaves into the measurement chamber. The horn is all copper to avoid materials that could possibly be magnetic, and it has been modified so that it fits into the clearance holes on the end-caps of the magnetic shields. Because the emitter of the microwave horn is stainless steel and a custom non-magnetic part is economically prohibitive, a long

copper waveguide is used to bring the microwave power into the magnetic shield when the shields are closed up.

7.3. Rabi oscillations

In order to verify that the microwave system is working and to characterize the amount of microwave power in the different polarizations at the two different lattice locations, Rabi-oscillations are observed between the $F = 4$ to $F = 3$ magnetic sublevels. First, the applied magnetic field, which defined the axis for the optical pumping, is adiabatically rotated over 10 ms to an axis that is favorable for the polarization of the microwave field produced by the horn. This axis is ultimately determined by the measurements of the Rabi frequencies.

First, we find the exact frequency of the (4,-4) to (3,-3) transition. The results of one such measurement are presented below in Figure 7-1. The microwave power at a single frequency is applied for 1 ms with ~1 W power. After the microwave pulse, the probe beam, tuned to the $F = 4$ to $F' = 5$ transition, measures the population of atoms that remains in the $F = 4$ ground state. The initial atom number is measured in a separate shot. For these measurements, the atom number was found by integrating the atomic signal on a CCD camera as shown in Figure 3-11. The frequency of the microwave is scanned to produce the graph.

These results show that the applied field is 33.3 mG at the negative lattice and 32.0 mG at the positive lattice location. The difference in magnetic field for the two locations comes from a combination of the residual magnetic field in the measurement region while it is still unshielded, and the fact the applied magnetic field may be non-uniform without corrections to the first order gradient.

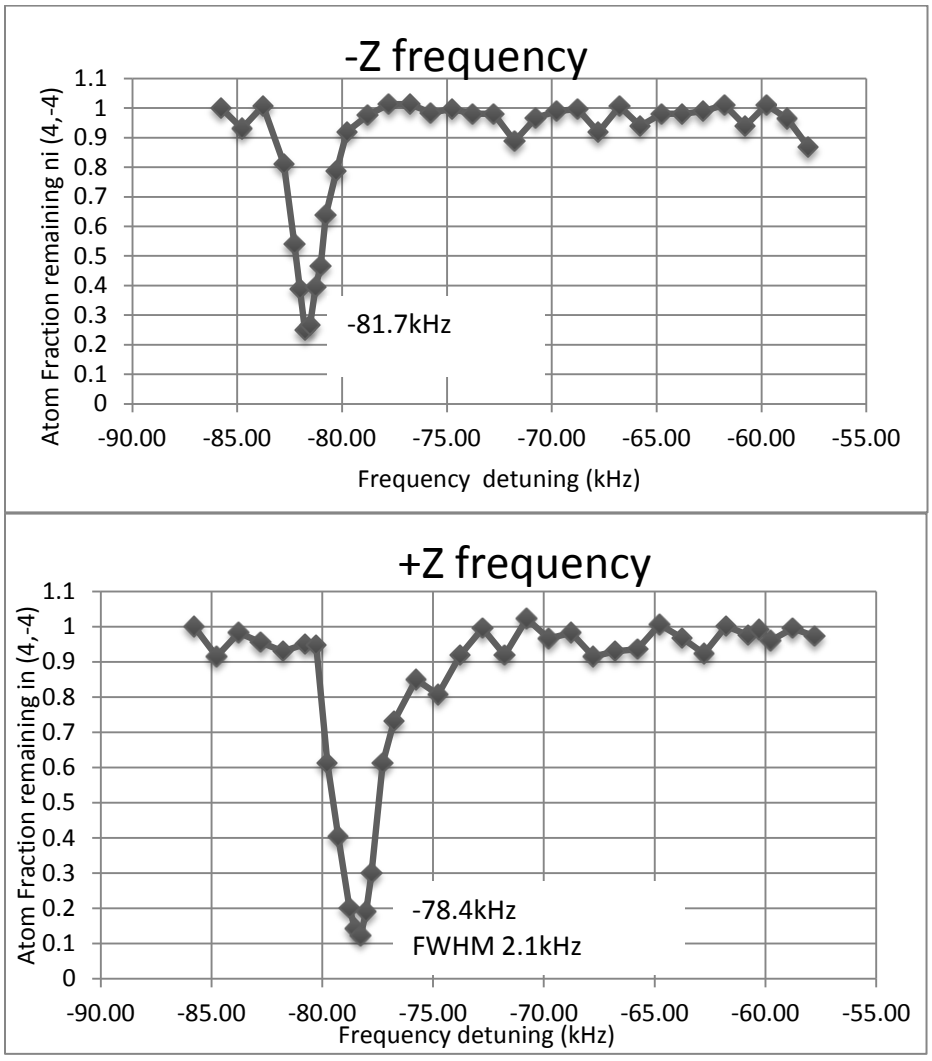

Figure 7-1. *Frequency of (4,-4) to (3,-3) transition*

The width of the transitions also suggests that there is some broadening. If we remember that we image a ~1 cm vertical spread of atoms, that the cavities are separated by 1 cm, and that there is a 3.2 kHz detuning between the transition at the two different lattice locations, it suggests at least some of the ~2 kHz width could come from a gradient in the magnetic field along the vertical direction, which will not be a problem when the shields are closed and the gradients are cancelled.

Next we measure the Rabi oscillations. The measurement procedure is similar to the one used above except that the microwave frequency is parked on resonance to the transition, the pulse time is 2 ms, and the amplitude of the pulse is scanned. The results for the two different cavities are shown below in Figure 7-2. For these graphs the amplitude is given as a fraction of the maximum power that we can apply with our system. In general, these results can change if the orientation or alignment of the microwave horn changes, and if the direction of the quantization axis changes.

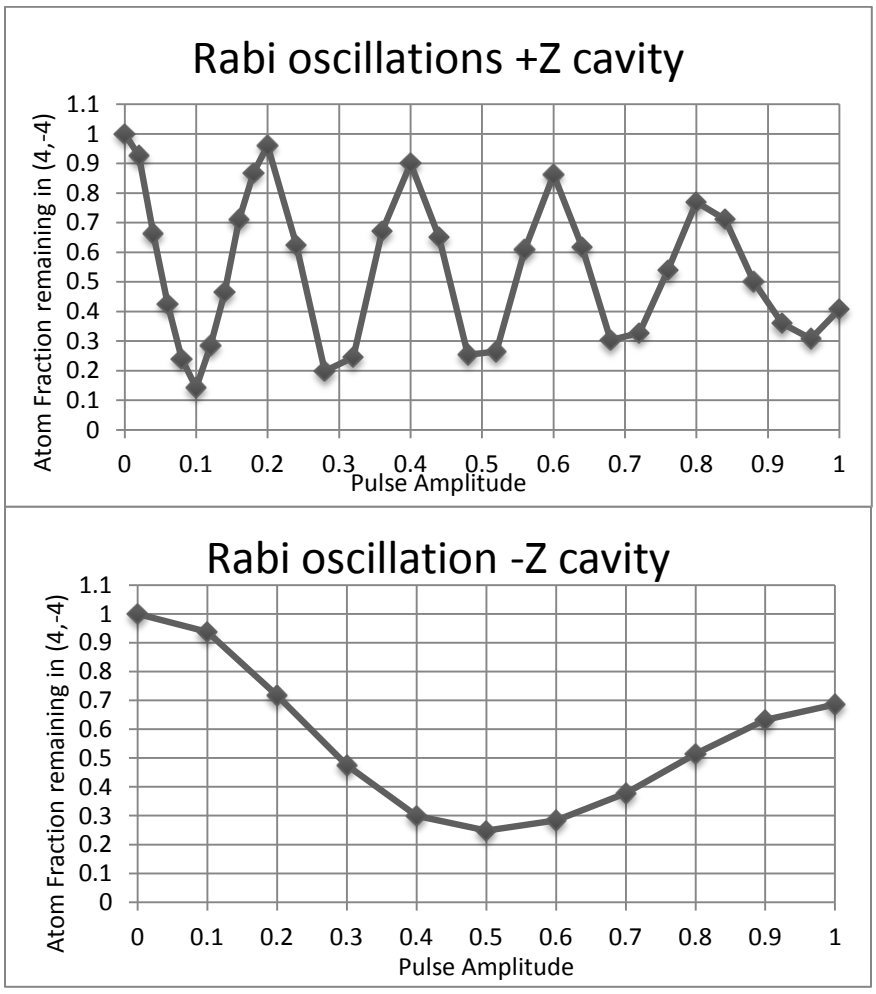

Figure 7-2. *Rabi oscillations of (4,-4) to (3,-3) transition*
The pulse amplitude is given as a fraction of the peak power we can apply (12 W).

A π-pulse is measured as the time and amplitude of the pulse required to transfer the atoms from the (4,-4) state to the (4,-3) state (i.e., the first minimums in graphs such as in Figure 7-2).

A π-pulse is defined by Equation (7.1).

$$0.42\,\Omega\,t = \pi \tag{7.1}$$

Where *t* is the time of a Blackman pulse, the 0.42 is a factor that takes into account the shape of a Blackman pulse as compared to a square wave, and Ω is the Rabi frequency of the transition. A Blackman pulse shape minimizes the frequency components away from the carrier frequency (Harris, 1968).

From these graphs we calculate the maximum possible Rabi frequency we can apply (i.e., an amplitude of 1) for a reasonable pulse length (which we set at 2 ms) in order to compare the power available for different transitions. The Rabi frequency scales linearly with the amplitude of the applied field. For example, in the +Z cavity of Figure 7-2 the π-pulse is achieved at an amplitude of 0.1. If the pulse duration is 2 ms, the Rabi frequency can be calculated from Equation (7.1) to be 595 Hz. The maximum amplitude of the microwave field gives a maximum Rabi frequency of 5.95 kHz.

The two graphs in Figure 7-2 show that there can be dramatically different microwave powers at the two different lattice locations even though they are separated only by 1 cm. This is because the surfaces of the plates and glass cell can reflect or partially reflect the microwaves, the glass can diffract the microwaves, and the optics in the measurement chamber can partially block the microwave beams. Because the power of the microwave goes as the amplitude squared, the power difference between the two cavity locations for this particular alignment of the horn at this particular polarization is a factor of 25. The horn's wide axis was initially aligned with the vertical distribution of the atoms, however, the polarization of the magnetic field is in the x-z

plane for this orientation, which can exacerbate interference effects. This suggested that rotating the horn by 90 degrees could improve the imbalance.

Using measurements such as these on three different transitions, we can assess the ability to do any microwave transition at the two different lattice locations. Specifically, for a given quantization axis and horn orientation we determine the microwave power projected onto the three polarizations, σ^-, σ^+, and π. We measure the three transitions shown in half of the magnetic sublevel manifolds shown in Figure 7-3. The remaining factors that contribute to the Rabi frequency for any other transition are given by the Clebsch-Gordon coefficients.

.

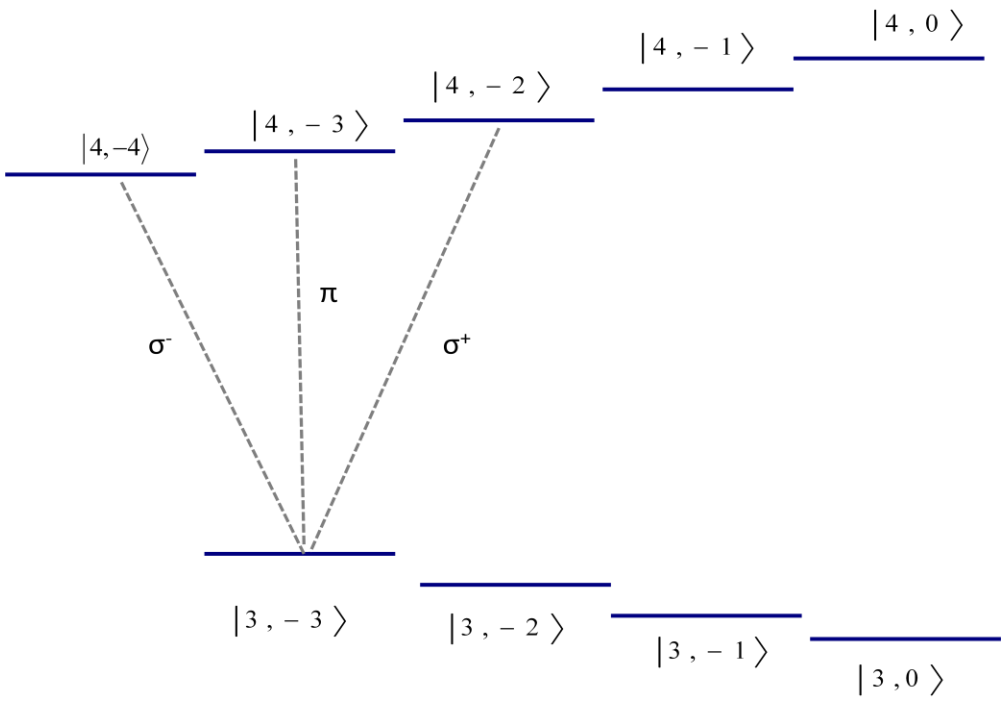

Figure 7-3. *Three microwave polarizations*

The results for these three transitions for the two cavity locations for the rotated horn and a quantization axis in the y direction are summarized in Table 7-1.

Transition	Polarization	Ω_{max} +Z	Ω_{max} -Z
(4,-4) to (3,-3)	σ^-	19.8 kHz	8.5 kHz
(3,-3) to (4,-3)	π	1.5 kHz	3 kHz
(3,-3) to (4,-2)	σ^+	2.4 kHz	1.2 kHz

Table 7-1. *Summary of Rabi frequencies for three polarizations*

The Rabi-frequency for the two different lattice locations is never more than a factor of two different, as compared to a factor of five previously. There can also be significantly different Rabi frequencies for the different polarizations at the same location. Because we primarily use the π and σ^- transitions for state preparation, and because the σ^+ transition is twice as detuned from the σ^-, the ratio that limits us here is the 19.8/1.5 = 13.2. Using sets of measurements such as these, we find a horn orientation and alignment as well as a quantization axis that gives smaller ratios of the measured Rabi frequencies. However, in order to fully understand the best distribution of microwave power, we must first understand exactly what we want to do with the microwaves. The problem with having such dramatically different Rabi frequencies turns out to involve off-resonant transitions during the multiple adiabatic rapid transit transitions described in the following sections.

7.4. Adiabatic rapid passage

It is well known that a more robust state transfer can be achieved using adiabatic rapid passage (ARP) rather than a π-pulse. Adiabatic rapid passage is accomplished by starting with a frequency that is detuned from the transition. The frequency is then swept through resonance such that on the Bloch sphere, the torque vector sweeps from the ground state to the excited state. As long as the frequency sweep is done slowly

enough, the state vector, initially in the ground state, will tightly circle the torque vector and follow it up to the excited state. ARP is robust to inhomogeneous broadening and is insensitive to the actual power of the pulse, as long as it is large enough.

The results of an adiabatic rapid passage transfer between the (4,-4) and (3,-3) state is shown in Figure 7-4. For this pulse, the total time was 2 ms, the frequency was swept from -2.5 kHz to +2.5 kHz, and the peak amplitude of the microwave was 0.3.

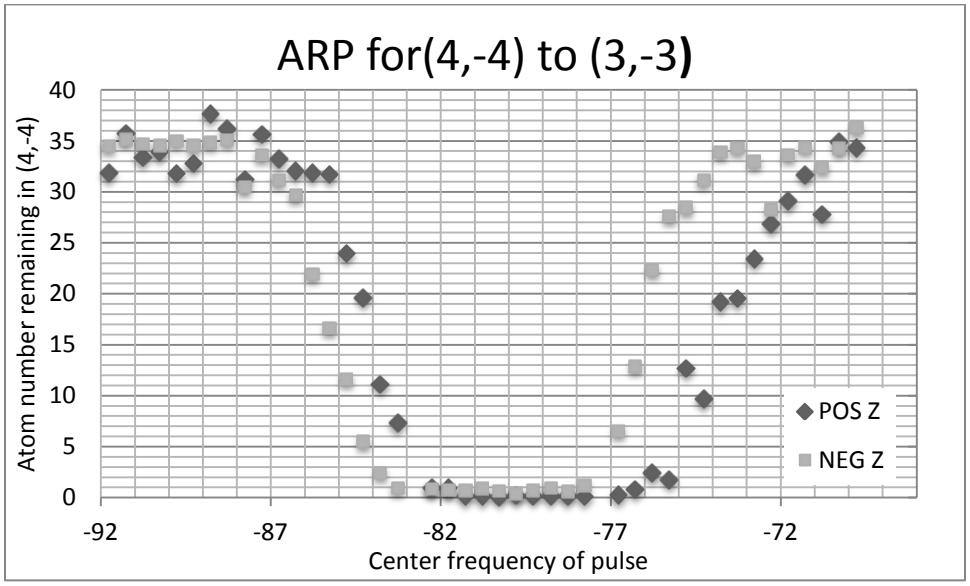

Figure 7-4. *ARP as a function of frequency*

The flat bottom of the shape in Figure 7-4 demonstrates that the transfer can be done effectively even if the transitions for the two lattices have different frequencies. In addition, the ARP transfer is shown as a function of the pulse amplitude for four different pulse times in Figure 7-5. The flatness as the pulse amplitude increases demonstrates the insensitivity of the ARP to the amplitude.

It is necessary to keep the frequency sweep large enough so that the torque vector starts sufficiently close to the ground state. At the same time it is necessary to keep the frequency sweep small and not over-drive it so that the microwaves do not

cause transitions on the detuned microwave transitions which, for this bias magnetic field, are only separated by 11 kHz. When the frequency sweep, amplitude, and time are experimentally optimized, a single transition can be performed with fidelity as high as 99.8%.

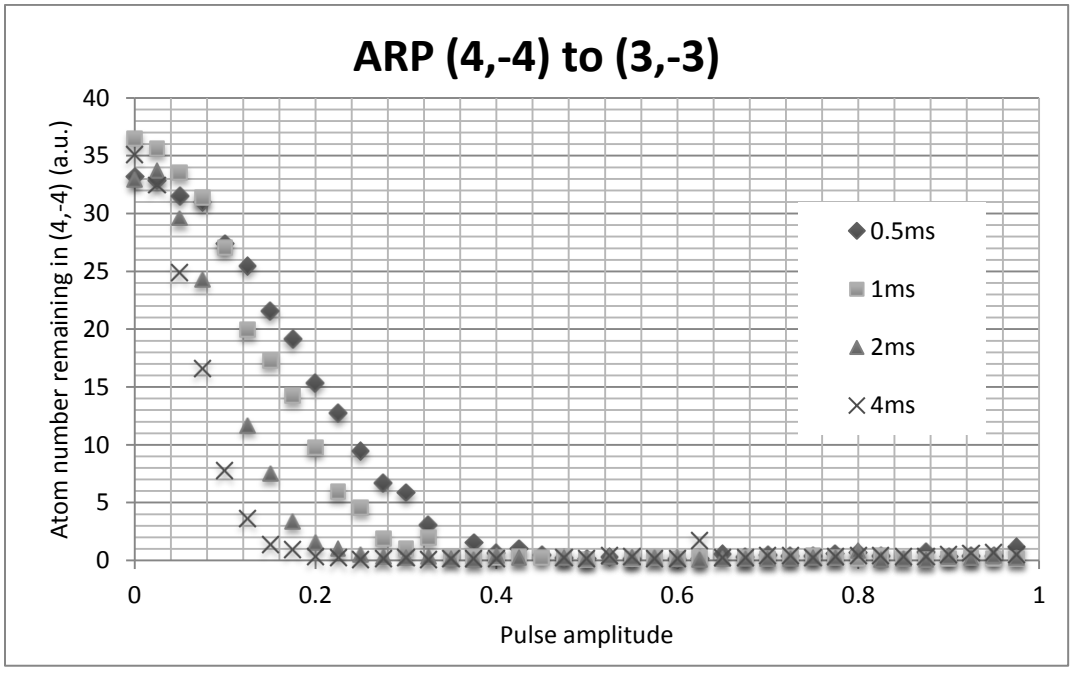

Figure 7-5. *ARP as a function of amplitude*

7.5. Multiple ARP transfers

As has been described, we ultimately want to prepare the atoms in the (3,0) state. This can be accomplished with 5 ARP pulses. Such a path is shown in Figure 7-6. The numbers next to the transitions are the Clebsch-Gordon coefficients squared (i.e., the transition strength).

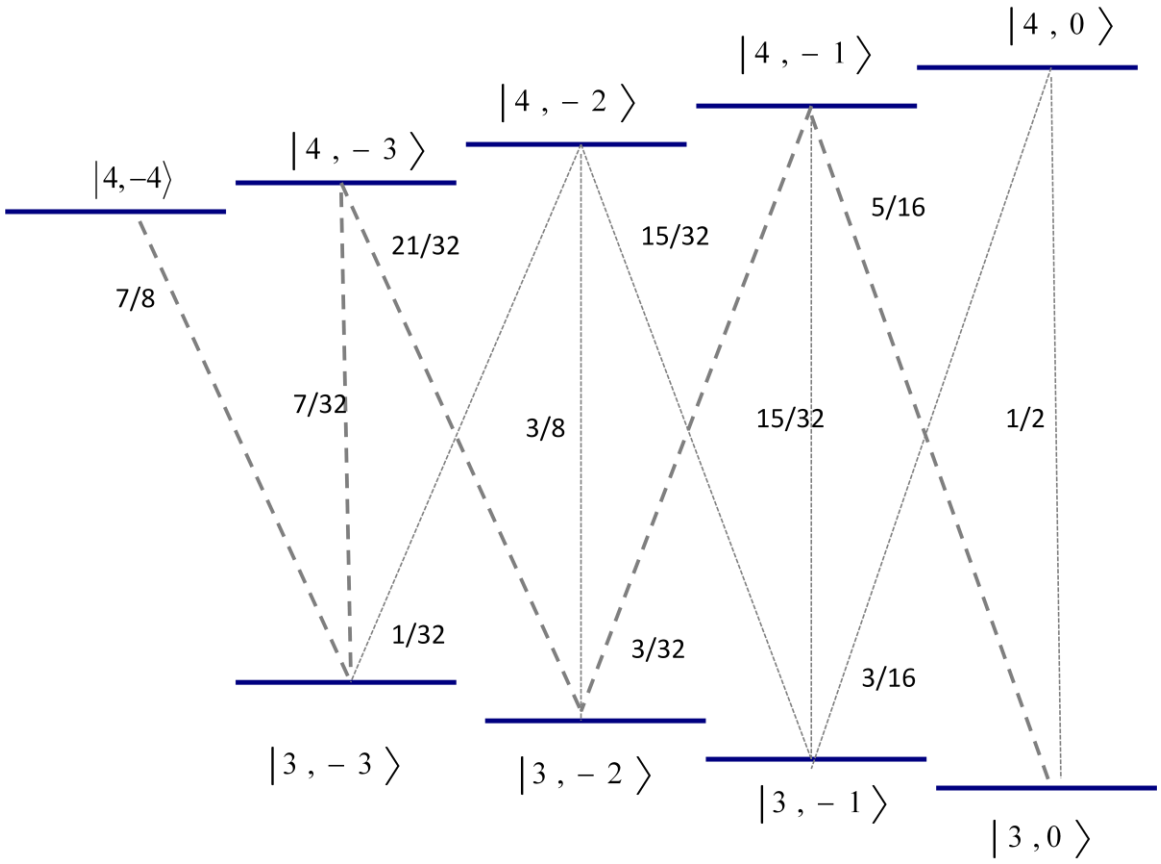

Figure 7-6. *Multiple ARP transfers to (3,0)*

The dashed line is one possible path to take through the magnetic sublevels. Using the quantization axis described above, the five transition sequence to the (0,0) state could only achieve a fidelity of ~95%. It is possible that another path through the microwave manifold would be more favorable.

In particular, it seems advantageous to avoid the small matrix element of the (3,-3) to (4,-2) transition. However, the problem becomes clearer when the results of measurements such as those in Table 7-1 are convolved with Figure 7-6. The transition strengths at each cavity location can be scaled for the measured microwave power in each polarization. In order to avoid the factor of 13.2 ratio in adjacent transition

strengths, the quantization axis was changed to be 45 degrees off of the vertical in the x-y plane and the result is shown in Figure 7-7.

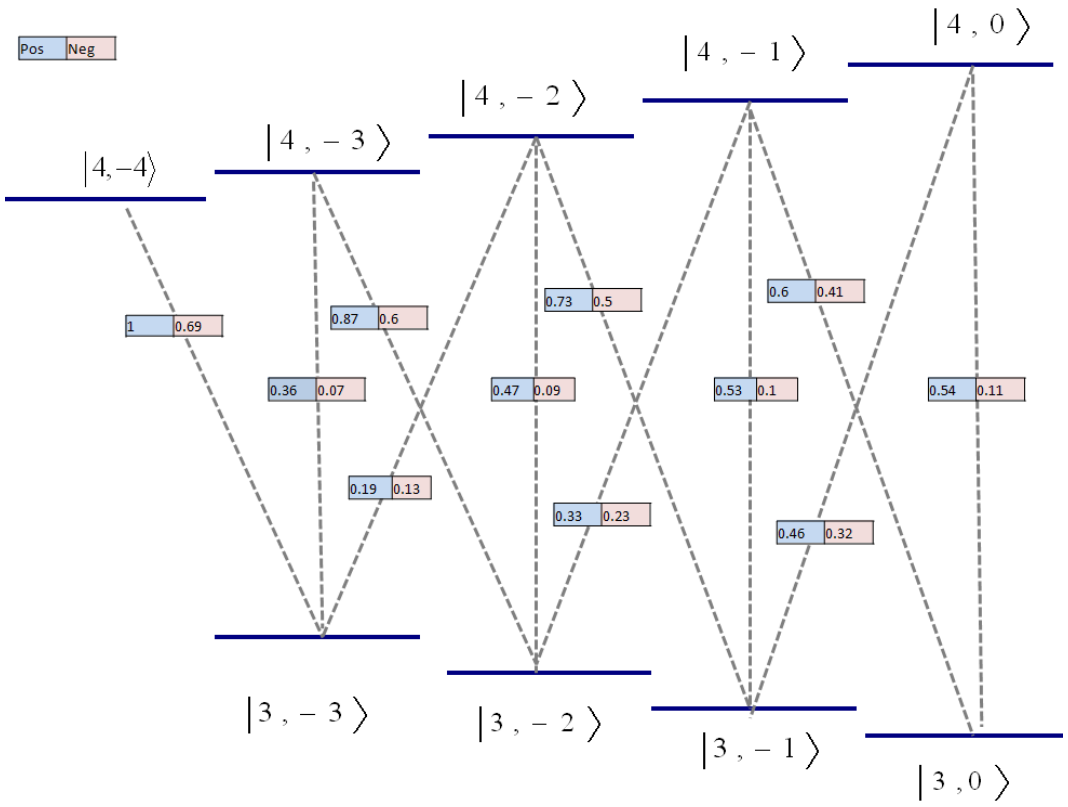

Figure 7-7. *Transitions strengths including polarizations and cavity location*

This analysis reveals a number of things. First of all, the fact that different polarizations can have dramatically different powers can outweigh the benefits of avoiding transitions with unfavorable Clebsch-Gordon coefficients. Note, for example, the (3,-3) to (4,-3) transition for the -z lattice. This Rabi frequency is so small that it must be driven very hard in order to make the transition. Because there are nearby transitions with much larger Rabi frequencies, i.e., the (4,-4) to (3,-3) +z transition, driving this transition will drive significant off resonant excitations that can limit the fidelity. If one

were to convolve Table 7-1 and Figure 7-6, the resulting figure would look much less favorable than Figure 7-7 because of the large ratios between Rabi frequencies.

When the magnetic shields were installed, the microwave horn had a slightly different alignment, and the measured Rabi frequencies are given in Table 7-2. The potentially limiting ratio of Rabi-frequencies is only 13.2/3.3 = 4. Using this quantization axis, the five transition fidelity could be > 98%.

Transition	Polarization	Ω_{max} +Z	Ω_{max} -Z
(4,-4) to (3,-3)	σ^-	13.2 kHz	10.8 kHz
(3,-3) to (4,-3)	π	8.5 kHz	3.3 kHz
(3,-3) to (4,-2)	σ^+	1.2 kHz	2.4 kHz

Table 7-2. *Rabi frequencies for three polarizations in new setup*

Chapter 8. Noise and Systematic Effects

In this chapter we will discuss the noise and systematic effects that can affect the measurement. For the sake of completeness we will discuss the major effects and how our experiment meets them, but in many cases, detailed calculations were already performed by Fang (2007, pp. 30-45). When this is the case, we shall not repeat the calculations but will refer to that work.

The signal is ultimately a fraction of atoms returning to the $m_F = 0$ state (see Chapter 2). Though the signal from the full seven level system will be more complicated, we can visualize the effects that noise will have on the signal if we consider a simplified picture of a three level interferometer. In the three level system, the probability of any given atom returning to the $m_f = 0$ state, P, is given by Equation (8.1).

$$P = \mathrm{Cos}^2\left((\mu \mathrm{B} + \mathrm{dE})\frac{\tau}{\hbar}\right) \tag{8.1}$$

The phase accumulated, $\varphi = (\mu B + dE)\tau/\hbar$, depends on the magnetic moment, μ, the magnetic field, B, the EDM of the atom, d, the electric field E, the measurement time, τ, and Planck's constant. Though Equation (8.1) is simplified, it is intuitively satisfying in that if there is no phase accumulation between the two components of the superposition of $m_F = 3$ and $m_F = -3$, the probability of retuning to $m_F = 0$ will be 1. Similarly, if the phase accumulation between the two components is exactly π the probability will be 0. If the measurement of Equation (8.1) is done many times in parallel (i.e., with many atoms), it can also be interpreted as a fractional population of atoms returning to $m_F = 0$. Noise on the phase and noise on the population can have different effects on the measurement.

8.1. Insensitivity to noise with simultaneous interferometers

Our experiment has been designed specifically to be insensitive to particular types of noise. A differential measurement of two interferometers simultaneously allows for the cancellation of common mode noises (Fixler *et al.*, 2007). As long as a noise source is common mode, even if it is larger than an entire fringe, the phase difference between the two interferometers can still be extracted. In essence, the sinusoidal shapes of two interferometers will parametrically produce an ellipse. That ellipse can be fitted to extract the phase difference (Foster *et al.*, 2002).

Figure 8-1 shows a simulation of the populations of three perfect interferometers. The phase is shifted from the first interferometer by π/10 and π/25 for the second and third interferometers respectively. The second and third interferometers are compared to the first on the right side of the figure. The phase difference can be extracted from the ellipse. Two interferometers with the exact same phase parametrically form a line with slope 1. Two interferometers exactly π out of phase form a line with slope -1. As we will see, this type of analysis is inherently insensitive to some types of noise.

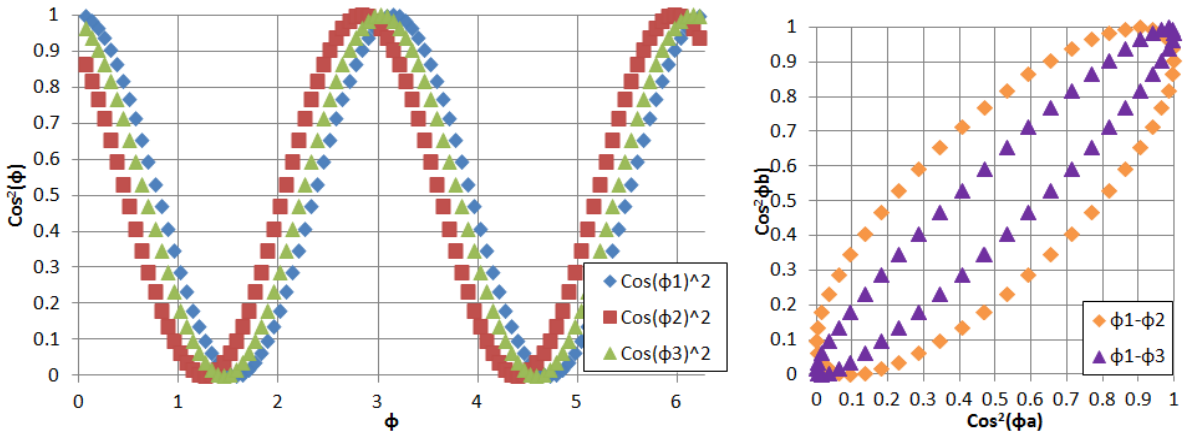

Figure 8-1. *Phase shift between two interferometers*

Graphically, we can see how a noise on the phase of the interferometer affects graphs like those in Figure 8-1. In Figure 8-2 (a) we simulate common mode phase noise by adding the same random phase noise with a π/25 amplitude to each of the interferometers. This effectively adds a random horizontal shift to each point in the fringe. Even though the fringe is significantly noisier, the ability to fit to the ellipse is not compromised. If the phase noise has an amplitude of π, (b), the fringe will be completely washed out. But as long as the noise is common mode it still does not compromise the ability to fit the ellipse.

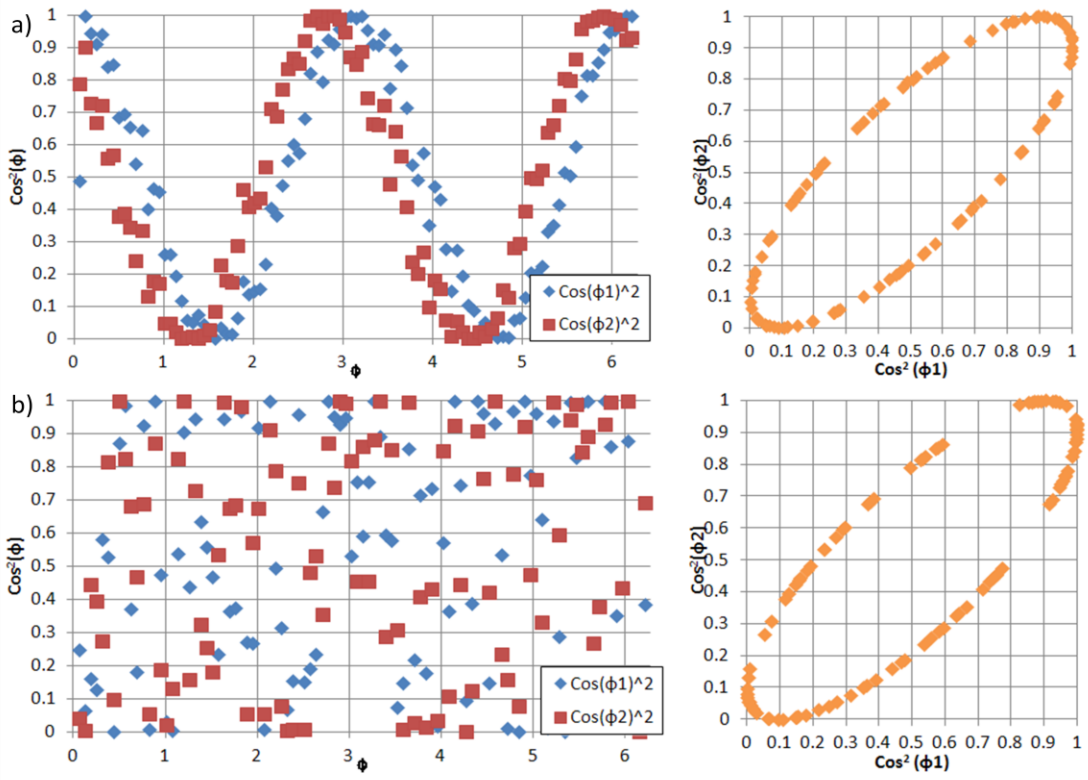

Figure 8-2. *Common mode phase noise*

a) Common mode phase noise with an amplitude of π/20, b) common mode phase noise with an amplitude of π. In either case, the parametrically formed ellipse is not compromised.

The other type of noise is one that adds a random vertical shift, rather than a horizontal one. This comes from any type of noise in the population of the atoms, or in our ability to measure the population of the atoms. Though we will have the ability to normalize the population by measuring the total atom number in the shot, there could be some noise in how well we can normalize the population. In Figure 8-3 we add a random noise to the population of the fringes with an amplitude of 20% of the peak amplitude. As we will see in the following section, this is an overestimate of how much population noise we expect, but it is used as a demonstration of how this type of noise affects the signal. In case (a) the noise is common mode, and in (b) it is not. In both cases, the fringe looks qualitatively the same as that in Figure 8-2 (a), but the parametrically drawn ellipse is different. Common mode noise is only partially cancelled, particularly near the center of the fringe (i.e., population near 0.5). But even in the case of uncorrelated noise, the ellipse can still be fit with statistical methods.

If uncorrelated phase noise is added to the interferometers, the resulting graphs will look qualitatively similar to Figure 8-3 (b). Also, if common mode phase noise is added in addition to the population, the addition of population noise does not compromise the ability to cancel the common mode phase noise. If the contrast of the fringes is reduced, they still parametrically produce an ellipse, albeit a smaller one.

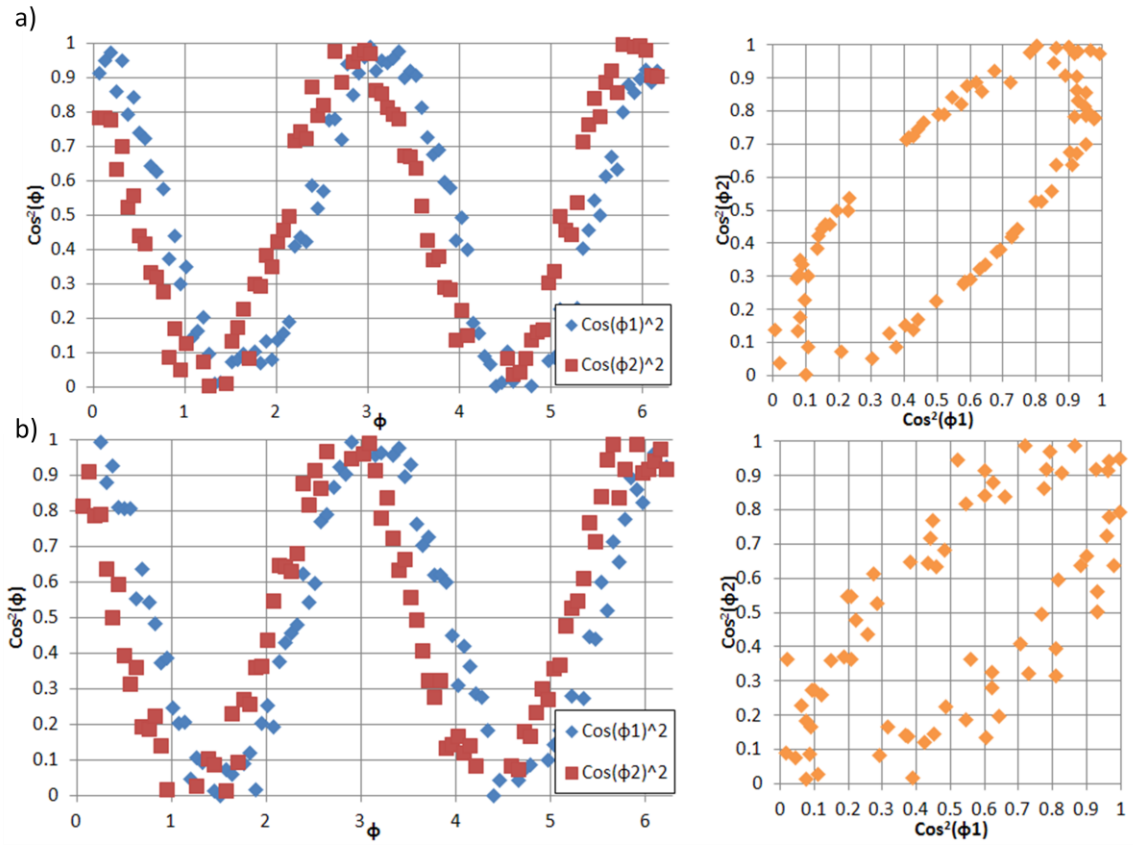

Figure 8-3. *Population noise*

a) Common mode population noise with an amplitude of 20% of the total, b) uncorrelated population noise with an amplitude of 20% of the total.

The ability to determine the phase difference between two fringes depends on how well the ellipse can be fit. Common mode phase noise does not compromise the measurement at all. Population noise, even if common mode, can have some effect on the ability to fit the ellipse, but only if it is a type of population noise that cannot be normalized by a measurement of the total atom number.

Our experiment in fact has two built in simultaneous interferometers. The first pair is the two optical cavities, which give simultaneous measurements of the atoms in both positive and negative E fields. This ensures that if there is a uniform bias B field, $\delta B(t)$, which is the same for the two lattice locations, it will be cancelled out in a

differential measurement, even if it is different from one shot to the next. The second pair of interferometers is the ability to measure the atoms in a positive and negative E field at the same lattice location on two subsequent shots, i.e., with the voltage on the center plate reversed. This means that any B field gradient, *ΔB(z),* will be cancelled in the differential measurement as long as it does not change from one shot to the next. The final possibility is a magnetic field gradient that changes from one shot to the next, *δΔB(z,t).*

This can be seen symbolically in Equation (8.2). The numerical subscripts on the phases represent either the first or second shot, i.e., with a positive or negative voltage on the center electric field plate. The + and – subscripts represent either the +z or –z lattice locations.

$$\varphi_1^+ = \left(+\mathrm{dE} - \mu\frac{\delta\mathrm{B(t)}}{2} + \mu\frac{\Delta\mathrm{B(z)}}{2} + \mu\frac{\delta\Delta\mathrm{B(z,t)}}{2}\right)\frac{\tau}{\hbar} \tag{8.2}$$

$$\varphi_1^- = \left(-\mathrm{dE} - \mu\frac{\delta\mathrm{B(t)}}{2} - \mu\frac{\Delta\mathrm{B(z)}}{2} - \mu\frac{\delta\Delta\mathrm{B(z,t)}}{2}\right)\frac{\tau}{\hbar}$$

$$\varphi_2^+ = \left(-\mathrm{dE} + \mu\frac{\delta\mathrm{B(t)}}{2} + \mu\frac{\Delta\mathrm{B(z)}}{2} - \mu\frac{\delta\Delta\mathrm{B(z,t)}}{2}\right)\frac{\tau}{\hbar}$$

$$\varphi_2^- = \left(+\mathrm{dE} + \mu\frac{\delta\mathrm{B(t)}}{2} - \mu\frac{\Delta\mathrm{B(z)}}{2} + \mu\frac{\delta\Delta\mathrm{B(z,t)}}{2}\right)\frac{\tau}{\hbar}$$

$$(\varphi_1^+ - \varphi_1^-) - (\varphi_2^+ - \varphi_2^-) = 4\,dE\frac{\tau}{\hbar} + 2\mu\,\delta\Delta\mathrm{B(z,t)}$$

We see that a magnetic field gradient that changes as a function of time is not cancelled out by the measurement procedure.

8.2. Shot noise limit and systematic sensitivity

Shot noise is the noise associated with the random aspect of a quantum measurement (Beenakker and Schönenberger, 2003). A single measurement gives only one result out of the possible outcomes, but if the measurement is repeated many times the initial state can be reconstructed. The uncertainty of determining that initial state can be lessened by accumulating more measurements. The shot noise level is the uncertainty in the final measurement imposed by quantum counting statistics (Itano, *et al.*, 1993). In principle, the measurement cannot be better than the limits imposed by these counting statistics, unless a fancy squeezing technique is used. Therefore, the shot noise limit is the limit against other sources of noise are measured. If a given source of possible error is smaller than the final shot noise limit, it will not detract from the overall sensitivity.

If we perform a differential measurement and subtract the probability in the two different cavities, they would have nominally the same magnetic field and only the electric field would have the opposite sign. The resulting difference, after some algebra, and applying the small angle approximation on the term with the EDM is given in Equation (8.3):

$$\Delta P \approx 2\mathrm{dE}\frac{\tau}{\hbar}\mathrm{Sin}\left(\mu\mathrm{B}\frac{\tau}{\hbar}\right) \tag{8.3}$$

The term in the phase, $\varphi \approx \mu B\frac{\tau}{\hbar}$, is much larger than the term with the EDM, and the probability of measuring a state in $m_F = 0$ is proportional to $\mathrm{Cos}^2\varphi$. The probability of *not* returning to $m_F = 0$ will be proportional to $\mathrm{Sin}^2\varphi$.

The standard deviation of any probabilistic measurement, σ, is given by Equation (8.4):

$$\sigma^2 = \left(\sum_{\mathrm{i}} (\mathrm{X_i} - \langle \mathrm{X} \rangle)^2\right) \tag{8.4}$$

Where the X_i are the possible results of the measurement, i.e., 1 if the result is m_F = 0 and 0 if the result of the measurement is that the atom stayed in the superposition state. The average of the measurement will be the probability of each result multiplied by the result of the measurement (i.e., 0 or 1). The average result, $\langle X \rangle$, of the measurement of Equation (8.3) is $\mathrm{Cos}^2\varphi$, again using the small angle approximation. After expanding and simplifying, Equation (8.4) looks like this:

$$\sigma^2 = \left(1 - \mathrm{Cos}^2(\varphi)\right)^2 \mathrm{Cos}^2(\varphi) + \left(-\mathrm{Cos}^2(\varphi)\right)^2 \mathrm{Sin}^2(\varphi) \tag{8.5}$$

$$\sigma = Sin\,(\varphi)\,Cos\,(\varphi)$$

The standard error of the mean, *SEM*, is given by Equation (8.6).

$$SEM = \frac{\sigma}{\sqrt{\mathrm{N}}} = \frac{Sin\,(\varphi)\,Cos\,(\varphi)}{\sqrt{\mathrm{N}}} \tag{8.6}$$

Where *N* is the total number of measurements. If the probability in Equation (8.3) is measured *N* times, it can only be determined as accurately as the *SEM*. Equating Equations (8.3) and (8.6) and a little algebra gives us an expression for the smallest measurable atomic EDM:

$$d_s = \frac{\hbar}{4\tau \mathrm{E}\sqrt{\mathrm{N}}} \tag{8.7}$$

Where we have used the identity $\mathrm{Sin}(\varphi)\mathrm{Cos}(\varphi)/\mathrm{Sin}(2\varphi) = 1/2$. The subscript ‘s’ in d_s signifies that it is the smallest possible measurement, i.e., the systematic sensitivity. It is important to note that this could be different by a numerical factor depending on the exact nature of the probability in the measurement procedure, but the experimental parameters largely determine the shot noise limit. The total number of measurements, *N,* is the total number of atoms measured. If we wish to know the ultimate sensitivity of the

experiment, we can break this down into more experimentally useful quantities. In this case, N is given by the number of atoms in each shot, n, multiplied by the number of shots. The number of shots can be expressed as the total amount of time the experiment is run, T, multiplied by the experimental duty cycle, D, divided by the measurement time, τ. The duty cycle is the fraction of the time during running the experiment that actually contributes to the free evolution time, taking into account the overhead time, i.e., the time taken for loading the atoms into the measurement chamber and performing the state preparation.

The sensitivity to the electron EDM is found by using the relationship $d_s = d_{es}Rmg$, where g is the Landé g-factor, R is the enhancement factor, and m is the magnetic quantum number at which the measurement takes place. To obtain the ultimate systematic sensitivity of the experiment, we expand Equation (8.7) with the substitutions for the total number of atoms and for the electron EDM:

$$d_{es} = \frac{\hbar}{4\mathrm{ERmg}\sqrt{\mathrm{nTD}\tau}} \tag{8.8}$$

A useful way to express the shot noise limit is the frequency shift that an electron EDM of that size would produce. The frequency shift is given by d_{es} multiplied by $ERmg/\hbar$. This way, other effects that shift the frequency of the transition during the measurement can be compared easily. Because magnetic fields are frequently a potential problem for us, we also care about what size of a magnetic field will produce this frequency shift. This is found by comparing the frequency shift to that from a magnetic field ($\hbar\omega = \mu B = 2gm\mu_B B$), where μ_B is the Bohr magneton. In Table 8-1, the systematic sensitivity and shot noise per shot limits are summarized in terms of the sensitivity in e-cm, Hz, and gauss (G).

If a noise effect is not correlated with the reversal of the electric field, (e.g., if it is random from one shot to the next or if it is a slow drift), as long as this noise source isn't larger than the shot noise of one shot of atoms, then it will average out over many shots. For that case we would use the number of atoms in each shot, *n,* in Equation (8.7) instead of the total number of atoms measured throughout the entire experiment (*N)*. The smaller atom number contributing to the statistical uncertainty results in a much less stringent requirement for the noise sources. If the noise on the population is not accounted for by normalization, it is appropriate to compare it to the shot noise per shot.

For Table 8-1 we use the following set of values; E = 60 kV/4 mm = 150 kV/cm, R = 120.5, g = 1/4, m_f = 3, D = .5, T = 24 hours, τ = 3 seconds, and $n = 2*10^8$. The value $2.5*10^{-30}$ e-cm is the ultimate systematic sensitivity of the experiment. This is a possible improvement by a factor of ~400 over the current experimental limit assuming that all sources of noise and systematic errors can be kept below the shot noise level.

	Systematic sensitivity	Shot noise per shot
d (e-cm)	$2.5*10^{-30}$	$3*10^{-28}$
ω/(2π) (Hz)	$5*10^{-8}$	$6*10^{-6}$
B (G)	$2.5*10^{-14}$	$3*10^{-12}$

Table 8-1. *Shot noise limits*

8.3. Sources of noise

8.3.1. Noise on the atom number and detection system

Noise on the atom number could come from fluctuations in the loss from collisions with the background gas or fluctuations in atom number from shot to shot (coming from any number of fluctuations in the atom collection and preparation system

described in 0). However, both of these can be normalized by measuring the total number of atoms in each shot. This could be done after the measurement free evolution time by adding all of the contributions from the individual m_F levels in the final state spectroscopy. This noise reduces to noise in the detection system.

The vacuum limited lifetime of 6 seconds should be long enough to ensure that the fringe contrast is not lost from atoms loss during the measurement time. As long as the vacuum is relatively stable, the fluctuation in this atom number will be small. The shot to shot noise on the atom number measured on our apparatus can be as high as 20 to 30%, but the uncertainty on that number is only limited by our ability to measure the number of total atoms in each shot.

Fluctuations in the detection system could come from fluctuations in the probe laser frequency or intensity, misalignments in the collection optics, or because of dark currents on the linear photo-diode array. Because both probe beams for each cavity derive from the same laser, some of this will be common mode noise and its effects will be partially mitigated. For the collection optics, because the atom cloud has a width of 580 μm and the photodiodes are 3.2 by 4.7 mm, we do not require a high degree of spatial resolution, and fluctuations in the collection efficiency are not likely to cause a problem. Even so, an upgrade of the collection optics is currently being undertaken which will hopefully obtain better spatial resolution and therefore more stability. In addition, we specifically designed a photodiode and amplifier system with low noise and we expect to have a $3.7*10^3$ signal to noise ratio (Zhu, Solmeyer, and Weiss 2012; Zhu, *forthcoming*).

8.3.2. Scattering from the trapping light

Types of noise that de-phase the m_F level of the atoms at any point during the measurement procedure will essentially be a noise on the atom number with a reduced fringe contrast. If the atoms scatter photons from the trapping light they will decohere and will not contribute to the measurement. The scattering rate, $\Gamma_{s,}$ is given by:

$$\Gamma_s = \sum \frac{\mathrm{I}}{\mathrm{I_s}} \frac{{\Gamma_0}^2}{8\delta^2} \tag{8.9}$$

Where I, $I_{s,}$ Γ_0, and δ are the intensity, saturation intensity, natural lifetime, and detuning of the relevant atomic transitions which are summed. For Cs, the D_1 and D_2 lines give a scattering rate of 0.1 s^{-1} for a 10 μK trap depth. We can load the atoms into the trap with a larger trap depth, but for the measurement we can lower it to 10 μK to minimize sources of noise and systematic errors.

The noise on the fringe contrast will be a fraction of this depending on the intensity fluctuations of the cavity in the timescale of the measurement time. Currently the intensity fluctuations of the cavity have an amplitude of about 1%, but the drift of the average intensity over the measurement time will be much less than this. The intensity noise of the cavity is uncorrelated between the two cavities.

8.3.3. State preparation noise and the AC-tensor stark shift

If there is noise in the state preparation or readout system, the atoms will effectively be lost to the measurement and add population noise and a lowered fringe contrast. One possibility is noise in the microwave state preparation. Such a noise could come from fluctuations in the level of microwave power or frequency, or from shifts in the transition frequencies. Noise associated with the output of the microwave system would

be largely common mode noise and would not contribute greatly to noise in the atom number because ARP transfers are robust against fluctuations in the microwave power and frequency.

The low B-field transitions are potentially compromised by nose on the transition frequency. This could come from noise in the AC-tensor or AC-vector stark shift. The AC-tensor stark shift has the form (Romalis and Fortson, 1999):

$$\Delta\nu_t = \nu_t(3\mathrm{Cos}^2(\varphi_\mathrm{T}) - 1)\mathrm{m_f}^2 \tag{8.10}$$

Where ν_t is a constant that depends on the hyperfine level and the frequency of the trapping light and is ~.03 Hz for Cs in a 10 μK trap. φ_T is 0 because it is the angle that the polarization of the trapping light makes with the quantization axis, i.e., the direction of the DC-E field. This gives a shift of the (3, 3) level of 1 Hz. The noise because of this shift will depend linearly on the intensity fluctuations of the cavity and will depend on how much change this produces in the fidelity of the low frequency B field transitions.

8.3.4. AC-vector stark shift

Another type of noise that can affect the measurement is a frequency shift that is proportional to m_F. This noise could come from two sources: the AC-vector stark shift or a magnetic field. If a vector shift, i.e., a shift that is proportional to m_F, is oriented in the x or y direction, it will primarily effect the noise in the state preparation and readout because, if it were big enough, it would tend to mix the m_F levels in the z direction. Noise from a vector shift in the z-direction will not reduce the contrast of the fringe, but will directly shift the phase of the measurement (i.e., the type of noise described in Figure 8-2). The AC-vector stark shift is given by (Romalis and Fortson, 1999):

$$\Delta\nu_v = \nu_{vt}(|\varepsilon_\mathrm{L}|^2 - |\varepsilon_\mathrm{R}|^2)\mathrm{m_f}\,\mathrm{Cos}(\theta) \tag{8.11}$$

Where in this case v_{vt} is $4*10^3$ for a 10 μK trap. The ε_L and ε_R are the components of left and right circular polarization in the trapping light, whose difference would be 0 for perfectly linearly polarized light. Because the circular polarization acts on the m_F linearly, it is often interpreted as a fictitious magnetic field. θ is the angle that the k vector of the trapping light makes with the quantization axis.

If we assume we can make the polarization linear to the extent that the prefactor depending on polarization is 10^{-3} and we can align the cavity with respect to the E field to better than 10^{-3}, this gives a frequency shift of the (3,3) level of $1.2*10^{-2}$ Hz. The k vector is largely in the y direction and partially in the z direction, by a factor of ~.005. To the extent that this produces a linear shift in the m_F levels in the z direction, it can alter the phase of the interferometer and should be compared to the shot noise per shot. Including the reduction from the projection onto the z direction, if the noise on the trapping light intensity is better than 10^{-2} the noise will be $6*10^{-7}$ Hz, which is smaller than the shot noise per shot ($6*10^{-6}$ Hz). Currently, our control over the polarization in the cavity is not this good, but the undertaking to optimize the polarization in the cavities will hopefully correct this deficit. The part of this vector shift that is in the y direction will be less of a problem for the reasons discussed above.

If there is noise in the state preparation, a collisional frequency shift could also contribute to the noise of the measurement. Based on the calculations of Bijlsma, Verhaar, and Heinzen (1994), as long as we have < 2% fluctuation in the difference in the population between the m_F = +3 and the m_F = -3 states when the superposition is prepared, the noise coming from the collisional frequency shift will be less than the shot noise (Fang, 2007).

8.3.5. Johnson noise

Fluctuating magnetic fields can come from several things, such as residual ambient fields leaking through the magnetic shields, residual magnetization of the magnetic shields, or Johnson noise in any conducting material near the measurement chamber. All of these will presumably be uncorrelated with the switching of the E field and to the extent that they are in the z direction, different for the two cavities, and different from one shot to the next, they should be compared directly to the shot noise per shot of 3 pG. If it is difficult to estimate the field gradient from an effect or it's stability in time, if the effect is smaller than the shot noise for the size of the magnetic field itself, it will not be a problem.

One source of magnetic fields that change rapidly and can potentially be close to the atoms are those created by Johnson noise (Lamoreaux, 1999). Johnson noise is the magnetic field noise created by electrons jiggling in a conductor. This is the motivation behind keeping good conductors away from the atoms in the measurement chamber. In order to calculate the Johnson noise of an arbitrarily shaped object we first note that the root mean squared value of the current dipole noise, i^2, in a given frequency spread, δf, and in a given volume, dV, will be given by the Nyquist theorem as (Nyquist, 1928; Varpula and Poutanen, 1983):

$$i^2 = 4\,\mathrm{k_B T}\,\sigma\,\delta\mathrm{f}\,\mathrm{dV} \tag{8.12}$$

Where k_B is Boltzmann's constant, T is the temperature, and σ is the conductivity of the sample. The magnetic field produced by this current dipole for a current, i, along the length element dl is calculated with the Biot-Savart law:

$$dB = \frac{\mu_0}{4\pi}\frac{\mathrm{i} * \mathrm{dl} \times \mathrm{R}}{\mathrm{R}^3} \tag{8.13}$$

Where *R* is the distance from the current source. In order to integrate Equation (8.11) over the volume, we take the root mean squared value for a field in the z direction by adding the components of i_x and i_y. Assuming the currents in the opposite directions are uncorrelated, the cross term of the root mean squared value will vanish. The magnetic field, given in Tesla Hz^{-2} is given by the following integral:

$$B_z = \left(4\,k_B T\sigma\left(\frac{\mu_0}{4\pi}\right)^2 \int\left(\frac{x^2+y^2}{(x^2+y^2+z^2)}\right)dV\right)^{1/2} \tag{8.14}$$

It should be noted that for the integration over the volume of x, y, and z, the zero of the coordinates is at the position of the atoms. Equation (8.14) reproduces the calculations for specific geometries given in Nenonen, Montonen, and Katila (1996) but is general enough to calculate the magnetic field coming from any arbitrarily shaped conductor. Equation (8.14) was used throughout the design of the experiment to calculate the Johnson noise from things like the inner magnetic shield, small titanium screws used for the plastic mirror mounts, and the magnetic field coils inside the shield will largely be common mode between the two lattices and will be completely canceled out. Even so, when calculated, these fall below the shot noise limit. The thin ITO coating will likely produce a fluctuating magnetic field that is different for the two lattices. Using the coating thickness of 30nm and a sheet resistance of 500 Ω/sq, Equation (8.14) gives around 3 pG/√Hz.

8.3.6. Noise currents

Another possible source of magnetic field noise could come from the thermoelectric effect. The high voltage system contains several connections of dissimilar metals. If there is a temperature difference between one end of a metal object and the

other, a voltage can be produced which will drive a current. The largest effect in our system comes from the connection of titanium to ITO. This has a thermoelectric effect of roughly 40 μV/ºK (Sarath Kumar and Kasiviswanathan, 2008). The current in the large loop formed by the connections to the top and the bottom of the plates is suppressed by the 5 MΩ resistors in that path. The smaller loop formed by the two ground plates is potentially more problematic because of the difficulty of inserting high vacuum compatible resistors into that loop. The plates themselves give a resistance of ~800 Ω. If we assume a temperature difference of 0.1 ºK this leads to a voltage of 4 μV and a current of 5 nA.

Using the estimates of Fang (2007), we conclude that a current running along the length of the plates would give a magnetic field in the z direction of about 1 fG/pA. Currents along the length of the plates need to be smaller than 2 nA to be smaller than the shot noise per shot. The thermoelectric current is within this order of magnitude and could potentially cause a problem depending on how well the temperature of the system equillibriates.

The final possible source of noise on the magnetic field is from the current from the 60 Hz pick-up on the plates shown in Figure 6-14. This was seen to have an amplitude of 2 nA. Additional suppression of this noise source can occur when the experimental timing is triggered on the 60 Hz line, so that the magnetic field produced from the 60 Hz line is the same during each run of the experiment.

In conclusion, noise can come from effects that alter the atom number or the phase of the interferometer. The types of noise described will affect the measurement differently, and most of them seem to fall within the requirements for the measurement.

8.4. Systematic errors

Systematic errors are effects that exactly mimic an eEDM. They are effects that shift the $+m_F$ levels linearly, with a sign flip that is correlated with the reversal of the electric field. Such an effect will be completely indistinguishable from an actual eEDM. Essentially these effects are magnetic fields (real or fictitious) that reverse directions with the sign of the electric field. Since these effects would be correlated with the reversal of the electric field throughout the entire run of the experiment, they will never be averaged out, and hence they need to be smaller than the systematic sensitivity quoted in Table 8-1. The ability to measure 25 independent subgroups of atoms along the vertical direction (see Section 3.2.2) and the fact that we have two lines of atoms separated by 1 cm will allow any source of systematic error with particular spatial characteristics (e.g., magnetic fields from leakage currents) to be tracked down.

We will discuss three possible systematic errors: leakage currents across the electric field plates, imperfect electric field reversals leading to a shift of the atoms in a magnetic field gradient, and a linear Stark interference effect measured by Chen *et al.* (1994) and identified as a possible systematic error by Romalis and Fortson (1999).

8.4.1. Leakage currents

When using such high voltages it is possible that a small current leaks from the high voltage center plate to the outer plates, presumably as a surface current on the fused silica spacers. Such current will produce a magnetic field at the atoms. That magnetic field will change directions with reversal of the electric field. The interactions between the magnetic fields and the magnetic dipole moment of the atom will directly

mimic the interaction of the electric field with the EDM of the atom, and will hence mimic the signal we are looking for. The magnetic field produced by leakage currents will have a characteristic shape. The spatially distinct interference fringes of the atoms would be useful in tracking down problematic leakage currents.

The relevant leakage currents are the steady state leakage currents of the high voltage system during the coherent measurement time. Transient charging currents and the large leakage currents which can be a precursor to electric field breakdown, though possibly detrimental to the experiment, are not relevant to the systematic error. If the new electric field plates behave similarly to the current plates, we can estimate the steady state leakage current from Figure 6-15. From this we estimate that at 60 kV the leakage current could be as high as 120 pA.

The magnetic field produced by a leakage current depends on the particular path it takes across the spacer. Fang (2007) estimated the size of a magnetic field coming from a worst case shape of the leakage current making a full loop around the spacer as it goes from the center to the outer plates. She found that the leakage current had to be less than 1.5 nA to be smaller than the systematic sensitivity.

If there is some component of the leakage current that runs along the length of the plates, the current will be very close to the atoms. If all of the leakage current ran along the plates, it would be 120 pA. Because we expect the leakage to occur at the spacers, the fraction of the current that ran along the plates near the atoms would be roughly 1/12 of this, while the rest of the current would go directly away from the center, lowering the current near the atoms to 10 pA. A further suppression occurs to the extent that the plates are attached symmetrically on the top and the bottom. this suppression happens to the extent that those currents are the same, which, according to Figure 6-15,

would give about a factor of 2 reduction. So we assume we have 5 pA flowing along the plates near the atoms.

Geometry suggests that a sheet current in the y direction would produce no magnetic field in the z direction and would not directly mimic the effect of an EDM. But to the extent that a leakage current's path is somewhat unpredictable, it is possible that it creates some field in the z direction. If we assume the worst case, which would be a single line of current that ran along the plates vertically, there will be a position along the x direction that gives the largest z component of the magnetic field. The current of a wire is given by:

$$\mathrm{B} = \frac{\mu_0 \, \mathrm{I}}{2 \, \pi \, \mathrm{r}} \tag{8.15}$$

Where *I* is the current, and *r* is the distance to the atoms. Only a fraction of that will be in the z direction, depending on how far off of the center of the plates the current is. If we call the distance along the x direction from the atoms to the line of current x, then the field in the z direction will be Equation (8.15) multiplied by Cos(θ), where θ is the angle that the plates make with respect to the line from the line of current to the atoms. Using some trigonometry, the field in the z direction is given by:

$$\mathrm{B_z} = \frac{\mu_0 \, \mathrm{I}}{2 \, \pi} \, \frac{\mathrm{x}}{\mathrm{x}^2 + \, 2\mathrm{mm}} \tag{8.16}$$

For 5 pA, Equation (8.16) has a maximum of 2.4 pG at *x* = 1.41 mm. This is a factor of 100 above the systematic sensitivity listed in Table 8-1. A single line of current is, however, an exceedingly unlikely path for the current to take. To estimate how much this will be a problem, we integrate Equation (8.16) over the entire width of the plates (42 mm), and divide by the integrated length with an offset to the center. We then determine how much of an offset is required to give an effect below the systematic sensitivity. As a result, if the atoms are offset from the center of the plates in the x direction by 2 mm, the

magnetic field will be smaller by a factor of 100, meeting the systematic sensitivity of $2.5*10^{-2}$ pG.

8.4.2. Atoms shifting in a B field gradient

Another potential systematic error is a composite effect of a non-uniform electric field, *E,* imperfect reversal of the electric field, $E_+ + E_- = \Delta|E|_\pm$, and a magnetic field gradient, ∇B. If the electric field has a gradient, the atoms will experience a force from the DC Stark effect. This force will shift them in the trap produced by the AC Stark effect of the lattice. However, because the DC Stark effect depends on E^2, the atoms would be shifted to the same place in a positive and negative electric field. If the positive applied electric field is different from the negative applied electric field, then the atoms will experience a slightly different force and will be displaced in the trap by different amounts depending on $\Delta|E|_\pm$. A slight displacement in the trap becomes a problem for the measurement if there is a gradient of the z-component of the magnetic field, because the atoms will move upon reversing the electric field and will hence experience a different magnetic field. This effect would be perfectly correlated with the electric field reversal and would mimic an EDM.

One possible way to create an electric field gradient is a wedge on the plates. The worst case wedge of the plates from Figure 6-12 is $\sim 1*10^{-4}$. This wedge would produce a ∇E of $3.7*10^5$ V/m^2. Based on the calculations of Fang (2007) we determine that this would create a displacement of 26 μm. Further, we assume that we can achieve a reversal of the electric field to at least a precision of one part in 10^4. This is readily achievable with our system. In order to meet the systematic sensitivity to the magnetic field of $2.5*10^{-14}$ G, this imposes the requirement for the gradient of the magnetic field in

the z direction to be smaller than 50-100 nG/cm. This level seems achievable in similar arrangements.

Electric field gradients could also stem from imperfections on the plates or pinholes in the ITO coating. The gradients produced by imperfections smaller than the scratch-dig of the plates would not be a problem. The ITO coating is done with a low to no-pinhole process by ECI. For this reason, among others, we wish to avoid damage to the coating from electric field breakdown or mechanical sources.

8.4.3. Third order effect

The final systematic error we describe is an effect that arises from interference between the AC electric dipole and higher order transitions (e.g., AC electric quadrupole and AC magnetic dipole transitions) in the presence of mixing from a DC electric field. The higher order transition amplitudes are usually forbidden by parity, but in the presence of a DC electric field, atomic states of opposite parity are mixed. As calculated by Romalis and Fortson (1999), these interferences create frequency shifts that are linear in both E and in m_F, and hence, this can produce a false EDM signal.

The shift for Cs atoms in a 1D optical lattice is approximately:

$$\Delta\nu = \left((.03\ \mathrm{Hz}) * (\boldsymbol{\varepsilon}\cdot\boldsymbol{\varepsilon_S})(\boldsymbol{b}\cdot\boldsymbol{\sigma}) + (.0006\ \mathrm{Hz}) * (\boldsymbol{b}\cdot\boldsymbol{\varepsilon_S})(\boldsymbol{\varepsilon}\cdot\boldsymbol{\sigma})\right) m_F * \frac{\Delta \mathrm{I}}{\mathrm{I}} \qquad (8.17)$$

Where $\boldsymbol{\varepsilon}$ is the polarization direction of the trapping laser light, $\boldsymbol{\varepsilon}_S$ is the polarization of the static E field, $\boldsymbol{b}$ is the direction of the magnetic field of the trapping light (i.e., $\boldsymbol{k}\times\boldsymbol{\varepsilon}$), and $\boldsymbol{\sigma}$ is the direction of spin quantization. They are suppressed in a standing wave by the fractional difference in intensity for the two opposing beams, $\Delta I/I$. In Equation (8.17) we have roughly estimated the size of this effect by adding the electric quadrupole and

magnetic dipole terms, which have roughly equal amplitudes. The coefficients in Equation (8.17) are scaled from Romalis and Fortson (1999) for a 150 kV/cm electric field and 10 μK trap depth at 1064 nm.

In our experiment, $\boldsymbol{\varepsilon}$ and $\boldsymbol{\varepsilon}_S$ are nominally parallel, as are $\boldsymbol{\sigma}$ and $\boldsymbol{\varepsilon}_S$. The lattice light is nearly perfectly linearly polarized, so $\boldsymbol{b}$ will be nearly perpendicular to $\boldsymbol{\varepsilon}_S$. Hence, this effect will be larger to the extent that the lattice polarization $\boldsymbol{\varepsilon}$, is misaligned with the static DC field, $\boldsymbol{\varepsilon}_S$. Due to our geometry, it is clear that the first term of Equation (8.12) dominates. In order to ensure that the first term in Equation (8.17) is smaller than the systematic sensitivity ($5*10^{-8}$ Hz), if the beam imbalance in the cavity is $< 10^{-3}$, the linear polarization of $\boldsymbol{\varepsilon}$ must be parallel to $\boldsymbol{\varepsilon}_S$ to better than $5*10^{-4}$. A more detailed calculation of this effect will ultimately be needed to fully understand its ramifications for the measurement.

In summary, most of the noise sources and systematic errors can be controlled to a level that will allow the eEDM to be measured with enough sensitivity to improve on the current experimental limit.

Chapter 9. Future Work

9.1. Getting to a proof of principle eEDM measurement

Currently, we have successfully prepared cold atoms in the measurement chamber. They have been trapped between three electric field plates in a well magnetically shielded region. The first steps of the state preparation, optical pumping and microwave state transfers, have been achieved. Even though the majority of parts required for the measurement are in place, there are several things that need to be done before a proof of principle eEDM measurement can take place: optimize a magnetic field zeroing procedure, purify the polarization of the optical cavities, replace the electric field plates, and perform spectroscopy and state preparation in the E-field quantized states.

Even with the magnetic shields installed, there will be some small bias magnetic field and field gradient at the atoms. These fields must be measured accurately and then cancelled for the electric field quantized low frequency B field transitions to be tested. Primarily we are concerned with magnetic fields in the z direction because our sensitivity to the field in other directions is greatly reduced.

One possible method to measure the B field is to measure the spin precession of an atomic sample optically pumped to the (3,3) state. Imagine that the atoms are initially be polarized in the x direction. If the atomic polarization is measured in the y direction, the signal will be linearly sensitive to a field in the z direction for small precessions. If a measurement is performed with a small field is applied in the z direction, a second measurement with the z field reversed will allow accurate determination of the residual field. The vertical spread of atoms (along the y direction) and the two different lattice locations (along the z direction) will give information about the residual magnetic field

gradients. The fields in the other directions can be determined with another set of measurements with x, y, and z cyclically permuted. These residual fields can be cancelled with the coils described in Chapter 5.

Another possible method for measuring the magnetic field is to do so in the electric field quantized superposition that is used for the eEDM measurement. This could hypothetically have the same sensitivity to magnetic field as the experiment has to the eEDM, but can only measure the z-component of the magnetic field, which is the component we care the most about. Using the vertical spread of atoms and the two lattices it would be possible to get information about derivatives in the y and z direction but not the x direction. In order to determine dB_z/dx we need to measure dB_x/dz.

The magnetic field gradients can be obtained by looking at the magnetic field for the two different lattice locations and the difference in the magnetic field along the length of the lattice, and by taking advantage of Maxwell's equations. These can be cancelled with the derivative coils described in Chapter 5.

Work on the magnetic field zeroing procedure has begun at the time of this writing, but a problem was found with the residual circular polarization of the cavity. This is currently too large to allow the field to be measured accurately and is too large for the measurement procedure itself. The vector light shift from a 100 μK lattice light represented a ~0.6 mG size fictitious magnetic that led to dephasing of the spin precession over a few ms because of the fact that different atoms see different intensities of light in the trap. In the current setup this produces an inhomogeneous shift of about 200 Hz. As discussed, this places a limitation on the ability to perform the low frequency B-field transitions.

An upgrade to the alignment procedure, particularly for the polarization of the cavity, is currently underway. This involves cleaning up the polarization of the input

beams with Glan-laser prisms, aligning the polarization axis with a ‘folding’ mirror within the cavity, and fine tuned control over the full three axis rotations of the Brewster plates. With these steps, hopefully the vector light shift will be small enough for us to perform the measurement.

Because of the problem described in Section 6.4.4, we will need to install new electric field plates. We are having an entirely new set of plates made. The plates are currently being manufactured and the coating will extend the ITO across the back of the ground plates. In order for the plates to be installed, the magnetic shield must be uninstalled. Even though we have detailed procedures worked out for each necessary step, we estimate that disassembling the system, replacing the electric field plates, and reassembling the system will take a minimum of four months.

With the electric field plates installed, spectroscopy on the electric field quantized states can take place, assuming the plates can sustain ~30 kV. The theory for the low frequency B-field transitions has largely been worked out (Zhu, *forthcoming*). The applied magnetic field is a combination of the frequency separation between (3,0)→(3,1), (3,1) →(3,2), and (3,2)→(3,3). The amplitude and relative phases between the frequency components are optimized to create a robust transfer from the (0,0) state to a superposition of (3, +3) and (3,-3) in a few cycles of the lowest frequency. There could be further complications for this due to the residual transverse B fields and the vector light shifts.

With these things accomplished, proof of principle eEDM measurements are possible.

9.2. Going from a proof of principle to a high precision measurement

After proof of principle eEDM measurements are performed, the next step will be to set up the experiment to take the large amounts of data required for statistical sensitivity. Many experimental and environmental parameters will have to be continuously monitored during the measurement: the ambient temperature fluctuations which may induce a change in the magnetization of the magnetic shields, ambient magnetic fields that may leak through the shields to the atoms, cavity power, cavity polarization, the voltage on the plates, and leakage currents. Ultimately, all of these parameters will be stored in a database along with the population information for all m_F levels each time the interference measurement is performed. Data analysis will infer if there are any superfluous correlations with the eEDM signal that could lead to false signals.

Ideally, the measurement procedure would be automated so that the system can step through the electric field polarization as well as the magnitude of the applied magnetic field, and perform the magnetic field zeroing procedure all with minimal human intervention. There are several parameters that will need to be able to check the sensitivity to the eEDM signal, e.g., the electric field magnitude and the depth of the cavity. If sensitivity could benefit from increased atom number, there are several easily achieved steps that could be taken (discussed in Sections 3.1.3 and 3.2.3), i.e. adding transverse cooling to the Zeeman slower and increasing the horizontal beam intensity in the measurement chamber.

After an eEDM measurement is performed using Cs, the ultimate check against systematic errors will be the measurement of the eEDM using Rb. For practical reasons, the development of the Rb system was halted several years ago and we have focused

solely on Cs. Cs is exactly 4.7 times more sensitive to the eEDM than Rb (Nataraj *et al.*, 2008), but its sensitivity to the magnetic field is the same. If a non-zero EDM signal is measured with Cs, when the experiment is performed in Rb, it should yield a signal exactly 4.7 times smaller. If the signal size for Rb is the same as Cs, one can be pretty certain that it stems from a magnetic field source. But if the signal is 4.7 times smaller, one has a very strong argument for the fact that the signal stems from a genuine eEDM. The ability to add a measurement of a second atomic system has been nominally built into all aspects of the experimental design, such as making sure all cooling beams could be mixed with Rb beams on dichromatic beam splitters, optimizing the electric field plate coatings for Cs and Rb light, and using trapping light that is far off resonance for both Cs and Rb. This addition, though technologically involved, could be implemented in a relatively straightforward way once it becomes necessary to do so.

9.3. Conclusion

The majority of parts necessary for an eEDM measurement are either in place or will be so soon. Using laser-cooled atoms in optical lattices, we take advantage of long measurement times and reduced systematic effects associated with the atomic velocity at the cost of possible interactions with the trapping laser. With a reasonable amount of data collection we anticipate a shot noise limited sensitivity that is a few hundred times below the current experimental limit. Keeping noise and systematic errors low enough is a challenge, but there is still a wide range for a significant improvement on the limit of the electron electric dipole moment.

If we can push the experimental limit down, we can either see a result consistent with zero, or we see a non-zero result. A result consistent with zero would force some theories of physics beyond the standard model, to explain why the eEDM was not observed. If we see a non-zero result, this would be the first direct evidence for physics beyond the standard model.

Appendix A. Launch Alignment

The angle at which the atoms are launched is sensitive to the absolute alignment of the optical molasses beams in space. Cooling in optical molasses usually depends only on the relative alignment of the beams, that is, the overlap of one beam with its counter-propagating beam. The relative alignment of the optical molasses is easy to achieve with apertures on either side of the MOT chamber.

The absolute alignment in space is critical here because when the frequency of the beams changes for the launch, the angle of the launch depends on the orientation of the beams in space. Figure A-1 shows the three aspects of beam alignment for the launch. The alignment in the x-y plane (α) can be accomplished by keeping all up and down beams in a plane and rotating that plane with respect to the plane normal to the horizontal beams. Alignment in the z-y plane is accomplished by adjusting the horizontal angle of the horizontal beams (β), and by adjusting the angle of one counter-propagating pair of up and down beams with respect to the other (γ).

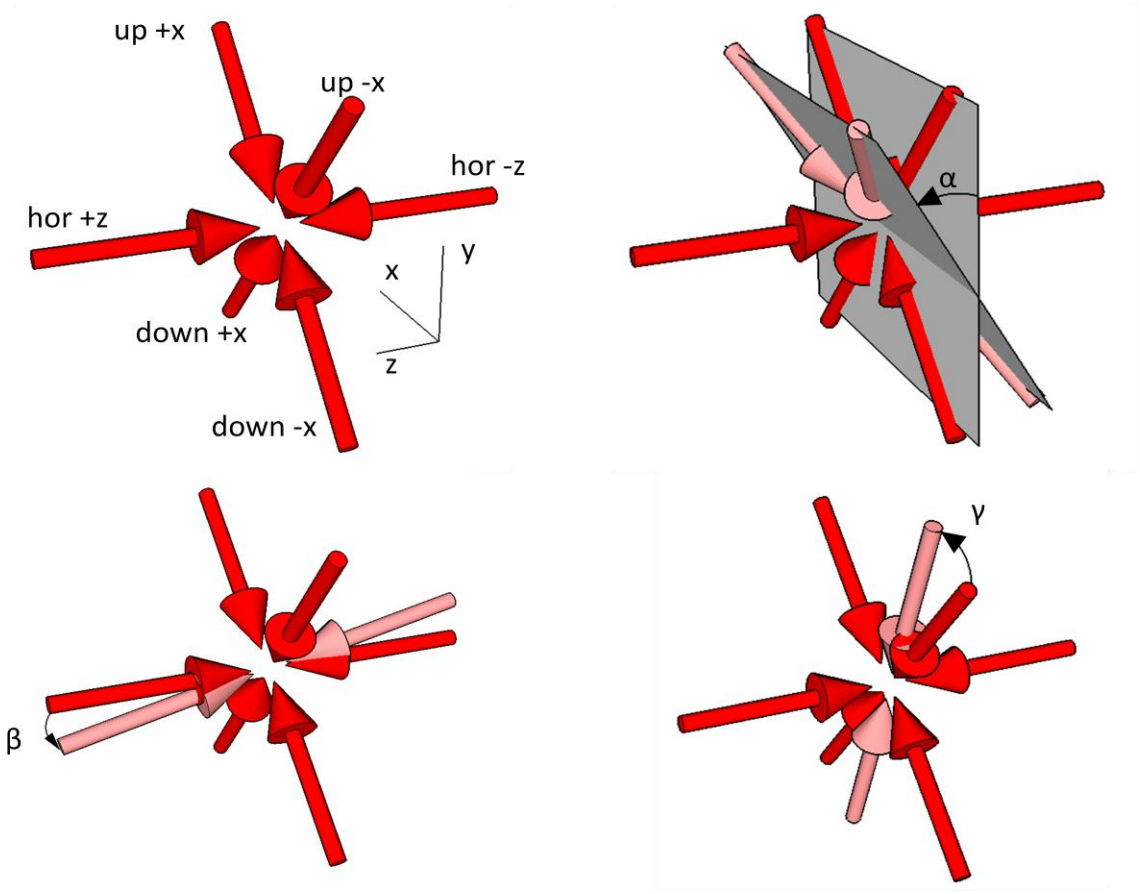

Figure A-1. *Launch alignment*

This is made much more difficult by the fact that all of the beams must remain well-centered between the two lattice locations in order to maintain good cooling at the two lattice locations during the loading as well as during the launch. This is accomplished by always adjusting counter-propagating beams simultaneously, in opposite directions on their respective apertures, so that the adjustments in Figure A-1 are as close to real rotations about the center position as possible. The apertures are then centered on the beams so that further alignment adjustments or corrections can be made. If care is not taken to keep the beams centered, a particular change in alignment

that improves the launch for one lattice may not be better for the other lattice, forcing one to start over again.

The alignment procedure goes as follows. If you cannot see the atoms in the measurement chamber for the initial alignment, you launch the atoms as high as you can, while you are still able to see them as they fall back down to the MOT chamber. Adjust the alignment in order to peak the signal of the atoms returning, then launch higher and higher, repeating this procedure until you can image atoms at the top in the measurement chamber. You can further adjust the beam alignment and other launch parameters to peak up the atom signal at the top.

In practice, aligning the optical molasses beams for the launch is a very laborious process requiring a lot of re-alignment and adjustments so that the beams do not clip, etc. For this reason, it is highly beneficial to perform extensive measurements in an attempt to align the MOT apertures in the a priori correct locations. If this is done, only minimal alignment adjustments will be needed.

Appendix B. Cavity Lock Circuit

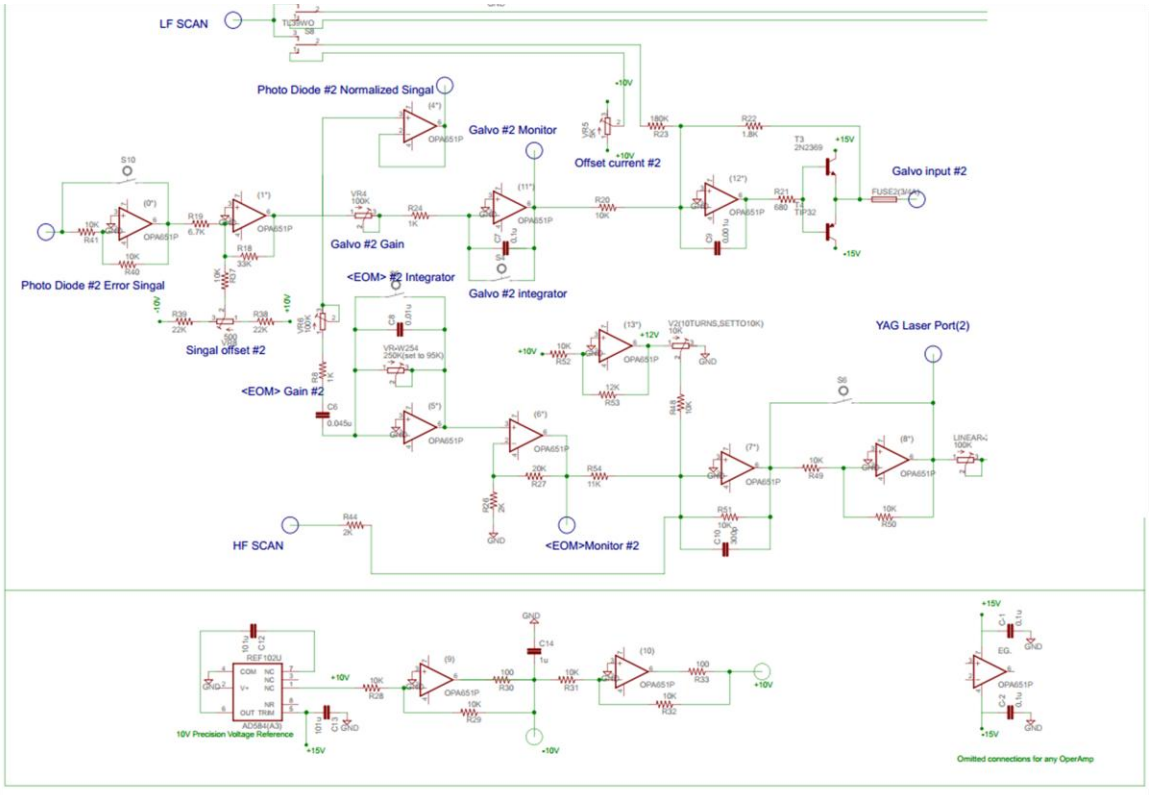

Figure B-1. *Cavity lock circuit*

This diagram shows the lock circuit for one of the cavities. A second identical circuit functions for the other cavity. At the top of the circuit, the low frequency scan allows us to manually input a voltage to the galvanometers. The photodiode error signal is sent split into a low and a high frequency feedback systems. The low frequency signal goes to a tunable PID lock and output to the galvanometers. The high frequency feedback also goes through a tunable PID lock circuit and then to the PZT driver (labeled YAG Laser Port for historical reasons). An oscillating voltage can be added at (EOM) monitor, in order to map out the transfer functions as seen in Figure 3-13.

Appendix C. Plate Coating Reflection and Transmission

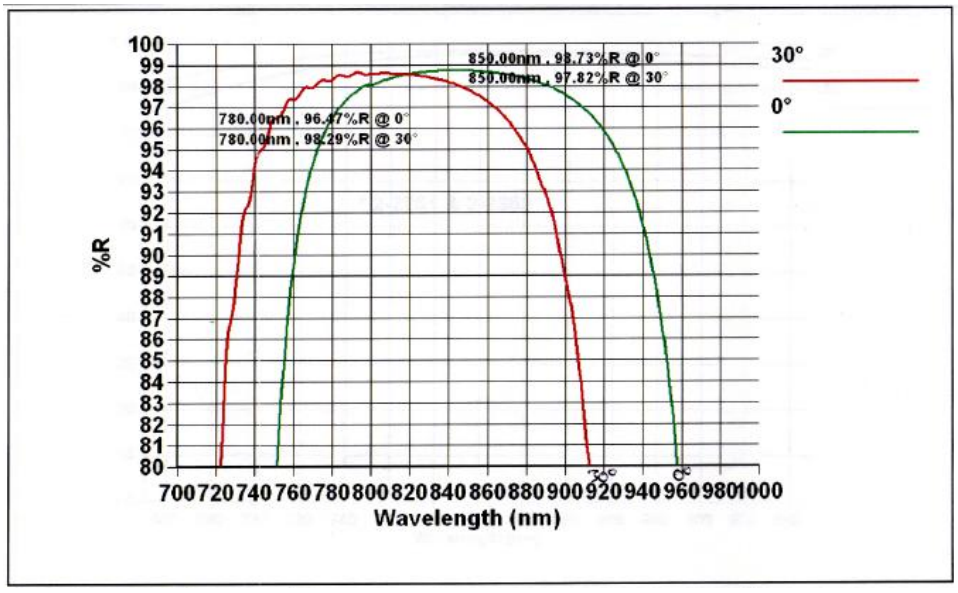

Figure C-2. *Reflection of center electric field plate*

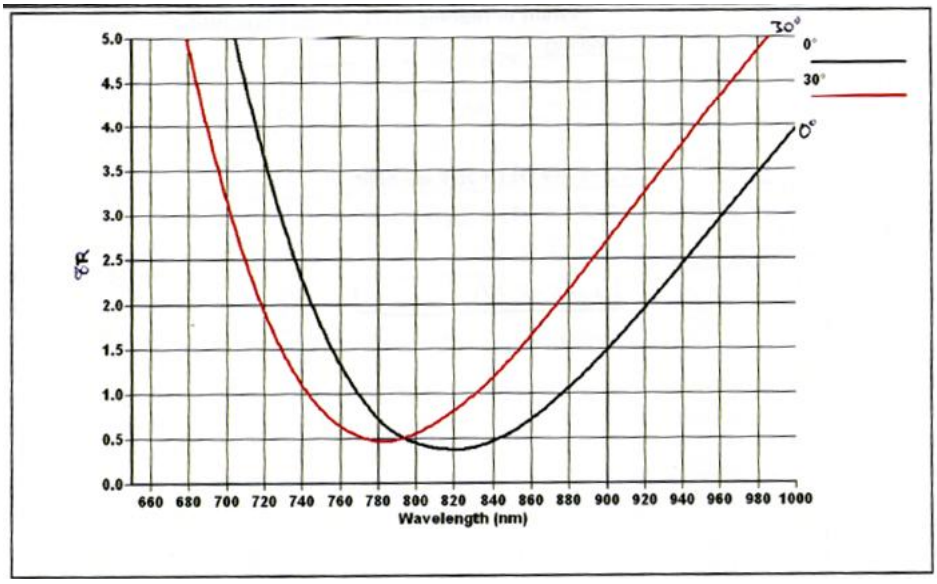

Figure C-3. *Reflection of outer electric field plates*

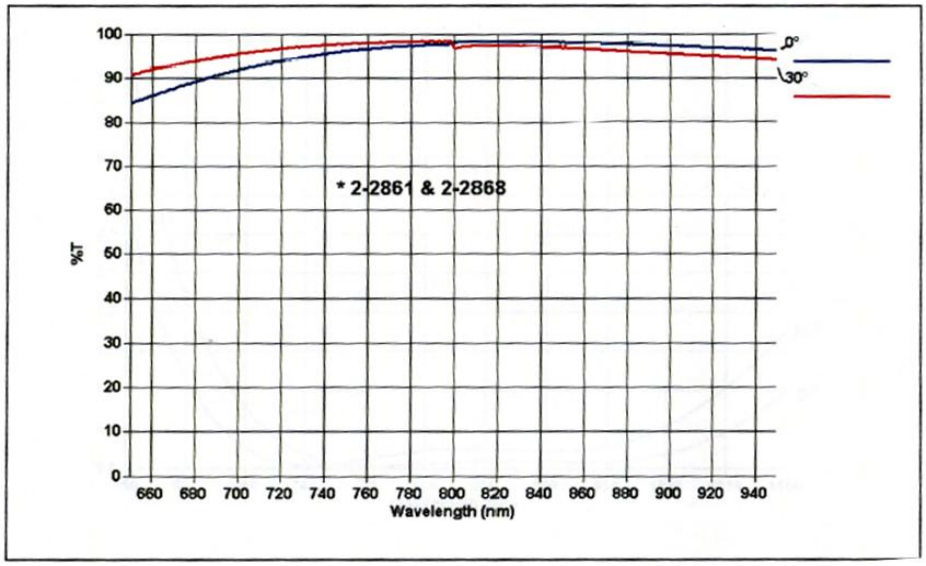

Figure C-4. *Total transmission of outer electric field plates*

Appendix D. Plate Mounting Designs

Front View

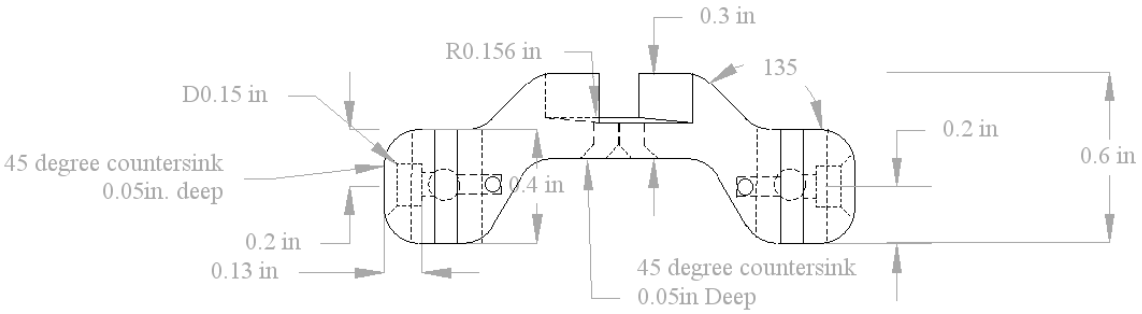

Top View

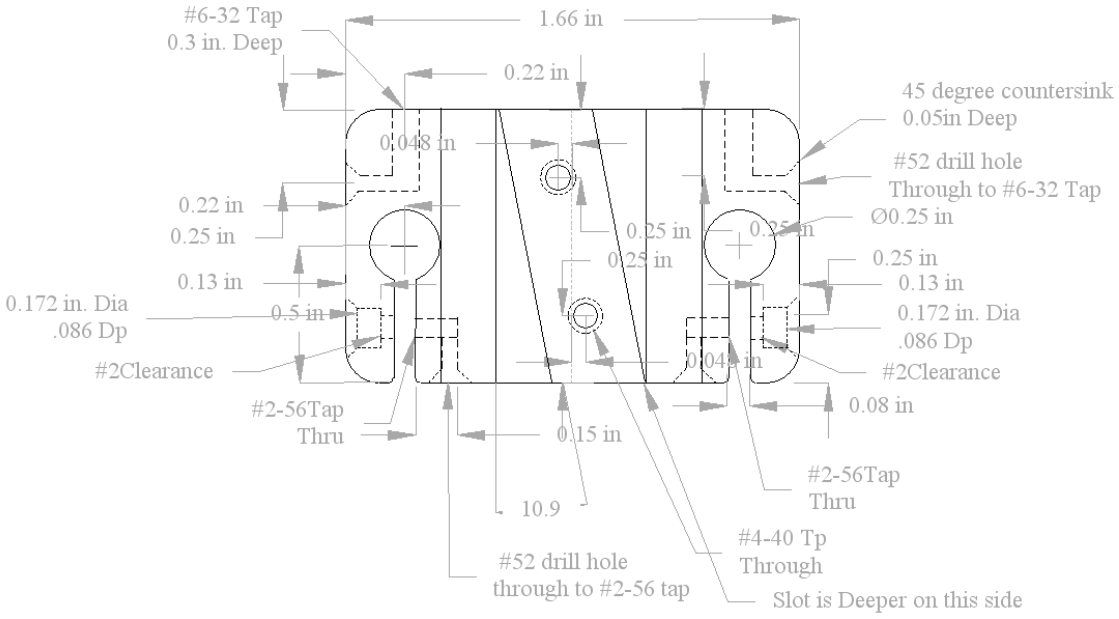

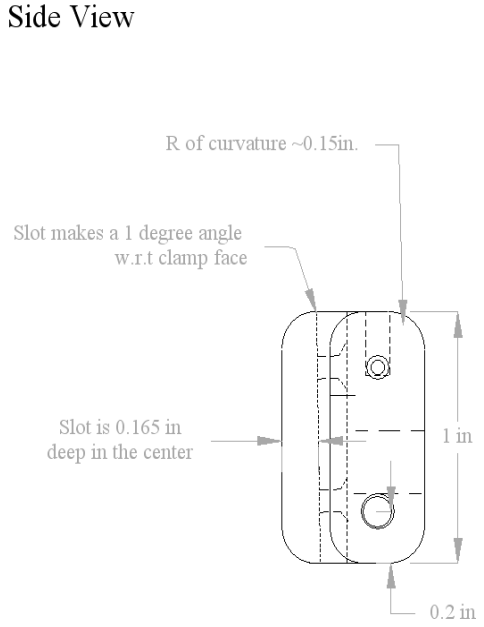

Figure D-1. *Clamp body*

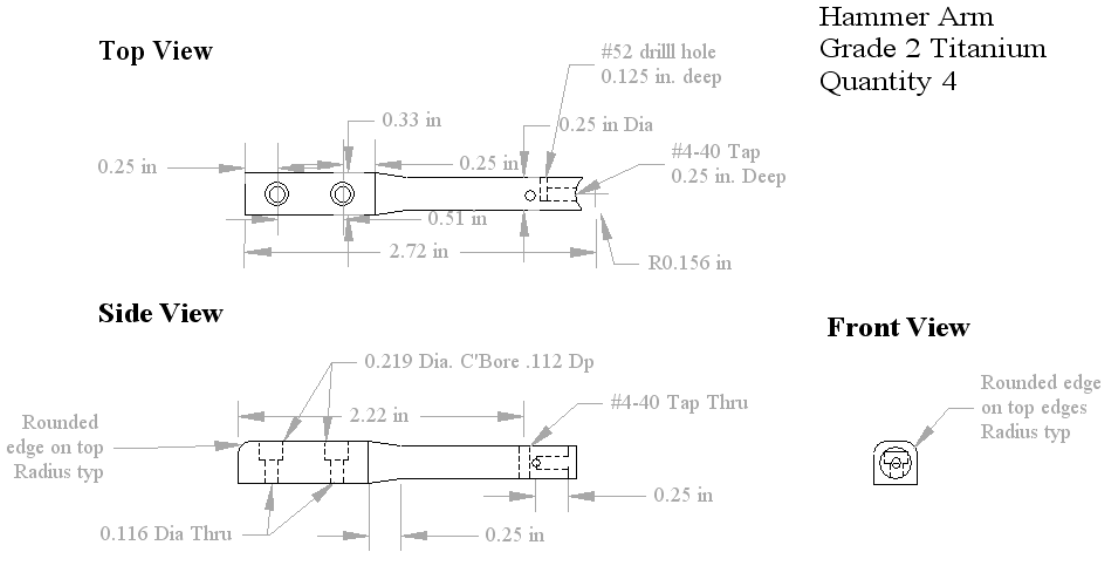

Figure D-2. *Hammer arm*

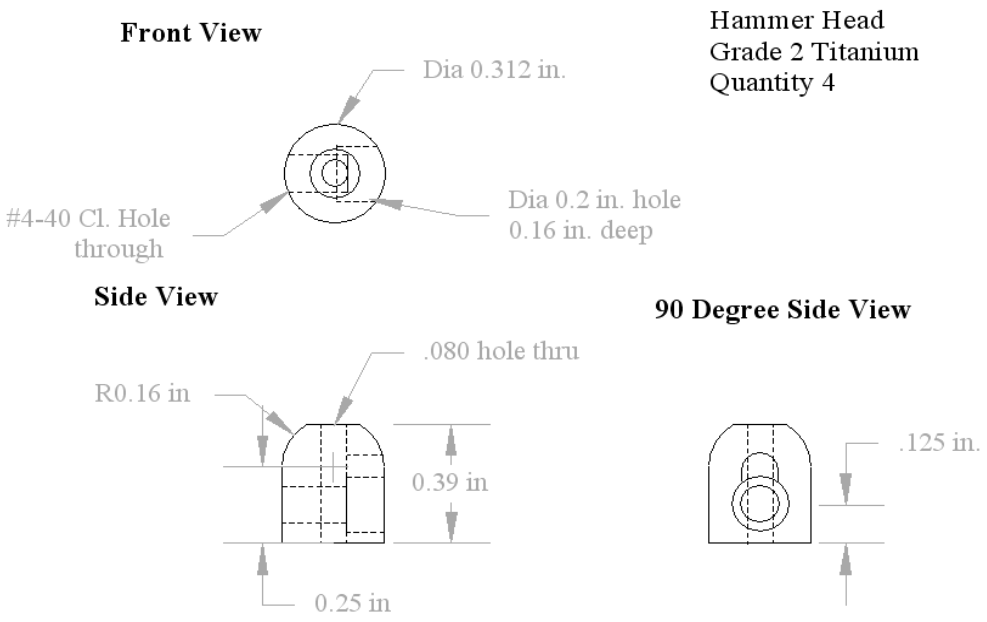

Figure D-3. *Hammer head*

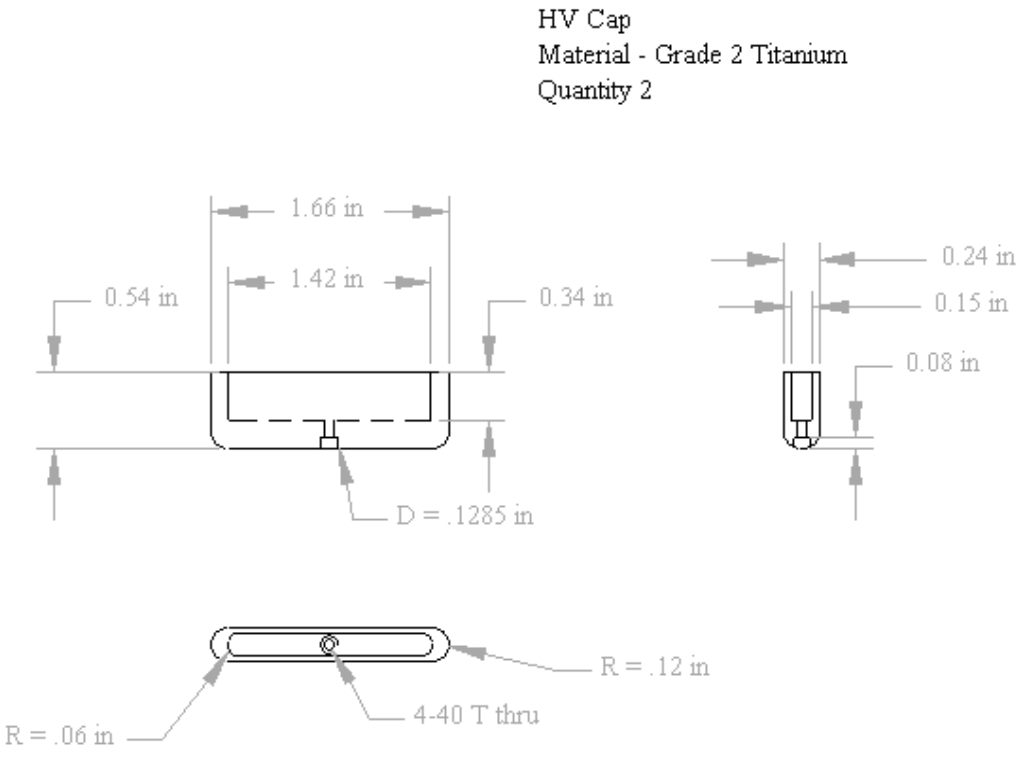

Figure D-4. *Titanium cap*

Bibliography

Aaij, R., *et al.*, (LHCb Collaboration), 2012, "Evidence for *CP* violation in time-integrated $D^0 \to h^- h^+$ decay rates," Phys. Rev. Lett. **108**, 111602.

Abe, K., *et al.*, 2001, "Observation of large *CP* violation in the neutral *B* meson system," Phys. Rev. Lett. **87**, 091801.

Abelev, B. I., *et al.*, 2010, "Observation of charge-dependent azimuthal correlations and possible local strong parity violation in heavy-ion collisions," Phys. Rev. C **81**, 054908.

Amini, J. M., C. T. Munger, and H. Gould, 2007, "Electron electric-dipole-moment experiment using electric-field quantized slow cesium atoms," Phys. Rev. A **75**, 063416.

Aubert, B., *et al.*, 2002, "Measurement of the *CP* asymmetry amplitude sin2β with B^0 mesons," Phys. Rev. Lett. **89**, 201802.

Baker, C. A., *et al.*, 2006, "Improved experimental limit on the electric dipole moment of the neutron," Phys. Rev. Lett. **97**, 131801.

Beenakker, C., and C. Schönenberger, 2003, "Quantum shot noise," Phys. Today **May**, 37-42.

Bernreuther, W., and M. Suzuki, 1991, "The electric dipole moment of the electron," Rev. Mod. Phys. **63**, 313-340.

Beukema, G. P., 1973, "Influence of adsorbed gases on prebreakdown currents in vacuum," J. Phys. D **6**, 1455-1466.

Bijlsma, M., B. J. Verhaar, and D. J. Heinzen, 1994, "Role of collisions in the search for an electron electric-dipole moment," Phys. Rev. A **49**, R4285-R4288.

Bloch, I., J. Dalibard, and W. Zwerger, 2008, "Many-body physics with ultracold gases,"

Rev. Mod. Phys. **80**, 885-964.

Brown, J. M., S. J. Smullin, T. W. Kornack, and M. V. Romalis, 2010, "New limit on Lorentz and CPT-violating neutron spin interactions," Phys. Rev. Lett. **105**, 151604.

Budker, D., D. F. Kimball, and D. P. DeMille, *Atomic Physics: An Exploration Through Problems and Solutions* (Oxford University Press, New York).

Burt, E. A., and C. R. Ekstrom, 2002, "Optimal three-layer cylindrical magnetic shield sets for scientific applications," Rev. Sci. Instrum. **73**, 2699-2704.

Carrico, J. P., A. Adler, M. R. Baker, S. Legowski, E. Lipworth, P. G. H. Sandars, T. S. Stein, and M. C. Weisskopf, 1968, "Atomic-beam resonance measurement of the differential polarizability between Zeeman substates in the ground state of the Cesium atom," Phys. Rev. **170**, 64-76.

Chen, X., F. R. Huang-Hellinger, B. R. Heckel, and E. N. Fortson, 1994, "Measurement of a linear Stark interference effect on the rubidium *D1* absorption line," Phys. Rev. A **50**, 4729-4731.

Chin, C., C. Leiber, V. Vuletić, A. J. Kerman, and S. Chu, 2001, "Measurement of an electron's electric dipole moment using Cs atoms trapped in optical lattices," Phys. Rev. A **63**, 033401.

Chu, S., 1998, "The manipulation of neutral particles," Rev. Mod. Phys. **70**, 685-706.

Commins, E. D., 2007, "Electric dipole moments of elementary particles, nuclei, atoms, and molecules," J. Phys. Soc. Jpn, **76**, 111010.

Commins, E. D., J. D. Jackson, and D. P. DeMille, 2007, "The electric dipole moment of the electron: An intuitive explanation for the evasion of Schiff's theorem," Am. J. Phys. **75**, 532-536.

Crane, S., and C. R. Ekstrom, 2005, "Nonmagnetic UHV optical viewports," *Proceedings*

of the 2005 IEEE international frequency control symposium and exposition, Vancouver (IEEE Piscataway), 297.

Drever, R. W. P., J. L. Hall, F. V. Kowalksi, J. Hough, G. M. Ford, A. J. Munley, and H. Ward, 1983 “Laser phase and frequency stabilization using an optical resonator,” Appl. Phys. B. **31**, 97-105.

Ebert, M. F., 2010, “Progress towards a measurement of the electron electric dipole moment using cold Cs and Rb atoms in a 1D optical trap,” B. S. Undergraduate Honors Thesis (The Pennsylvania State University).

Ellis, J., 2003, “Antimatter matters,” Nature **424**, 631-634.

Fang, F., 2007, “Progress toward a measurement of the electron electric dipole moment using ultra-cold atoms,” Ph.D. dissertation (The Pennsylvania State University).

Fang, F., and D. S. Weiss, 2009, “Resonator-enhanced optical guiding and trapping of Cs atoms,” Opt. Lett. **34**, 169-171.

Feynman, R. P., and M. Gell-Mann, 1958, “Theory of the Fermi interaction,” Phys. Rev. **109**, 193-198.

Fitch, V. L., R. F. Roth, J. S. Russ, and W. Vernon, 1965, “Evidence for constructive interference between coherently regenerated and *CP*-nonconserving amplitudes,” Phys. Rev. Lett. **15**, 73-75.

Fixler, J. B., G. T. Foster, J. M. McGuirk, and M. A. Kasevich, 2007, “An interferometer measurement of the Newtonian constant of gravity,” Science **5**, 74-77.

Fortson, N., P. Sandars, and S. Barr, 2003, “The search for a permanent electric dipole moment,” Phys. Today **June**, 33-39.

Foster, G. T., J. B. Fixler, J. M. McGuirk, and M. A. Kasevich, 2002, “Method of phase extraction between coupled atom interferometers using ellipse-specific fitting,” Opt. Lett. **27**, 951-953.

Garwin, R. L., L. M. Lederman, and M. Weinrich, 1957, “Observation of the failure of conservation of parity and charge conjugation in meson decays, the magnetic moment of the free muon,” Phys. Rev. **105**, 1415-1417.

Griffiths, W. C., M. D. Swallows, T. H. Loftus, M. V. Romalis, B. R. Heckel, and E. N. Fortson, 2009 “Improved limit on the permanent electric dipole moment of ^{199}Hg,” Phys. Rev. Lett. **102**, 101601.

Guido, D., and R. Longo, 1995, “An algebraic spin statistics theorem,” Commun. Math. Phys. **172**, 517-533.

Harris, F. J., 1968, “On the use of windows for harmonic analysis with discrete Fourier transform,” *Proceedings of the IEEE* **66**, 51-83.

Hodapp, T. W., C. Gerz, C. Furtlehner, C. I. Westbook, W. D. Phillips, and J. Dalibard, 1995, “Three dimensional spatial diffusion in optical molasses,” Appl. Phys. B **60**, 135-143.

Hood, C. J., H. J. Kimble, and J. Ye, 2001, “Characterization of high-finesse mirrors: Loss, phase shifts, and mode structure in an optical cavity,” Phys. Rev. A **64**, 033804.

Hoogeveen, F., 1990, “The standard model prediction for the electric dipole moment of the electron,” Nucl. Phys. **341**, 322-340.

Hosoya , M., and E. Goto, 1991, “Coils for generating uniform fields in a cylindrical ferromagnetic shield,” Rev. Sci. Instrum. **62**, 2472-2475.

Hudson, J. J., D. M. Kara, I. J. Smallman, B. E. Sauer, M. R. Tarbutt, and E. A. Hinds, 2011, “Improved measurement of the shape of the electron,” Nature **473**, 493-496.

Itano, W. M., J. C. Bergquist, J. J. Bollinger, J. M. Gilligan, D. J. Heinzen, F. L. Moore, M. G. Raizen, and D. J. Wineland, 1993, “Quantum projection noise: Population

fluctuations in two-level systems," Phys. Rev. A **47**, 3554-3570.

Jackson, J. D., 1962, *Classical Electrodynamics* (John Wiley & Sons, Inc., New York).

Kim, Y. J., C.–Y. Liu, S. K. Lamoreaux, G. Visser, B. Kunkler, A. V. Matlashov, and T.G. Reddy, 2011, "New experimental limit on the electric dipole moment of the electron in a paramagnetic insulator," arXiv: 1104.4391v1 [nucl-ex] 22 April 2011.

Khriplovich, I. B., and S. K. Lamoreaux, 1997, *CP Violation Without Strangeness*, (Springer, Berlin).

Kobayashi, M., and T. Maskawa, 1973, "*CP*- violation in the renormalizable theory of weak interaction," Prog. Theor. Phys. **49**, 952-957.

Lamoreaux, S. K., 1999, "Feeble magnetic fields generated by thermal charge fluctuations in extended metallic conductors: Implications for electric-dipole moment experiments," Phys. Rev. A **60**, 1717-1719.

Lamoreaux, S. K., 2002, "Solid-state systems for the electron electric dipole moment and other fundamental measurements," Phys. Rev. A **66**, 022109.

Landau, L., 1957, "On the conservation laws for weak interactions," Nucl. Phys. **3**, 127-131.

Leanhardt, A. E., J. L. Bohn, H. Loh, P. Maletinsky, E. R. Meyer, L. C. Sinclair, R. P. Strutz, and E. A. Cornell, 2011, "High-resolution spectroscopy on trapped molecular ions in rotating electric fields: A new approach for measuring the electron electric dipole moment," J. Mol. Spectrosc. **270**, 1-25.

Lederman, L. M., and C. T. Hill, 2004, *Symmetry and the beautiful universe* (Prometheus Books, Amherst).

Lee, T. D., and C. N. Yang, 1956, "Question of parity conservation in weak interactions," Phys. Rev. **104**, 254-258.

Lee, T. D., R. Oehme, and C. N. Yang, 1957, "Remarks on possible noninvariance under

time reversal and charge conjugation," Phys. Rev. **106**, 340-345.

Ma, L.-S., J. Ye, P. Dubé, and J. L. Hall, 1999, "Ultrasensitive frequency-modulation spectroscopy enhanced by a high-finesse optical cavity: Theory and application to overtone transitions of C_2H_2 and C_2HD," J. Opt. Soc. Am. B **16**, 2255-2268.

Maltin, L., and S. Koch, 2009, "A practical guide to low frequency magnetic shielding," *Workshop presented at The Pennsylvania State University,* University Park, PA, Nov. 13.

Metcalf, H. J., and P. van der Straten, 1999, *Laser Cooling and Trapping* (Springer, New York).

Meyer, E. R., and J. L. Bohn, 2008, "Prospects for an electron electric-dipole moment search in metastable ThO and ThF^+," Phys. Rev. A **78**, 010502(R).

Nataraj, H. S., B. K. Sahoo, D. P. Das, and D. Mukherjee, 2008, "Intrinsic electric dipole moments of paramagnetic atoms: Rubidium and cesium," Phys. Rev. Lett. **101**, 033002.

Nenonen, J., J. Montonen, and T. Katila, 1996, "Thermal noise in biomagnetic measurements," Rev. Sci. Instrum. **67**, 2397-2405.

Nielsen, M. A., and I. L. Chuang, 2000, *Quantum Computation and Quantum Information* (University Press, Cambridge).

Noble, A., and M. Kasevich, 1995, "UHV optical window seal to a conflat knife edge," Rev. Sci. Instrum. **65**, 3042-3043.

Noether, E., 1918, "Invariant variation problems," *Nachr. v. d. Ges. d. Wiss. zu Göttingen*, 235-257. [English translation in, Tavel, M. A., *Transport theory and statistical physics* **1**, 183-207 (1971)].

Nyquist, H., 1928, "Thermal agitation of electric charge in conductors," Phys. Rev. **32**, 110-113.

Patten, R. A., 1971, “Michelson interferometer as a remote gauge,” Appl. Opt. **10**, 2717-2721.

Petrov, A. N., N. S. Mosyagin, and A. V. Titov, 2009, “Theoretical study of low-lying electronic terms and transition moments for HfF^+ for the electron electric-dipole moment search,” Phys. Rev. A **79**, 012505.

Phillips, W. D., and H. Metcalf, 1982, “Laser deceleration of an atomic beam,” Phys. Rev. Lett. **48**, 596-599.

Pospelov, M., and A. Ritz, 2005, “Electric dipole moments as proves of new physics,” Ann. Phys. **318**, 119-169.

Purcell, E. M., and N. F. Ramsey, 1950, “On the possibility of electric dipole moments for elementary particles and nuclei,” Phys. Rev. **78**, 807.

Ramsey, N. F., 1950, “A molecular beam resonance method with separated oscillating fields,” Phys. Rev. **78**, 695-699.

Regan, B. C., E. D. Commins, C. J. Schmidt, and D. DeMille, 2002, “New limit on the electron electric dipole moment,” Phys. Rev. Lett. **88**, 071805.

Romalis, M. V., and E. N. Fortson, 1999, “Zeeman frequency shifts in an optical dipole trap used to search for an electric-dipole moment,” Phys. Rev. A **59**, 4547-4558.

Rushchanskii, K. Z., *et al.*, 2010, “A multiferroic material to search for the permanent electric dipole moment of the electron,” Nature Mater. **9**, 649-654.

Sakharov, A. D., 1966, “Violation of *CP* invariance, *C* asymmetry, and baryon asymmetry of the universe,” Pis’ma Zh. Eksp. Teor. Fis. **5**, 32-35. [English translation in Sov. Phys. Usp. **34**, 392-393 (1991)].

Sandars, P. G. H., 1965, “The electric dipole moment of an atom,” Phys. Lett. **14**, 194-196.

Sarath Kumar, S. R., and S. Kasiviswanathan, 2008, “A hot probe setup for the

measurement of Seebeck coefficient of thin wires and thin films using integral method," Rev. Sci. Instrum. **79**, 024302.

Schiff, L. I., 1963, "Measurability of nuclear electric dipole moments," Phys. Rev. **132**, 2194-2200.

Schreck, F., and T. P. Meyrath, "A laboratory control system for cold atom experiments," available at: http://george.ph.utexas.edu/~meyrath/informal/ .

Simon, E., P. Laurent, and A. Clairon, 1997, "Measurement of the Stark shift of the Cs hyperfine splitting in an atomic fountain," Phys. Rev. A **57**, 436-439.

Solmeyer, N., K. Zhu, and D. S. Weiss, 2011, "Mounting ultra-high vacuum windows with low stress induced birefringence," Rev. Sci. Instrum. **82**, 066105.

Sudarshan, E. C. G., and R. E. Marshak, 1958, "Chirality invariance and the universal Fermi interaction," Phys. Rev. **109**, 1860-1862.

Suits, B. H., and D. E. Wilken, 1989, "Improving magnetic field gradient coils for NMR imaging," J. Phys. E **22**, 565-573.

Sumner, T. J., J. M. Pendleburry, and K. F. Smith, 1987, "Conventional magnetic shielding," J. Phys. D **20**, 1095-1101.

Varpula, T., and T. Poutanen, 1983 "Magnetic field fluctuations arising from thermal motion of electric charge in conductors," J. Appl. Phys. **55**, 4015-4021.

Vutha, A. C., *et al.,* 2007, "Search for the electric dipole moment of the electron with thorium monoxide," J. Phys. B **43**, 074007.

Vutha, A. C., *et al.,* 2011, "Corrigendum: Search for the electric dipole moment of the electron with thorium monoxide," J. Phys. B **44**, 079803.

Wu, C. S., E. Ambler, R. W. Hayward, D. D. Hoppes, and R. P. Hudson, 1957, "Experimental test of parity conservation in beta decay," Phys. Rev. **105**, 1412-1415.

Zhu, K., N. Solmeyer, and D. S. Weiss, 2012, “A low noise, nonmagnetic fluorescence detector for precision measurements,” Rev. Sci. Instrum. **83**, 113105.

Zhu, K., *forthcoming*, Ph.D. dissertation (The Pennsylvania State University).

VITA

Neal Solmeyer

Education

Ph.D.	Physics	Pennsylvania State University	2013
B. A.	Physics and Philosophy	Carleton College	2006

Award

ECOS Star	For assisting the department with laser safety compliance	2010

Professional Society Memberships

American Physical Society (APS)	2008 - present
American Association for the Advancement of Science (AAAS)	2010 - present

Papers

Zhu, K., **N. Solmeyer**, and D. S. Weiss, 2012, “A low noise, nonmagnetic fluorescence detector for precision measurements,” Rev. Sci. Instrum. **83**, 113105.

Solmeyer, N., K. Zhu, and D. S. Weiss, 2011, “Mounting ultra-high vacuum windows with low stress-induced birefringence,” Rev. Sci. Instrum. **82**, 066105.

Talk

***Meyer, N.**, K. Zhu, F. Fang, and D. Weiss, Oct. 2008, "An electron electric dipole moment with atoms in optical lattices," in *Laser Science XXIV*, OSA Technical Digest (CD) (Optical Society of America, 2008), paper LTuD2.

Posters

Solmeyer, N., K. Zhu, and D. S. Weiss, Aug. 2012, “An electron electric dipole moment search using cesium atoms,” presented at *Gordon Research Conference: Quantum Science*, Easton, MA.

Solmeyer, N. E., K. Zhu, and D. S. Weiss, July 2011, “Progress towards a permanent electron electric dipole moment search using cold atoms in an optical lattice,” presented at *DAMOP*, Atlanta, GA.

Solmeyer, N. E., K. Zhu, M. Ebert, F. Fang, and D. S. Weiss, July 2010, “Using cold atoms in optical lattices to search for an electron EDM,” presented at *Lepton Moments*, Centerville, MA.

***Meyer, N. E**., K. Zhu, F. Fang, and D. S. Weiss, May 2009, “Progress towards a permanent electron electric dipole moment search using cold atoms in an optical lattice,” presented at *DAMOP*, Charlottseville, VA.

*Presented under former name, Neal Meyer